Metasurface Based Mid-infrared Devices

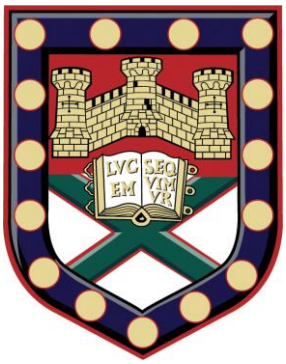

Cheng Shi

College of Engineering, Mathematics and Physical Science

University of Exeter

A thesis submitted for the degree of

Doctor of Philosophy

July 2019

Metasurface Based Mid-infrared Devices

Submitted by Cheng Shi to the University of Exeter
as a thesis for the degree of
Doctor of Philosophy in Engineering
In July 2019

I certify that all material in this thesis which is not my own work has been identified and that no material has previously been submitted and approved for the award of a degree by this or any other University.

(Signature) .....

Cheng Shi
July 2019

Dedicated to Yiqi and Kaiwen

Acknowledgements

First of all, I would like to thank my supervisors, Prof Geoffrey Nash and Dr Isaac Luxmoore, for their patient guidance and support during all my four years of PhD study. Without their supervising, I doubt that I can be in this place today. Geoff, you are always enthusiastic, knowledgeable and optimistic. Thank you so much for giving me so many valuable advice both for academic research and daily life, I knew if I get confused, you are always the right person I turn to ask for guidance. Thank you also for taking so much for your valuable time in reading this thesis and all the constructive comments. Isaac, you are always more than willing to answer any questions I had, no matter how insignificant. I benefited greatly from many fruitful discussions with you. I also appreciate your efforts in getting me familiar with all the experiment equipment.

Next, I would also like to thank the colleagues in our group that I have worked alongside these four years. Special thanks to Dr Nathan Mahlmeister who fabricated the thermal emitters during the first years of my PhD. I'm also grateful for the contributions of Dr Prarthana Gowda and Mr Callum Penrose, Ms Jacqueline Pitts in the work of enhanced ATR spectroscopy. I also would like to express my appreciate to Dr Tim Poole who gave me a lot of support and suggestions in using the equipment in the cleaning room, and Ms Camilla Owens who creates a lot of joy in the office, and all other supportive colleagues:

Dr Pouya Caroline, Dr Benjamin Ash, Ms Jessica Brown, Ms Vicky Kyrimi, Ms Hannah Barnard, Ms Eleanor Osborne, and Ms Isabel Mitchell.

Outside my research group, I'd like to thank everyone in the CDT for all the fun over the four years, especially to Laicong Deng, Carlota Ruiz De Galarreta, Henry Fernandez, Ben Hogan, Joaquin Faneca. It is the friendships with you that enrich my memory of the PhD life.

Last but not least, my deepest thanks to my family, my parents Liping Zhou and Yaodong Shi. despite the long distance between Exeter and Shanghai, I can always feel their encouragement, everlasting love and unconditional financial and emotional support throughout the whole 4 years. Also greatest appreciate with love to my wife, Yiqi Wang who stands by me through all my travails and son, Kaiwen Shi. who brings a lot of joy into my life. They are the intrinsic motivations for me to finish my degree.

Finally, I would like to say thank you to many other people whose names are not mentioned here but this does not mean that I have forgotten their help.

ABSTRACT

The development of compact, efficient, and powerful mid-infrared devices is mainly restrained by the limited choice of materials due to the high loss of conventional optical materials in the mid-infrared range. The aim of this work was to find alternative novel materials which would enable the realization of devices with smaller size while maintaining its functionality. Metasurface and graphene have emerged as promising materials which can help us to manipulate the infrared light within nano-meter scale thickness. In this thesis, three different mid-infrared devices, thermal emitter, wave trapping sensor and phase modulator were designed based on either metasurface or both metasurface and graphene. Devices were all fabricated with modern semiconductor fabrication processes and their performances were also fully investigated, both experimentally and through simulations.

A metasurface was first designed as a frequency selective layer on a graphene thermal emitter to tailor the graybody emission spectrum from a graphene filament into two discrete narrow bands for applications such as gas sensing or molecule detection. The emission and reflectance spectra of the devices were characterised using (FTIR) Fourier transform infrared spectroscopy and showed good agreement with simulations based on the Finite-difference time-domain (FDTD). method.

The use of a metasurface to enhance the interaction between molecular vibrations and the evanescent waves, in a total attenuated reflectance system, was also explored. A complementary ring-resonator structure was patterned onto both silicon and SiO_2/Si substrates, and the spectral properties of both devices were characterised using an FTIR-ATR system. Experiments were undertaken using 5µL mixtures containing trace amounts of butyl acetate diluted with oleic acid. Without the use of a metasurface, the minimum concentration of butyl acetate that could be clearly detected was 10%, whereas the use of the metasurface on the SiO_2/Si substrate allowed the detection of 1% butyl acetate.

Finally, graphene was integrated into a metasurface structure to achieve tunability of the design. The third device investigated was a phase modulator which shows the capability to change the amplitude and phase of the reflected wave by electrostatically gating the graphene from -90V to 90V. A dynamic beam steering lens model which is made up of a unit cell consisting of four phase modulator with different phase shift was also proposed to control the angle for the reflected wave from specular to 30°.

Contents

List of Figures i

List of Tables i

List of Publications i

1 Introduction 1

1.1 Motivation 1

1.2 Overview 3

2 Fundamental Concepts and Background 9

2.1 Introduction 9

2.1.1 Gas detection 11

2.1.2 Trace chemical detection 13

2.1.3 Infrared imaging and camouflage 15

2.2 Metasurfaces 18

2.2.1 Effective Medium Theory 21

2.2.2 Metasurface Applications 25

2.3 Graphene 34

2.3.1 Electronic Properties 34

2.3.2 Thermal Properties 42

3 Numerical Simulations 48

3.1 Introduction 48

3.2 Solving Maxwell's Equations 49
3.2.1 Finite Element Method 50
3.2.2 FDTD method 52
3.3 Simulation software and settings 54
3.3.1 Simulation Software 54
3.3.2 Material Properties 56
3.3.3 Boundary Conditions 58
3.3.4 Mesh sizes 60
3.4 Comparison between FEM and FDTD method 61
4 Device Fabrication 64
4.1 Introduction 64
4.2 Metasurface fabrication 65
4.2.1 Electron beam lithography 65
4.2.2 Metallization 68
4.3 2D-material fabrication 70
4.3.1 2D material transfer 70
4.3.2 Reactive ion etching 72
4.4 Fabricated Devices 74
5 Characterisation 75
5.1 Introduction 75

5.2 Metrology 76
5.2.1 Optical Microscopy 76
5.2.2 Scanning Electron Microscopy 76
5.2.3 Atomic Force Microscopy 79
5.3 Electromagnetic response characterization 82
5.3.1 Transmission Measurement 82
5.3.2 Reflection measurement 84
5.3.3 Emission measurement 87
5.3.4 Attenuated total reflection Measurement 89
5.4 Conclusion 92
6 Metamaterial-based Graphene Thermal Emitter 93
6.1 Introduction 93
6.2 Design 96
6.2.1 Single Band Emitter 96
6.2.2 Dual Band Emitter 102
6.3 Fabrication 105
6.4 Reflection Measurement 109
6.5 Emission Measurement 114
6.6 Quality Factor Improvement 118
6.7 Summary 121

7 Wave Trapping Sensor for Attenuated Total Reflection Spectroscopy 123

7.1 Introduction 123

7.2 Modelling 127

7.2.1 Modelling of ATR configuration 127

7.2.2 Modelling of the device 130

7.3 Fabrication and Measurement 136

7.3.1 Device Fabrication and Measurement 136

7.3.2 Chemical Analytes Measurement 140

7.3.3 Measurement of Chemical Analytes with metasurface devices 143

8 Graphene-based Mid-infrared Modulator 149

8.1 Introduction 149

8.2 Design 151

8.3 Experiment 158

8.4 Application 164

8.5 Summary 168

9 Conclusions and Outlook 170

9.1 Conclusions 171

9.1.1 Metasurface-based Narrowband Graphene Thermal Emitter 171

9.1.2 Metasurface-enhanced ATR Spectroscopy 172

9.1.3 Graphene based metasurface phase modulator 173

9.2 Outlook 174

9.2.1 Metasurface 174

9.2.2 Graphene 174

Bibliography 176

List of Figures

Figure 1.1 The propagation loss for conventional semiconductor material in Infrared wavelength range. Propagation loss more than 2 dB cm^{-1} is highlighted in orange (illustration taken from Ref [17]). 2

Figure 2.1 Absorption spectra for major natural greenhouse gases in the earth's atmosphere. From top to bottom: carbon monoxide, methane, nitrous oxide, ozone, carbon dioxide, semiheavy water vapour, water vapour and air (illustration taken from Ref. [42]). 12

Figure 2.2 A thin, switchable thermal camouflage film covered on hand(illustrations taken from Ref. [55]). 17

Figure 2.3 Number of publications on metamaterials (a) and different applications (b) of metamaterials between 2002 and 2012 (illustrations taken from Ref. [92]). 19

Figure 2.4 Schematics of the definition of (a)Transfer Matrix and (b)S parameters. 23

Figure 2.5 (b) propagation phase, (c) permittivity and (d) permeability retrieved from the negative refractive index metamaterial structure shown in (a) (illustrations taken from Ref. [62]). 24

Figure 2.6 (a) Schematic diagram of a 3-layer cross-resonator absorber and absorption spectra for (b) 1-layer cross structure; (c) 2-layer cross structure; (d) 3-layer cross structure (illustrations from Ref [76]). 28

List of Figures

Figure 2.7 Schematics used to derive the generalized Snell's law of (a) refraction and (b) reflection. 29

Figure 2.8 (a) top: phase and amplitude profile required for the beam steering lens, bottom: schematic of the resonator array for realizing the required phase distribution and simulations of the scattered electric field for the individual antennas composing the array (illustrations taken from [97]); (b) Flat focusing lens with consisting of V-shaped nanoantenna array and the transverse cross-section of its intensity profiles (illustrations taken from [102]). 33

Figure 2.9 (a) Graphene lattice structure. Each original cell contains two symmetrical and inequitable carbon atoms A and B,(b) Graphene electronic band structure obtained in the tight-binding model; the valence and conduction bands connect in the Brillouin area (illustration taken from Ref [143]). 36

Figure 2.10 Resistivity of graphene as a function of gate voltage at 1K. The insets indicate changes in the position of the Fermi energy E_F with varying gate voltage V_g (illustration taken from Ref [161]). 38

Figure 2.11(a) Real parts of intraband (solid lines) and interband (dash lines) surface conductivities of graphene with $|E_F|$ = 0.2 eV (in black) and $|E_F|$ = 0.4 eV (in red). The inset shows the band structure of graphene. (b) The optical

response of moderately doped graphene in different spectral ranges (illustrations from Ref [163]). 41

Figure 2.12 Phonon dispersion diagram of single-layer graphene along the Γ-to- M crystallographic direction (illustration taken from Ref [136]). 44

Figure 2.13 (a) Spatial images of the integrated infrared emission from graphene channels with different gate voltage, (b) Corresponding I-V characteristic, (c) Infrared intensity profile along the length of the graphene sample, (d) More localized hotspot with bias graphene on a substrate with thinner oxidized layer ((a-c) taken from Ref. [177], (d) taken from Ref. [178]). 47

Figure 3.1 Geometry for 2D and 3D meshes (elements) in COMSOL. 51

Figure 3.2 (a) A graphical representation of a central-difference approximation to the gradient at a point x_0 (b). Illustration of a standard Cartesian Yee cell used for FDTD which is composed of an electric cell and a magnetic cell staggering in space (illustration taken from [188]). 53

Figure 3.3 The Lumerical FDTD Solutions model of the unit cell of graphene-based metasurface modulator as introduced in Chapter 8. 59

Figure 3.4 The automatically generated mesh for a sphere with 5 μm radius in (a) Lumerical FDTD Solutions (mesh setting: level 4) and (b) COMSOL Multiphysics (mesh setting: normal). 63

List of Figures

Figure 4.1 Schematic diagrams of the lithography processes on positive resist (top row) or negative resist (bottom row). 66

Figure 4.2 Schematic diagram of metallization process on an EBL patterned sample. 69

Figure 4.3 Schematic diagram of transferring of CVD 2D material grown on Cu foil to a Si/SiO_2 substrate. 71

Figure 4.4 Schematic diagram of etching 2D material transferred on Si/SiO_2 substrate. 73

Figure 5.1 Schematic diagram of SEM working principle (illustration taken from [194]). 78

Figure 5.2 Images of a split ring resonator structure proposed in Chapter 8 measured under (a) optical microscope and (b) SEM by using a secondary electron detector. 79

Figure 5.3 Schematic diagram of AFM working principle (illustration taken from [196]). 81

Figure 5.4 (a)2D image and (b)3D image of ring resonators on an h-BN encapsulated graphene filament..... 81

Figure 5.5 Schematic diagram and beam path of a Bruker Vertex 80v FTIR spectroscopy (illustration taken from [198]). 83

Figure 5.6 The external setup of FTIR spectroscopy for reflection measurement. ... 85

Figure 5.7 The external setup of FTIR spectroscopy for emission measurement..... 87

Figure 5.8 (a) Bruker Platinum ATR module (illustration taken from [199]) (b) Schematic diagram of the mechanism of ATR measurement. 91

Figure 6.1 (a) 3D schematic and (b) top view of the unit cell of the design modelled in the simulation. 97

Figure 6.2 Simulated transmission (black line), reflection (red line) and absorption spectrum of the unit cell of single annular ring resonator on the top of h-BN encapsulated graphene thermal emitter..... 99

Figure 6.3 Cross sectional electric field distribution (colour plot) and surface current (red arrows) in x-y plane between metasurface and substrate at λ = 4.4 μm. 100

Figure 6.4 (a) Simulated absorption/emission spectra of single annular ring resonator unit cell with different radii ranges from 100 nm to 400 nm. (b) The resonance wavelength of single annular ring resonator as a function of radius of the annular ring resonator. 101

Figure 6.5 (a) Top view and (b) simulated emission spectrum of double annular ring resonator designs for dual band metasurface-based graphene thermal emitter. 103

Figure 6.6 (a) Electric field and (b) surface current distributions in x-y plane between the metasurface and substrate at 4.2 μm, (c) Electric field and (d) surface

current distributions in x-y plane between the metasurface and substrate at 6.6 μm 104

Figure 6.7 The cross section diagrams of fabricating the sample (i)-(vi): Formation of the emission area. (vii)-(xii): Deposition of first and second contact on outer edge. (xiii)-(xv) Transfer of top layer h-BN. (xvi)-(xix) Evaporation of contact pads and metamaterial ring resonators. 107

Figure 6.8 (a) Top view of the schematic illustration of graphene narrowband thermal emitter with quadrants. (b) Microscope image taken at 50× magnification of the top of the emitter. (c) AFM image taken from within the red dash box shown in (b). 108

Figure 6.9 Measured spatial variation of the total reflection intensity from the surface of GTE_MM_2 on a logarithmic scale. 110

Figure 6.10 Measured reflection spectra of gold mirror reference (red dash lines), quadrants without metasurface (black dash lines) and quadrants with metasurface (solid lines in different colors) from (a) GTE_MM_1; (b) GTE_MM_2; (c) GTE_MM_3; (d) GTE_MM_4..... 112

Figure 6.11 Normalized (red solid lines) and simulated (blue solid lines) reflectance of the quadrants with metasurface and normalized reflectance (black dash lines) of quadrants without metasurface from (a) GTE_MM_1, (b) GTE_MM_2, (c) GTE_MM_3, (d) GTE_MM_4..... 113

Figure 6.12 Measured spatial variation of the total emission intensity from the surface of GTE_MM_2 on a logarithmic scale. 115

Figure 6.13 Measured emission spectra of quadrants without metasurface (black dash lines) and quadrants with metasurface (solid lines in different colors) from (a) GTE_MM_1; (b) GTE_MM_2; (c) GTE_MM_3; (d) GTE_MM_4.. 116

Figure 6.14 Normalized (solid lines with different colors) and simulated (black solid lines) emissivity of the quadrants with metasurface from (a) GTE_MM_1, (b) GTE_MM_2, (c) GTE_MM_3, (d) GTE_MM_4. 117

Figure 6.15 (a) and (b) Emission spectra for substrates with different conductivities. (c) Calculated radiation spectrum of the metamaterial-based graphene thermal emitter on an aluminium substrate (blue line) based on the measured radiation spectrum of a bare graphene thermal emitter (red line). 119

Figure 6.16 Calculated Q-factors of both emission peaks (blue line for 1st emission peak and red line for 2nd emission peak) for substrates with different conductivities. 120

Figure 7.1 (a) 3D schematic of the simulation model used to generate evanescent wave with incident wave propagates along z-axis with an angle of incidence θ and electric field polarized along x-axis. (b)The electric field

distribution in x-z plane at k = 1000 cm^{-1} with incident angle = 10° (left) and 45° (right). 127

Figure 7.2 Reflectance obtained from the simulation model as a function of incident angle. 129

Figure 7.3 (a) 3D perspective view and (b) top view with geometric parameters of the device proposed for enhancing the sensitivity of ATR spectroscopy. 130

Figure 7.4 (a) Simulated reflectance spectra of the metasurface on Si substrate (b) and (c) shows the electric field distribution for x-y plane at 450 cm^{-1} (dipole mode) and 860 cm^{-1} (quadrupole mode)..... 131

Figure 7.5 Simulated dispersion diagram of metasurface on Si/SiO_2 substrate. The two red dashed lines show the calculated resonance frequencies (dipole mode and quadrupole mode) of uncoupled metasurface. The three black dash lines represent frequencies of three surface optical phonon modes in SiO_2. The vertical white line represents the spectral response of the metasurface on Si/SiO_2 substrate presented in this paper. 134

Figure 7.6 Comparison between the reflection spectra of metasurface on Si substrate (black line) and on Si/SiO_2 substrate (red line). 135

Figure 7.7 (a) the SEM photo of ATR-Si-M01; (b) measured reflectance spectra of ATR-Si-M01 and ATR-SiO_2-M01 under ATR configuration. 138

Figure 7.8 (a) Measured reflection spectra of metasurface with different scales on Si/SiO_2 substrate in the ambient atmosphere, spectra are consecutively shifted by 0.25 vertically for clarity; (b) dispersion diagram as shown in Figure 7.5 with extracted wavenumber of maxima and minima overlaid. ▼ and ▲ in blue, red and black corresponding to the maxima and minima observed in the spectrum of ATR-SiO_2-M03, ATR-SiO_2-M01, and ATR-SiO_2-M02 respectively. 139

Figure 7.9 Measured absorption spectra of (a) 99.9% oleic acid and (b) 99.9% butyl acetate. 140

Figure 7.10 Measured absorption spectra for mixtures in the ambient atmosphere, spectra are consecutively shifted by 0.5 vertically for clarity; (b) Extinction spectra for mixtures without the presence of metasurface. 142

Figure 7.11 (a) Measured absorption spectra of mixtures in the presence of ATR-Si-M01 in the ambient atmosphere, spectra are consecutively shifted by 0.2 vertically for clarity; (b) zoomed extinction spectra of mixtures in the presence of ATR-Si-M01 for the carbon oxygen stretching band region between 800 cm^{-1} and 1200 cm^{-1}. 144

Figure 7.12 (a) Measured absorption spectra of mixtures in the presence of ATR-SiO_2-M01 in the ambient atmosphere, spectra are consecutively shifted by 0.2 vertically for clarity; (b) zoomed extinction spectra of mixtures in the

presence of ATR-SiO_2-M01 for the carbon–oxygen stretching band region between 800 cm^{-1} and 1200 cm^{-1}..... 146

Figure 8.1 schematic of the graphene metasurface modulator (a) 3D view, (b) equivalent circuit diagram (c) top view..... 152

Figure 8.2 Calculated conductivity of non-doped ($|E_F|$ = 0 eV) and doped ($|E_F|$ = 0.4 eV) monolayer graphene-based on simplified Kubo formula..... 154

Figure 8.3 Reflection and normalized effective impedance spectra of designs with (a) non-doped graphene ($|E_F|$ = 0 eV); (b) doped graphene ($|E_F|$ = 0.4 eV). Minimum of reflection occurs when the normalized effective impedance equals to 1 (Z_{eff}/Z_0 = 1). 155

Figure 8.4 (a) Simulated reflection spectra and (b) retrieved phase information of reflection from designs with Fermi level of graphene ranging from 0 eV (non-doped) to 0.4 eV (doped). 157

Figure 8.5 cross-sectional normalized electric field distribution at 60THz in the x-y plane (left) and in the x-z plane intersecting the gap of SRRs (right). 158

Figure 8.6 (a) SEM image and (b)photograph of the fabricated device..... 159

Figure 8.7 (a) schematic of the field effect characteristic measurement setup (b) Field effect characteristic curves of graphene with metasurface patterned on the top and without metasurface on the top..... 161

Figure 8.8 Spatially resolved reflectance map from the graphene metasurface modulator (b) Measured Reflection Spectra of graphene metasurface modulator with gate voltage ranging from -90 V to 60 V (V_{CNP}). 162

Figure 8.9 Extracted resonance frequency as a function of gate voltage, the same extracted simulation data is also presented here for comparison. For the simulation curve, the gate voltage is converted from the Fermi level by Equation (2.15). (Lines are guided for the eye and not fitted curves) 163

Figure 8.10 (a) Schematic of two adjacent super cells of beam steering lens constructed by four modulators with different geometric parameters to achieve the necessary reflection phases. (b) The phase profile along x-axis at f = 60 THz for non-doped and doped graphene devices shown in (a). 166

Figure 8.11 Numerical simulations of scattering farfield pattern of non-doped graphene (a) and doped graphene device (b), showing specular and anomalous reflection at f = 60 THz respectively..... 167

List of Tables

Table 2.1 Characteristic absorption frequencies of common organic functional groups. (Ref [46]) 14

Table 4.1 List of fabricated devices characterized and discussed in this thesis 74

Table 6.1 A list of double annular ring resonators based emitters with different geometric parameters for fabrication and measurement. λ_1 and λ_2 are the theoretical resonance wavelengths related to the large annular ring resonators and small annular ring resonators. 105

Table 7.1 List of devices fabricated and measured in the experiment as well as their geometric parameters..... 136

Table 8.1 Geometric parameters of modulators used in beam steering lens 166

List of Publications

[1] Shi, C., Luxmoore, I. J., & Nash, G. R. Gate tunable graphene-integrated metasurface modulator for mid-infrared beam steering. *Optics Express* **27**, 14577-14584 (2019).

[2] Shi, C., Luxmoore, I. J., & Nash, G. R. Graphene-based Metamaterial Tunable Phase Modulator for Mid-Infrared Wave Steering. In *CLEO2019* JTh2A-26 (2019).

[3] Shi, C., Penrose, C., Pitts, J. E., Gowda, P., Luxmoore, I. J., & Nash, G. R. Metamaterial-enhanced infrared attenuated total reflection spectroscopy. *Nanoscale Advances*, **1**, 476-480 (2019).

[4] Shi, C., Mahlmeister, N.H., Luxmoore, I.J. and Nash, G.R., Metamaterial-based graphene thermal emitter. *Nano Research* **11**, 3567-3573 (2018).

[5] Shi, C., Zang, X. F., Ji, X. B., Chen, L., Cai, B., Nash, G. R., & Zhu, Y. M. Compact broadband terahertz perfect absorber based on multi-interference and diffraction effects. *IEEE Transactions on. Terahertz Science and Technologies* **6**, 40–44 (2016).

1 Introduction

1.1 Motivation

The mid-infrared (MIR) spectral region of 2-20 μm contains strong characteristic vibrational transitions of many important molecules [1,2] as well as two atmospheric transmission windows between 3-5 μm and 8-13 μm [3], which makes it crucial for applications in spectroscopy [4-7], materials processing [8], chemical and bio-molecular sensing [9,10], security and industry [11]. Although there is a huge variety of potential applications in the mid-infrared regime, research on efficient MIR functional devices still remains challenging [12]. First of all, with the development of infrared industries, more sensitive and cost-effective devices are required for precise measurements. In addition, the idea of making infrared systems portable or handheld so that people can use those systems doing measurement and analysis directly on-site attracts increasing research interest [13-15]. This requires the components in the system to be designed as compact and integrable, but to remain cost-effective and feasible for fabrication. It is already not a trivial thing to fulfil only the latter two requirements simultaneously, let alone taking addition consideration of

portability and reliability into the design. Besides, mid-infrared devices are restrained by a limited choice of conventional optical elements. Although optical glass is widely used in fabricating optical devices as it can achieve nearly 100% transparency in optical wave band, its high transmission is limited to the wavelength less than 3.5 μm due to the vibrational modes associated with oxygen [16]. As shown in Figure 1.1, most of Group III or Group IV compounds have their cutoff frequencies in the mid-infrared regime. Although silicon and germanium have a relatively wide range of transmission window in the mid-infrared band, the energy propagated through these materials will be reduced by more than 50% due to their high refractive indices (n_{Si} = 3.7, n_{Ge} = 4.05) [17]. Besides, other chemical compounds like calcium fluoride (CaF_2), potassium bromide (KBr), barium

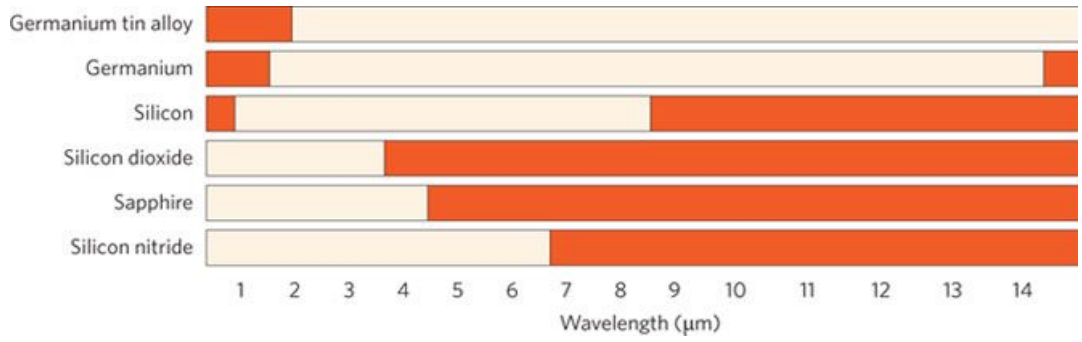

Figure 1.1 The propagation loss for conventional semiconductor material in Infrared wavelength range. Propagation loss more than 2 dB cm^{-1} is highlighted in orange (illustration taken from Ref [17]).

fluoride (BaF_2) have a broad transmission window as well as a high transmittance [18], but their softness and crystalline solid-state structures made it extremely difficult to be patterned on the surface, and are thus difficult to use in the fabrication of certain devices.

As a highly significant breakthrough, metasurfaces have been developed as promising building blocks in designing optoelectronic devices, by delicately engineering parameters or materials of those individual building blocks and selecting specific design algorithms. Furthermore, when integrating 2D materials like graphene into the metasurface, even more exceptional applications can be realized like thermal management, modulation, etc. Metasurface-based devices are promising to replace their conventional opponents due to their better performance and compact size.

1.2 Overview

The main results presented in this thesis are the study on the design, fabrication, and characterization of three different metasurface-based devices in the mid-infrared regime. The first device is an h-BN/graphene encapsulated incandescent mid-infrared emitter with metasurface structure integrated on the top. The second device is designed to enhance the

measurement sensitivity of attenuated total reflection (ATR) mid-infrared spectroscopy. The third device demonstrated is the active mid-infrared reflective modulator, whose performance can be tuned by changing the gate voltage applied on the device. Performances of all three devices are simulated and optimized by utilizing commercial software, Lumerical FDTD Solutions, which is based on finite difference time domain (FDTD) method and COMSOL Multiphysics, which is on the basis of finite element method (FEM). Devices were then fabricated in an ISO Class 5 cleanroom by following a set of delicate processes, followed by testing via a powerful Fourier Transform Infrared (FTIR) Spectroscopy. The measurement results, which are in good agreement to the simulation results, demonstrate the potential applications of those metasurface based mid-infrared devices in areas such as gas sensing, trace chemical detection, and thermal imaging. The rest of this thesis is structured as follows:

Chapter 2 gives background information on metasurfaces and graphene, two key elements in our device designs. The first section introduces some common strategies to design metasurfaces at the desired frequency, including details on the effective medium theory, as well as using this theory to design metasurface for perfect absorbers and ultrathin lenses. This is followed by a discussion on one of the most promising 2D

materials, graphene. Information on both electrical and thermal properties of graphene will be covered.

Chapter 3 presents details on two main simulation methods, the FEM and the FDTD method, which we applied to simulate the response of our devices presented in this thesis. Introduction to each method, and their settings for material properties, mesh sizes and boundary conditions are also discussed in this chapter.

Chapter 4 provides descriptions of the methodology involved in the fabrication of the devices presented in the thesis. The chapter will start with background information on the fabrication process of a metasurface structure on a substrate, including electron beam lithography, and thermal evaporation. This introduction is followed by the descriptions on the transfer the transfer process of chemical vapour deposition (CVD) 2D materials like graphene and hexagonal boron nitride (h-BN) to various substrates along with the patterning process by using reactive ion etching machine.

Chapter 5 introduces different kinds of set-ups of the Fourier transform infrared spectroscopy measurement systems used in the experiments, covering transmission (characterization for substrate), reflection (characterization for active reflective modulator), emission

(characterization for metasurface-based graphene thermal emitter), ATR (characterization for chemicals and wave trapping sensor for chemical detection),with background information of on the Bruker FTIR spectroscopy provided.

Chapter 6 investigates how the metasurface layer applied as a frequency selective surface (FSS) to tailor the thermal radiation spectrum from multilayer graphene infrared emitters. It was observed that CVD multilayer graphene can be thought of like a classic filament bulb with uniform channel resistance, but could be driven with much higher frequency, up to 100 kHz [19]. In order to obtain a narrowband emission spectrum, a metasurface structure is integrated into the CVD multilayer graphene infrared emitter. By comparing the measured spatial variations and spectra of the thermal emission from both patterned and unpatterned multilayer graphene infrared emitter, distinct differences can be noticed. The possibility of increasing the quality factor (Q factor) by integrating another metallic back-reflector layer is also investigated. An adapted form of this part of the chapter was published in Nano Research **11**, (2018) [20].

Chapter 7 begins with a full detailed introduction on our COMSOL model which is built to simulate the condition of an ATR setup. Research

on enhancing the detection of trace chemicals in a commercial attenuated total reflection setup is also demonstrated in this chapter. An array of periodic subwavelength metallic complimentary ring resonators patterned as metasurface layer on different substrates are investigated to improve the sensitivity of FTIR-ATR measurement. Geometric parameters of the metasurface structure are designed to ensure the resonance frequency of metasurface overlapping one of the vibrational modes of the analytes. This overlap will result in a strong interaction between the electromagnetic wave confined in the air gap and chemical analytes trapped there. An even stronger interaction is observed for an oxidized silicon substrate, due to the aforementioned two resonance modes coupling into the phonon mode of SiO_2. More details can be referred to our publication in the associated journal, Nanoscale Advances, **1** (2019) [21].

Chapter 8 shows our design on combining the metasurface structure and graphene as a whole active reflective modulator in the mid-infrared regime. Graphene, well known for its unique gapless bandstructure, introduces a wide range of tunable conductivity to the device for modulation. 300 nm thick SiO_2 on an aluminium covered Si substrate is used in device fabrication so that the graphene conductivity can be directly controlled by the gate voltage applied on the aluminium layer.

Preliminary results show a 150° modulation in phase can be achieved at 60THz by altering the gate voltage from -90V to 90V. In the second section, we show the application of a beam-steering lens by constructing four such modulators but with different geometric parameters as a new unit cell. Due to a 0 to 2π phase variation over the unit cell will be established as soon as the gate voltage is applied, our simulation results show that the biased device will reflect the beam with an extra 30° compared to when the device is unbiased. Parts of the results presented in this chapter have been published in CLEO proceedings 2019 [22] and Optics Express, **27** (2019) [23].

Chapter 9 summarizes the results presented in this thesis in addition to provides outlooks on the future development of metasurfaces and graphene.

2 Fundamental Concepts and Background

2.1 Introduction

In this chapter, we introduce three main applications of mid-infrared light: gas sensing, chemical detection, and thermal imaging. However, these applications are hindered by the relatively poor performance of mid-infrared optoelectronic devices which suffers from slowing responding time, poor sensitivities, and lack of flexibility. Thus, not only powerful but also compact and improved devices are required to promote the development of the infrared industry. However, advances in material sciences are opening up new routes to achieve this goal. Among these materials, metasurfaces and graphene are essential building blocks of the devices explored in this research due to their unique properties and ultrathin thicknesses. Metasurfaces, the planar form of metamaterials, which can be regarded as a homogeneous layer with artificial electromagnetic properties will be introduced in Section 2.2. Electromagnetic properties like permittivity and permeability can be precisely extracted with the assistance of effective medium theory, which will be described in detail in § 2.2.1. The retrieved values are crucial for the design and analysis of the metasurface devices. In § 2.2.2, research on two applications based on

metasurfaces, perfect absorbers and ultrathin flat lenses will be reviewed to show how infrared light can be controlled by such a thin layer of structures. In Section 2.3, the electronic and thermal properties of graphene will be discussed. Due to the high carrier mobility of graphene and the fact that graphene can be easily doped by electrons and holes through electrostatic gating or chemical doping, the graphene-integrated device's response to the electromagnetic wave could be directly controlled by the doping level of graphene within a response time less than 1 ns [24], which is a great breakthrough for applications like modulators.

Most of the objects around us are composed of nothing but molecules which in turn are formed by atoms linked together through either covalent bonding or ionic bonding [25]. If we regard the bonding as a massless spring, the atoms vibrate along with the spring and rotating around the axis. When light is incident on a substance, the radiation is transmitted, reflected or absorbed in varying degrees, depending upon the substance and the wavelength of the radiation [26]. At the atomic and molecular level, when a molecule is excited by a photon, the energy of the photon is absorbed by the molecule. Each molecule can vibrate and rotate in certain patterns, and for each pattern, there is an associated amount of energy of motion [10]. A molecule can only absorb energy from a photon if the energy matches precisely such an energy state of that

molecule. Notably, the frequencies of these energy states are mostly located in the mid-infrared band, particularly in 2-8 μm [27] which is one of the reasons why the mid-infrared range has attracted so many research interests. For the last two decades, mid-infrared devices have been widely used in a commercial infrared system for such applications as environment monitoring [28-30,35], organic matter analysis [36], medical diagnostics [37,38], and thermal imaging [39-41], etc.

2.1.1 Gas detection

For many gases, there are a large number of photon energies in the mid-infrared range that can be absorbed by gas molecules: As depicted in Figure 2.1, each gas exhibits a very specific set of absorption wavelengths which depend on the strength of the chemical bonds between the atoms that make up the molecule. Unlike diatomic molecules composed of like atoms such as oxygen (O_2), hydrogen (H_2), chlorine (Cl_2), and nitrogen (N_2) or infrared transparent inert gases (He, Ne, Ar, Kr, Xe, Rn) which oscillate at shorter wavelength such as ultraviolet and X-rays, greenhouse gas molecules like carbon dioxide (CO_2), nitrogen dioxide (NO_2) or methane (CH_4) exhibit oscillation modes that match the energy of mid-infrared radiation. The oscillation modes might be stretching and bending motions. It is this selective

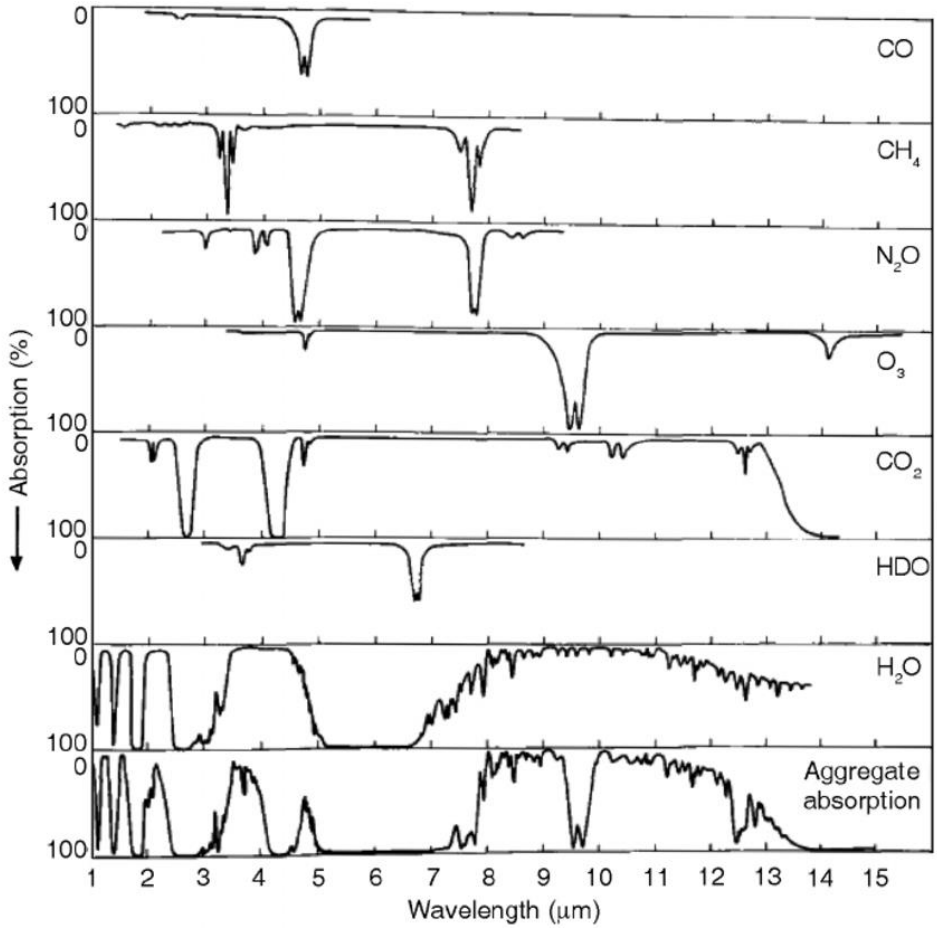

Figure 2.1 Absorption spectra for major natural greenhouse gases in the earth's atmosphere. From top to bottom: carbon monoxide, methane, nitrous oxide, ozone, carbon dioxide, semiheavy water vapour, water vapour and air (illustration taken from Ref. [42]).

absorption of radiation which forms the basis for detecting a gas and for measuring its concentration [28-35]. In order to get a real-time, accurate reading to predict the concentration of certain gas, powerful and robust handheld infrared systems are demanded. The metasurface graphene thermal

emitter proposed in this thesis, a robust source for handheld infrared systems has the potential to be much more cost-effective than MIR-LED sources and faster and more compact than tungsten filament based sources. The source is designed as a dual-band source which is particularly advantageous for gas-sensing applications, with one emission peak at the wavelength of the atmospheric transparent window providing a reference, and the other resonance wavelength with the absorption of the target gas. It should be noted that these emission peaks can be located at arbitrary frequencies by changing the geometrical parameters of design, so that it is suitable for all gas detection applications, includes monitoring the density of methane in mining [31,34], detecting the carbon dioxide emission from the factory [35] or automotive [29] and also analysis the gas pollutant in the environment [30].

2.1.2 Trace chemical detection

Another important application for mid-infrared devices is trace chemical detection which can be used in chemical and biological sensing [4,26,32,37,38]. Organic matter is built from four essential elemental ingredients: carbon, hydrogen, oxygen and nitrogen [43]. The atoms of these four elements are very likely to be covalently bonded together so as to make their valence shell complete and thus form into different functional groups. Furthermore, the

carbon atom can form long chains, known as carbon skeleton, which connect different carbon-based functional group and build up more complicated organic compounds. Researchers have successfully identified the absorption peaks for hundreds of organic compound in the mid-infrared regime in the past several decades [44,45], they also found that some functional groups absorb infrared radiation at about the same wavelength. For instance, as demonstrated in Table 2.1, there are three similar hydrogen stretching groups, alkanes (-C-H), carboxylic acids (-O-H) and amines (-N-H). Alkane stretching vibrations

Functional group	Type of vibration	Characteristic absorptions (cm^{-1})	Intensity
Alcohol			
O-H	Stretch, H-bonded	3200-3600	Strong, broad
O-H	Stretch, free	3500-3700	Strong, sharp
C-O	Stretch	1050-1150	Strong
Alkane			
C-H	Stretch	2850-3000	Strong
-C-H	Bending	1350-1480	Variable
Alkene			
=C-H	Stretch	3010-3100	Medium
=C-H	Bending	675-1000	Strong
C=C	Stretch	1620-1680	Variable
Alkyl halide			
C-F	Stretch	1000-1400	Strong
C-Cl	Stretch	600-800	Strong
C-Br	Stretch	500-600	Strong
C-I	Stretch	500	Strong
Alkyne			
C-H	Stretch	3300	Strong,sharp
C≡C	Stretch	2100-2260	Variable, not present in symmetrical alkynes
Amine			
N-H	Stretch	3300-3500	Medium (primary amines have two bands; secondary have one band, often very weak)
C-N	Stretch	1080-1360	Medium-weak
N-H	Bending	1600	Medium
Aromatic			
C-H	Stretch	3000-3100	Medium
C=C	Stretch	1400-1600	Medium-weak, multiple bands
Analysis of C-H out-of-plane bending can often distinguish substitution patterns			
Carbonyl			
C=O	Stretch	1670-1820	Strong (conjugation moves absorptions to lower wave numbers)
Ether			
C-O	Stretch	1000-1300 (1070-1150)	Strong
Nitrile			
C-N	Stretch	2210-2260	Medium
Nitro			
N-O	Stretch	1515-1560 and 1345-1385	Strong, two bands

Table 2.1 Characteristic absorption frequencies of common organic functional groups. (Ref [46])

usually appear between 3200 and 2800cm^{-1}, carboxylic acids stretching vibrations occur between 3650 and 3600cm^{-1}, and amines stretching vibrations locate between 3500 and 3300cm^{-1}. These types of infrared bands are called group frequencies because they tell us about the presence or absence of specific functional groups in a sample [45]. However, quantifying the concentration of those chemicals are far more difficult than qualifying them as the sensitivity of the most advanced spectroscopy techniques is limited by the weak light-matter interaction caused by the size mismatch between molecules and the wavelength. The second device presented in this thesis, a metasurface sensor based on wave trapping, was used to demonstrate an improvement of ten-fold in trace chemical detection. This is potentially extremely important for studies of biological samples, including proteins, lipids, carbohydrates, and nucleic acids, where usually only a small amount of samples can be obtained for the study.

2.1.3 Infrared imaging and camouflage

Apart from the unique interaction with molecules, the infrared band is also widely used in imaging, especially when the visible condition is poor. Unlike light can easily be blocked by smoke and light fog, the infrared light is able to successfully penetrate through them. Thus infrared vision is used extensively

for night vision [47,48], navigation [49], surveillance [50,51] and rescue [52]. With advancements in infrared detection technology, there is also a growing need for infrared countermeasures like infrared camouflage [53-56]. Although during the past few years, the concept of invisibility [57-59] and illusion [60,61] has already been proposed and proven in microwave band on the basis of transformation optics and conformal mapping, it is impracticable to scale down those designs to make them function in the mid-infrared regime due to the challenge of fabricating such small features. Traditional thermal camouflage uses a low-emissivity coating, which reduces the object's apparent radiation temperature, to make the object blend into the background [53,54]. However, the emissivity of a traditional camouflage coating is fixed, and the objects can only be camouflaged in a fixed background temperature. Once the background temperature changes, the object can be easily detected by thermal imaging cameras because of the difference in radiation temperature between the object and the background. Realizing an effective adaptive thermal camouflage is not trivial as it requires a material that can adapt to different temperatures, and with an extremely fast response time. Some of the drawbacks limited the development of thermal camouflage so far include poor thermal fluctuation, slow response times, and the requirement for rigid materials, to name a few. Recent progress has been reported by O. Salihoglu *et al* which relies on electro-

modulation of IR absorptivity of multilayer graphene via reversible intercalation of non-volatile ionic liquids [55]. Their approach of using active infrared reflective modulators to perform as a reconfigurable surface covered on the object is able to change the radar cross-section (RCS) of the object or steer the wave to another angle to disguise the object from being seen by infrared cameras. A mid-infrared wave modulator is designed as the third device worked in this thesis. We also proved such design can be potentially used as a dynamic beam steering lens which is able to deflect the incident infrared light when driven by a gate voltage.

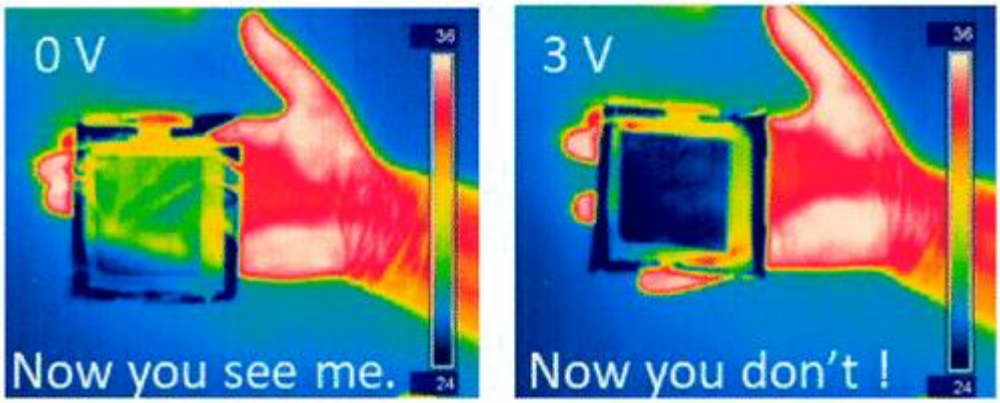

Figure 2.2 A thin, switchable thermal camouflage film covered on hand(illustrations taken from Ref. [55]).

2.2 Metasurfaces

The advent of metamaterials opens a new era for designing electromagnetic wave devices. Metamaterials are usually constructed by periodic unit cells, whose size and spacing are much smaller than the wavelengths of incoming electromagnetic radiation. Consequently, the electromagnetic wave does not experience the microscopic details of each unit cells, but treat it as a homogenous medium [62-65]. Thus engineering the nanostructure of metamaterials is equivalent to artificially design atoms to achieve electromagnetic properties that are not available or not easily obtainable in nature. As the chart shown in Figure 2.3, during the last 15 years, metamaterials have been the subject of an overwhelming interest in numerous publications in both highly focused and wider public journals, not only because of their unusual characteristics in wave propagation like negative permittivity [66], negative permeability [67], or negative refractive index [68,69], but also because their use in realizing such innovative applications as perfect absorbers [70-82], super-resolution imaging lens [83-89], invisible cloaks [57-59,90,91], and so on. Although those designs can be scaled up or down to resonance at any wavelength in the entire spectrum, most of these promising potential applications are still hindered in practice due to the high losses and strong

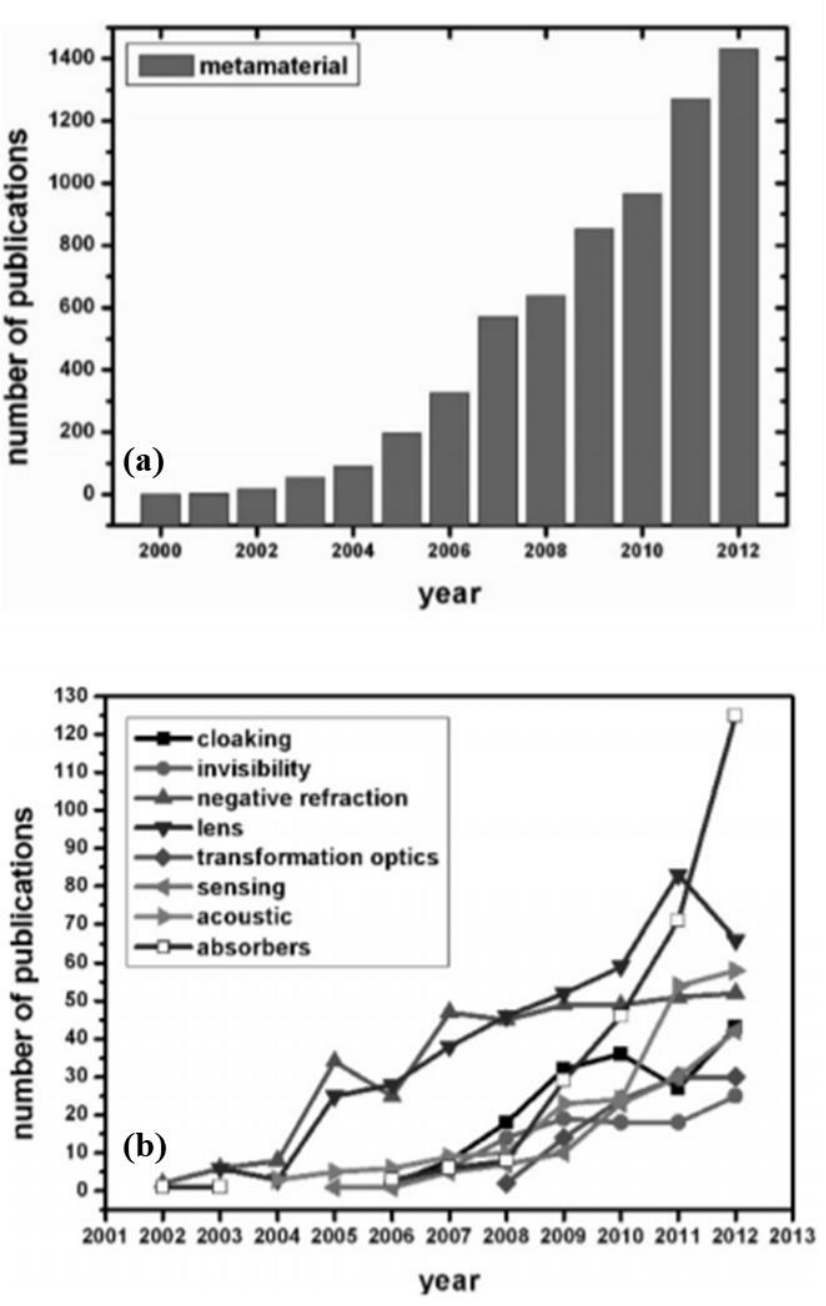

Figure 2.3 Number of publications on metamaterials (a) and different applications (b) of metamaterials between 2002 and 2012 (illustrations taken from Ref. [92]).

dispersion associated with the resonant responses and the use of metallic structures. In addition, whereas metamaterial-based devices can be easily fabricated for the microwave band, where the size of the features is in millimetre scale, it remains a huge challenge for realizing the required 3D structures in sub-micrometre scale, i.e. designs for infrared range or optical range. These two main obstacles of metamaterials drove many metamaterial researchers to focus on a single layer of planar structures, which were later termed as metasurfaces, that can be readily fabricated using existing technologies such as lithography and nanoimprinting methods. Meanwhile, the ultrathin thickness along the wave propagation direction can greatly reduce the unnecessary losses caused by the structure [93]. In general, metasurfaces can overcome the problems associated with metamaterials, while their interactions with incident waves can be still strong enough to provide very useful functionalities [94-96]. Over the past decade, metasurfaces have attracted great attention and have been proved to have the potential to replace 3D metamaterials in many applications in mid-infrared region, such as perfect absorbers [68-70,79,80], ultrathin lenses [97-103], holograms [104-106]. The metasurface can also be designed to enhance the electric field to improve the interaction between electromagnetic fields and objects [107,108], which is beneficial for applications

in mid-infrared band such as imaging, sensing, photovoltaics, and photo-emission [109–113].

2.2.1 Effective Medium Theory

Smith et al. first applied this practical method to assign bulk material properties to inhomogeneous metamaterials [62]. Suppose a beam of electromagnetic wave is propagating from one side of a metamaterial layer to the other. Assuming that the metamaterials perform like a homogenous medium with refractive index n and relative impedance z, the relation between the input electromagnetic field and the output electromagnetic field can be defined by the transfer matrix method as

$$\boldsymbol{A}_{out} = \boldsymbol{T}\boldsymbol{A}_{in} \tag{2.1}$$

where

$$\boldsymbol{T} = \begin{bmatrix} \cos\ nkd & -\dfrac{z}{k}\sin\ nkd \\ \dfrac{k}{z}\sin\ nkd & \cos\ nkd \end{bmatrix} \tag{2.2}$$

d is the thickness of the slab and $k = 2\pi/\lambda$ is the wavevector. However, for metasurfaces, the transfer matrix $\boldsymbol{T}$ cannot be evaluated because of a lack of knowledge of its n and k. An alternative approach is to calculate the transfer matrix using the scattering parameters (S-parameters) extracted from

simulations. The S-parameters, as shown in Figure 2.4, link the incoming field amplitudes to the outgoing field amplitudes and can also be directly related to experimentally determined quantities. The elements of the transfer matrix can be expressed by the values of S-parameters as follows:

$$\begin{aligned} T_{11} &= \frac{1+S_{11}\ \ 1-S_{22}\ \ +S_{12}S_{21}}{2S_{21}}, \\ T_{12} &= ik\frac{1+S_{11}\ \ 1+S_{22}\ \ -S_{12}S_{21}}{2S_{21}} \\ T_{21} &= \frac{1}{ik}\frac{1-S_{11}\ \ 1-S_{22}\ \ -S_{12}S_{21}}{2S_{21}} \\ T_{22} &= \frac{1-S_{11}\ \ 1+S_{22}\ \ +S_{21}S_{12}}{2S_{21}} \end{aligned} \tag{2.3}$$

Because the medium is assumed to be homogenous, so that we can get $S_{11} = S_{22}$ and $S_{21} = S_{12}$, the equations can be simplified into：

$$\begin{aligned} T_{11} &= T_{22} = \frac{1-S_{11}^2+S_{21}^2}{2S_{21}}, \\ T_{12} &= ik\frac{1+{S_{11}}^2-S_{21}^2}{2S_{21}} \\ T_{21} &= \frac{1}{ik}\frac{1-{S_{11}}^2-S_{21}^2}{2S_{21}} \end{aligned} \tag{2.4}$$

Using the analytic expression for the T-matrix elements in Equation (2.2) gives the refractive index n and relative wave impedance z of the effective medium in terms of S-parameters:

$$\begin{aligned} n_{eff} &= \frac{1}{kd}\cos^{-1}\left(\frac{1-S_{11}^2+S_{21}^2}{2S_{21}}\right) \\ z_{eff} &= \sqrt{\frac{1+{S_{11}}^2-S_{21}^2}{1-{S_{11}}^2-S_{21}^2}} \end{aligned} \tag{2.5}$$

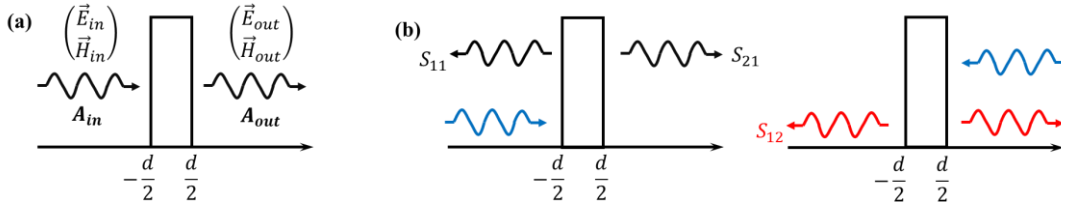

Figure 2.4 Schematics of the definition of (a)Transfer Matrix and (b)S parameters.

Finally the effective relative permittivity and permeability of the metamaterials can be obtained based on n and z by the relations:

$$\varepsilon_r = \frac{n_{eff}}{z_{eff}} = \sqrt{\frac{1 - S_{11}^{\ 2} - S_{21}^2}{k^2 d^2\ 1 + S_{11}^{\ 2} - k^2 d^2 S_{21}^2}} \cos^{-1}\left(\frac{1 - S_{11}^2 + S_{21}^2}{2S_{21}}\right)$$
$$\mu_r = n_{eff} z_{eff} = \sqrt{\frac{1 + S_{11}^{\ 2} - S_{21}^2}{k^2 d^2\ 1 - S_{11}^{\ 2} - k^2 d^2 S_{21}^2}} \cos^{-1}\left(\frac{1 - S_{11}^2 + S_{21}^2}{2S_{21}}\right) \quad (2.6)$$

Figure 2.5 shows the effective relative permittivity, permeability and phase information extracted from the negative index metamaterial proposed in Ref [114]. As can be directly observed that the structure has a negative value of permittivity for the frequency below 12 GHz as well as negative permeability between 9 GHz to 11 GHz. It can also be noted that the phase of the wave propagating through/reflecting from the metamaterials also varies along with the changes in permittivity and permeability. At the resonance frequency (f = 9.5 GHz), there is an abrupt change in the permittivity and permeability of the metamaterials which also dramatically changes the transmission/reflection

phase due to the resonance of the structure. This phase information can be extracted by calculating the phase of the S-parameters obtained from the simulation and then subtracting both the additional propagation phase from the wave source to the device and from the device to the monitor. These parameters retrieved from S-parameters are very helpful in designing metasurfaces for certain applications as will be introduced in the following section.

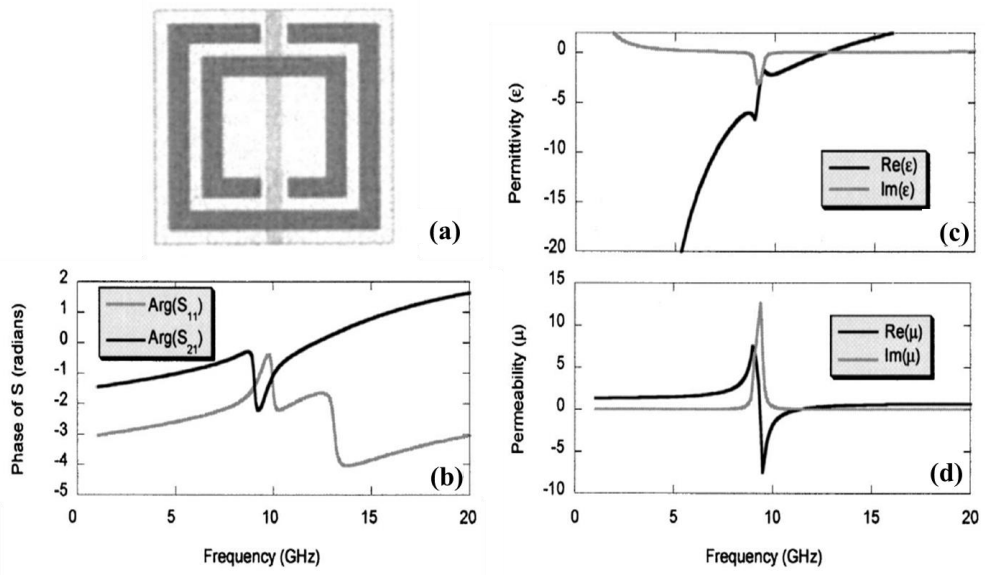

Figure 2.5 (b) propagation phase, (c) permittivity and (d) permeability retrieved from the negative refractive index metamaterial structure shown in (a) (illustrations taken from Ref. [62]).

2.2.2 Metasurface Applications

i) Metasurface absorbers

Metamaterial perfect absorbers, are one of the first metamaterial-based devices being realized for practical applications. High absorption is desired in many applications, such as energy harvesting [115,116], scattering reduction [117], as well as thermal sensing [118]. Near-unity absorption can be achieved by the use of a metallic ground plane to block all the wave propagating through the device while eliminating the entire reflection at the interface. According to the Fresnel formula of reflection, when a beam of wave incidents from air to a medium with refractive index n, the reflectivity (R) from the interface is [119]

$$\begin{aligned} \mathrm{R_{TE}} &= |r_{TE}|^2 = \left|\frac{\mu_r \cos\theta - \sqrt{n^2 - sin\theta}}{\mu_r cos\theta + \sqrt{n^2 - sin\theta}}\right|^2 \\ \mathrm{R_{TM}} &= |r_{TM}|^2 = \left|\frac{\varepsilon_r \cos\theta - \sqrt{n^2 - sin\theta}}{\varepsilon_r cos\theta + \sqrt{n^2 - sin\theta}}\right|^2 \end{aligned} \tag{2.7}$$

where the subscripts TE and TM refer to transverse electric (TE) and transverse magnetic (TM) polarized waves, θ is the angle of incidence. If we assume the normal incident condition, these equations can be reduced to:

$$\mathrm{R} = \frac{\mathrm{R_{TE}} + R_{TM}}{2} = \left|\frac{\sqrt{\mu_r} - \sqrt{\varepsilon_r}}{\sqrt{\mu_r} + \sqrt{\varepsilon_r}}\right|^2 = \left|\frac{\mathrm{Z_r} - 1}{Z_r + 1}\right|^2 \tag{2.8}$$

where $Z_r = \sqrt{\mu_r/\varepsilon_r}$ is the relative wave impedance. For classical electromagnetic absorbers, the permittivity and permeability of conventional materials won't support the reduction in reflection at the interface. Thus the approach adopted by those absorbers is to design a resonant cavity as an anti-reflection layer, for example, the design of Salisbury screens which consists of a thin resistive layer and a metal ground plane separated by a dielectric spacer of quarter wavelength thickness. In that case, the wave directly reflected from the interface will destructively interfere with the wave reflected through one round-trip propagation path and lead to the reduction in total reflection at a certain wavelength. However, the design is bulky and only can absorb energy over a narrow bandwidth. The mainstream design of metasurface absorbers inherits the three-layer Salisbury screen configuration, but replaces the top resistive layer by a metasurface. As mentioned in the effective medium theory, the metasurface can be treated as a homogenous layer with an effective relative permittivity and permeability. Research has shown that the effective relative permittivity of the metasurface is due to the electrical resonant response of individual elements in the metallic structure of the metasurface, and the effective relative permeability is attributed to the magnetic resonance resulting from anti-parallel surface currents between the top metasurfaces element and the ground plane [72,92]. The metasurface can thus be regarded as a

frequency selective surface (FSS) because it can fulfil the wave impedance matching condition, $z = Z_{eff}/Z_0 =$ 1, to eliminate the reflection at the artificial frequency by tailoring both ε_{r} and μ_r independently through adjusting the geometric dimensions of the metasurface structures and the thickness of the spacer layer. In comparison to the conventional absorbers, the thickness of metasurface absorbers can be dramatically reduced because the dielectric spacer layer not necessarily needs to be as thick as a quarter of the wavelength. Although for most metasurface designs, the bandwidth for unity absorption is also narrow, broadband absorption can be achieved by stacking several layers of metasurface resonating at close resonance frequencies [73,74,76] or using lossy material like heavily doped silicon as the spacer layer [77-80]. Figure 2.6(a) illustrates a metamaterial absorber structure consisting of three layers of cross-resonators with appropriate geometric dimensions and spacer thicknesses. The three resonance frequencies in close proximity merge together and form a broader absorption bandwidth as shown in Figure 2.6(b-d). Other metasurface-based absorbers have also been proposed and experimentally tested for more novel functionalities such as multi-band absorbers [81,82], coherent absorbers [121,122], frequency tunable absorbers [123,124].

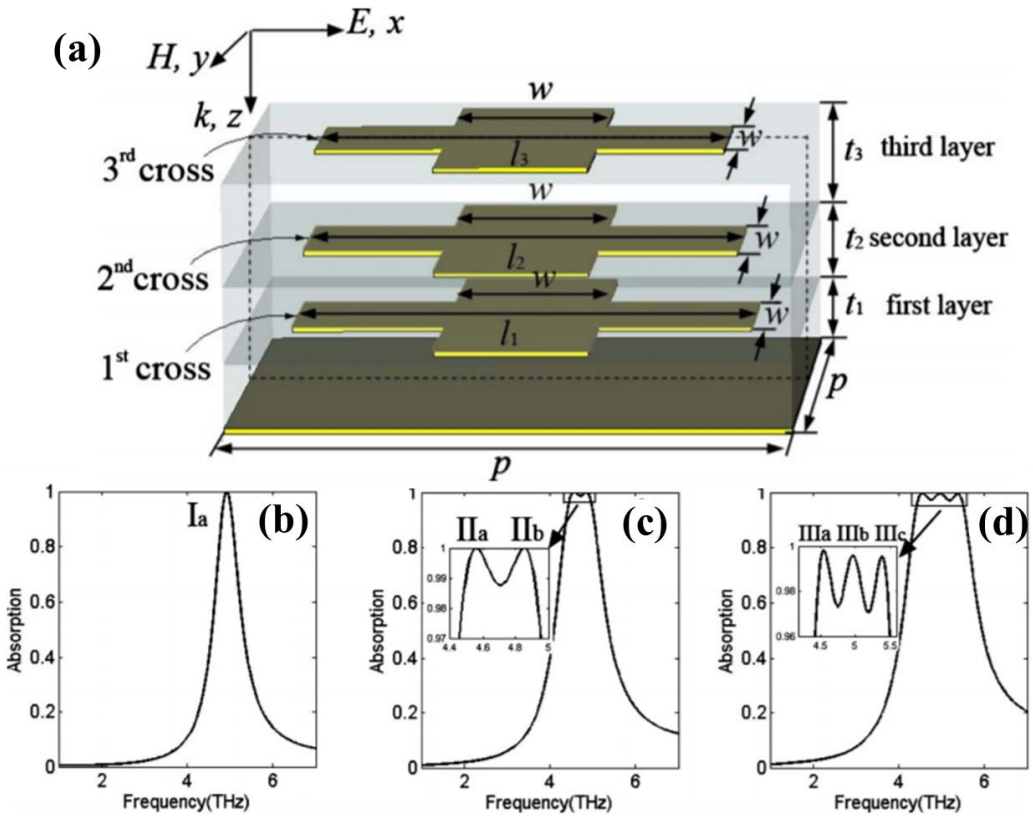

Figure 2.6 (a) Schematic diagram of a 3-layer cross-resonator absorber and absorption spectra for (b) 1-layer cross structure; (c) 2-layer cross structure; (d) 3-layer cross structure (illustrations from Ref [76]).

ii) Ultrathin flat lenses

In general, most conventional lenses are designed on the basis of geometric optics, which engineer the wavefront of the electromagnetic wave by altering its optical path length or propagation phase which can be calculated as $\phi = nkd$, where k is the wavenumber, and n, d are the refractive index and

thickness of the medium through which the wave propagates. Compared to classical lenses, which usually needs a sophisticated height profile to achieve the change in propagation phase, metasurfaces are able to change the phase directly, as shown in Figure 2.5(b), without sacrificing the device thickness. The introduced phase changes can lead to a series of intriguing phenomena: anomalous transmission and reflection [97-101], free aberration [102], etc.

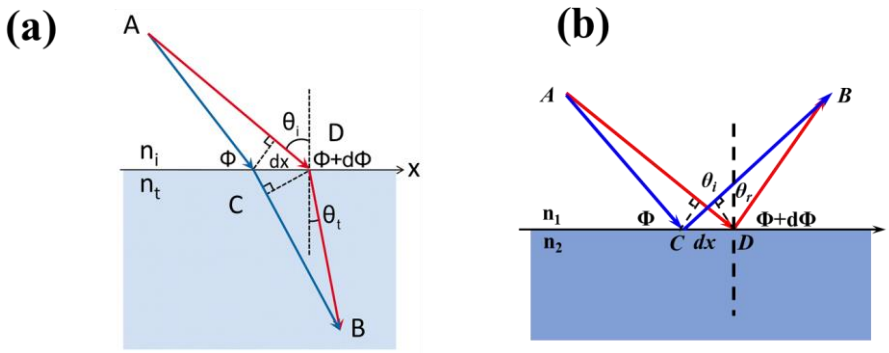

Figure 2.7 Schematics used to derive the generalized Snell's law of (a) refraction and (b) reflection.

As shown in Figure 2.7(a), consider a beam incidents at an angle θ from one medium to another medium. Assuming two optical paths ACB and ADB are infinitesimally close to the actual path between the points A and B, the difference in their propagation phases should be 0 and can be calculated as [97]:

$$k_0 n_i \sin\ \theta_i\ \ dx + \Phi + \mathrm{d}\Phi = k_0 n_t \sin\ \theta_t\ \ dx + \Phi \tag{2.9}$$

where k_0 is the wave number in air, n_1 is the refractive index of the medium where the wave coming from, dx is the distance between the two cross points C and D, Φ and $\Phi + d\Phi$ are the phases at these two points, and θ_t is the refraction angle. Similarly, for the reflection shown in Figure 2.7(b), we have:

$$k_0 n_i \sin\ \theta_i\ \ dx + \Phi + d\Phi = k_0 n_i \sin\ \theta_r\ \ dx + \Phi \tag{2.10}$$

when there is no abrupt phase change along the surface ($\mathrm{d}\Phi$ = 0), Equations (2.9) & (2.10) will lead to the classical Snell's law:

$$\begin{aligned} n_i \sin\ \theta_i\ &= n_t \sin\ \theta_t \\ \theta_i &= \theta_r \end{aligned} \tag{2.11}$$

However, if a phase discontinuity is introduced to this interface, Snell's law in Equation (2.11) will be generalized to:

$$\begin{aligned} n_t \sin\ \theta_t\ - n_i \sin\ \theta_i\ &= \frac{d\Phi}{k_0 dx} = \frac{c}{2\pi f}\frac{\mathrm{d}\Phi}{dx} \\ \sin\ \theta_r\ - \sin\ \theta_i\ &= \frac{d\Phi}{k_0 dx} = \frac{c}{2\pi f}\frac{\mathrm{d}\Phi}{dx} \end{aligned} \tag{2.12}$$

The anomalous refraction and reflection angles can thus be derived from Equation (2.12). For normal incidence in air, those two angles can be calculated as:

$$\theta_t = \sin^{-1}\left(\frac{c}{2\pi n_t f}\frac{\mathrm{d}\Phi}{dx}\right)$$
$$\theta_r = \sin^{-1}\left(\frac{c}{2\pi f}\frac{\mathrm{d}\Phi}{dx}\right) \quad (2.13)$$

the key challenge in using metasurfaces is therefore to fully control the wavefront lies in designing metasurface structures that can cover the whole 0 to 2π phase range. In some of the pioneering work on metasurfaces, V-shaped nanoantennas were proposed and experimentally demonstrated by Yu et al to control the propagation of linearly polarized light in the mid-infrared range [97,125]. The research was then extended to the optical [98], near-infrared (NIR) [100], and terahertz [101] range. However, since there is no theoretical relation between the metasurface design and the phase shift, a series of time-consuming simulations that sweep through one or more geometric parameters of the design have to be ran to test all the possible phase shift values the design can achieve. As a simpler method for designing metasurface for circularly polarized (CF) wave, Huang *et al* proposed a metasurface based on gold nanorods to manipulate the phase profile by employing Pancharatnam–Berry (PB) phase [98]. The beauty of this approach lies in the linear dependence of phase delay Φ on the orientation angle θ of each nanorod, i.e., $\Phi = \pm 2\theta$, with the sign determined by the polarity of the incident wave, which saves huge efforts in simulations. Other designs like Huygen's metasurfaces [126,127],

multilayer metasurfaces [128,129], etc are also proved to be able to cover the 2π phase range.

In order to use such phase shift resonator elements to build lenses, desired phase profile which is determined by the functionality of the lens needs to be first calculated. This phase distribution will then be discretized and converted into the corresponding resonator designs. For example, Figure 2.8(a) shows a beam steering lens based on V-shape resonators [97]. Eight different resonators are constructed into a large unit cell which has a linear phase gradient from 0 to 2π on the interface. This gradient phase profile will introduce an anomalous refraction and reflection angles, as already discussed in Equation (2.13). Figure 2.8(b) shows another example which uses circularly arrayed PB phase resonators to fit the phase distribution of an aberration-free lens [102]. Novel functionalities of metasurfaces continue to be explored benefiting from their full capabilities in controlling EM waves. One of the most promising applications is active metasurfaces, which has been realized using phase change materials [130,131], graphene [132,133], microelectromechanical systems (MEMSs) [134] and so on [135]. Programmable metasurfaces have been made and tested by sound and microwaves. Such metasurfaces can arbitrary manipulate to the wave to realize

different functions without re-fabrication which opens up the unprecedented potential for wave engineering.

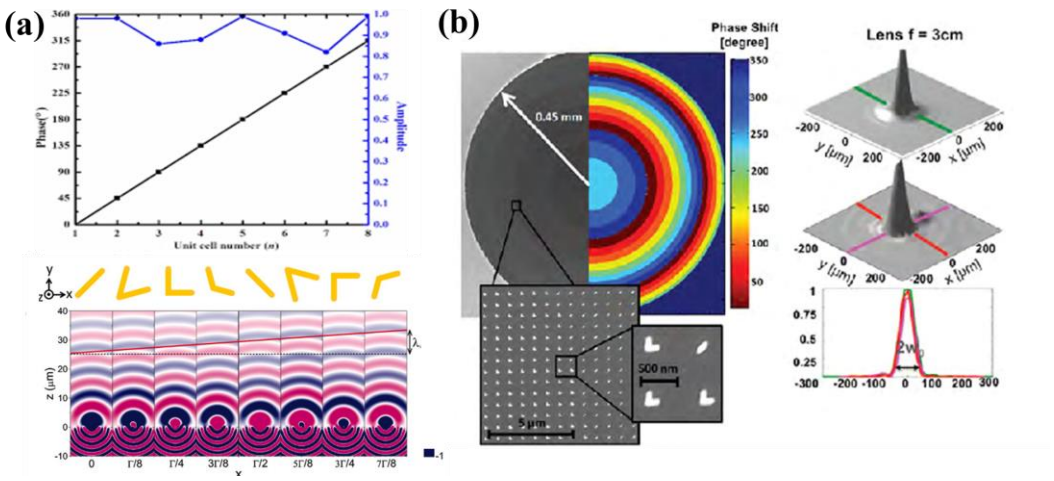

Figure 2.8 (a) top: phase and amplitude profile required for the beam steering lens, bottom: schematic of the resonator array for realizing the required phase distribution and simulations of the scattered electric field for the individual antennas composing the array (illustrations taken from [97]); (b) Flat focusing lens with consisting of V-shaped nanoantenna array and the transverse cross-section of its intensity profiles (illustrations taken from [102]).

2.3 Graphene

Apart from metasurfaces, graphene opens up another new possibility to manipulate mid-infrared light within an atomic-thick layer. This monolayer of carbon atoms arranged in a 2D honeycomb lattice has attracted interest due to its extraordinary thermal [136-138], mechanical [139,140] and electrical properties [141-143] since first being isolated in 2004. Through the studies in the past decade, both the understanding of graphene properties and the improved fabrication methods producing large scale high-quality graphene have paved the path for the development of graphene-based devices which can manipulate electromagnetic waves in the mid-infrared regime. In the following two sections, we will mainly focus on the thermal and electrical properties of the graphene in order to explore how to take advantage of these intriguing properties into the design of mid-infrared devices.

2.3.1 Electronic Properties

Due to the hexagonal structure of graphene, 3 out of 4 electrons in the outer shell of each carbon atom forms strong covalent σ bonds with neighbouring carbon atoms within the sheet, while the 4^{th} electron is located in the p_z orbital out of the plane. For monolayer graphene, these free electrons

link up together and form the π bonds which determine the exceptional electronic properties of graphene. The linear dispersion relation is the most discussed and unprecedented one among all those extraordinary properties. It can be proved, with the assistance of the tight-binding model [144] that, the dispersion relation between kinetic energy E and wavenumber k is linear for monolayer graphene and can be expressed as $E = hv_F|k|$, where h is Planck constant and v_F = 1.1×10^6 m/s is the Fermi velocity for graphene. Because the Fermi velocity is approaching the speed of light, the electrons in graphene are no longer non-relativistic particles and cannot be described by Schrödinger equation any more. Instead, they should be regarded as Dirac fermions with negligible effective mass and follow the Dirac equation [145]. This leads to a number of novel physical phenomena for monolayer graphene, such as an unconventional quantization sequence in the quantum Hall regime [146, 147], Klein tunnelling [148,149] and Veselago lensing [150].

Furthermore, based on this dispersion relation, the band structure of monolayer graphene can be calculated. As plotted in Figure 2.9, it can be clearly observed that in the band structure, there is no gap between the valence and the conduction bands as these two bands touch each other at a number of

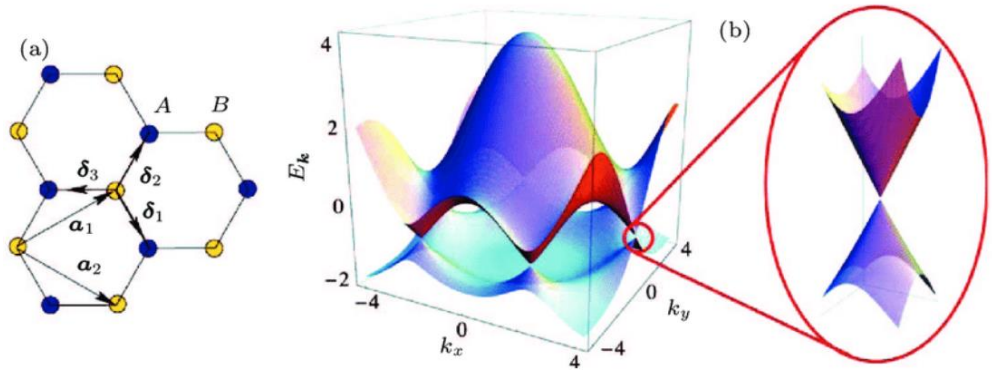

Figure 2.9 (a) Graphene lattice structure. Each original cell contains two symmetrical and inequitable carbon atoms A and B,(b) Graphene electronic band structure obtained in the tight-binding model; the valence and conduction bands connect in the Brillouin area (illustration taken from Ref [143]).

finite momentum values, termed as Dirac points. In theory, ideal monolayer graphene can be regarded as a metal with an empty valence band as the Fermi energy level lies at Dirac point. It should be noted that like other semiconductors, the position of Fermi energy level in the band structure of graphene can be controlled by either chemical doping [151], or alternatively, using the electric field effect [152,153]. For the latter method, a DC voltage, known as the gate voltage, is usually applied between graphene and a metallic layer, separated by a very thin insulator layer. In practice, most graphene devices are based on the use of doped silicon substrates with a thin oxidized layer. In this case, the

silicon is one plate of a capacitor, the SiO_2 is the dielectric, and graphene is the other plate. The surface charge density introduced into the graphene V_g can be calculated as:

$$n = \frac{\varepsilon_0 \varepsilon_r V_g}{te} \tag{2.14}$$

where ε_0 = 8.854×10^{-12} F/m is the permittivity in free space, e is the electron charge, t, ε_r are the thickness and permittivity of the thin dielectric layer. The variation in the carrier density will shift the Fermi energy level of graphene as follow:

$$E_F = \hbar v_F \sqrt{n\pi} = \hbar v_F \sqrt{\frac{\pi \varepsilon_0 \varepsilon_r V_g}{te}} \tag{2.15}$$

Figure 2.10 shows how the resistivity of perfect monolayer graphene varies with the gate voltage applied. Depending on the direction of the electric field, determined by the polarity of the gate voltage, electrons or holes can be added to the system. This ambipolar nature of graphene makes it particularly promising for applications in many photonic devices that require tunable functionality [124,154-160].

Because the conductivity can be tuned in a large range within an atomic layer, this makes graphene a promising candidate to use in conjunction with a metasurface to directly control its electromagnetic response. Modelling the

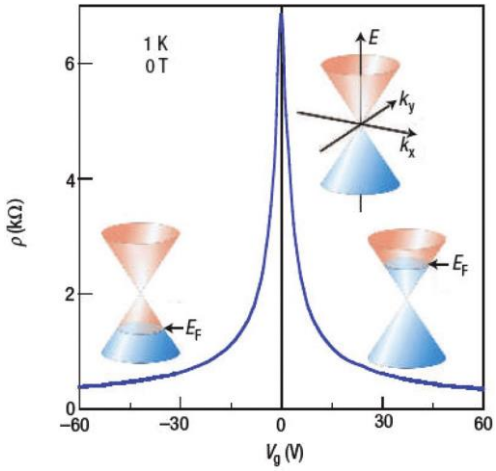

Figure 2.10 Resistivity of graphene as a function of gate voltage at 1K. The insets indicate changes in the position of the Fermi energy E_F with varying gate voltage V_g (illustration taken from Ref [161]).

conductivity of the graphene is thus of paramount importance in designing active optoelectronic devices. The conductivity of monolayer graphene can be modelled with the assistance of the Kubo formula, a quantum transport theoretical framework. Assuming the graphene sheet is in the x-y plane, its extended non-local anisotropic model for conductivity should follow the tensor form [159]:

$$\sigma = \overrightarrow{xx}\sigma_{xx} + \overrightarrow{xy}\sigma_{xy} + \overrightarrow{yx}\sigma_{yx} + \overrightarrow{yy}\sigma_{yy} \tag{2.16}$$

in which $\sigma_{xx}, \sigma_{xy}, \sigma_{yx}, \sigma_{yy}$ are the conductivity tensor along xx, xy, yx and yy directions. Noting that $\sigma_{xx} = \sigma_{yy}$ and $\sigma_{xy} = -\sigma_{yx}$, equation (2.16) can be rewritten as:

$$\sigma = I\sigma_D + J\sigma_{OD} \tag{2.17}$$

where σ_D, σ_{OD} are the conductivities along diagonal and off-diagonal directions, and $I,\ J$ are the symmetric and antisymmetric dyads. The general expressions for σ_D, σ_{OD} of monolayer graphene, derived from the Kubo formalism [162], are:

$$\begin{aligned}\sigma_{\mathrm{D}} = & \frac{e^2\ E_n^2 - \Delta^2\ \ \omega + \mathrm{i}2\Gamma}{\mathrm{i}\pi} \\ & \times \sum_{n=0}^{\infty} \left\{ \left(1 + \frac{\Delta^2}{E_n E_{n+1}}\right) \frac{[n_F\ -E_n\ - n_F\ E_{n+1}\ ] + [n_F\ -E_{n+1}\ - n_F\ E_n\ ]}{E_{n+1} + E_n\ ^2 -\ \omega + \mathrm{i}2\Gamma\ ^2} \frac{1}{E_{n+1} + E_n} \right. \\ & + \left. \left(1 - \frac{\Delta^2}{E_n E_{n+1}}\right) \frac{[n_F\ E_n\ - n_F\ E_{n+1}\ ] + [n_F\ -E_{n+1}\ - n_F\ -E_n\ ]}{E_{n+1} - E_n\ ^2 -\ \omega + \mathrm{i}2\Gamma\ ^2} \frac{1}{E_{n+1} - E_n} \right\}\end{aligned} \tag{2.18}$$

and

$$\begin{aligned}\sigma_{\mathrm{OD}} = -\frac{e^2 v_F^2 |eB_0|}{\pi} \sum_{n=0}^{\infty} \Big\{ & [n_F\ E_n\ - n_F\ E_{n+1}\ + n_F\ -E_{n+1}\ - n_F\ -E_n\ ] \\ & \times \left[\left(1 + \frac{\Delta^2}{E_n E_{n+1}}\right) \frac{1}{E_{n+1} + E_n\ ^2 -\ \omega + \mathrm{i}2\Gamma\ ^2} \right. \\ & \left. + \left(1 - \frac{\Delta^2}{E_n E_{n+1}}\right) \frac{1}{E_{n+1} + E_n\ ^2 -\ \omega + \mathrm{i}2\Gamma\ ^2} \right] \Big\}\end{aligned} \tag{2.19}$$

where $E_n = \sqrt{\Delta^2 + 2\mathrm{n}\hbar \mathrm{v}_{\mathrm{F}}^2 |eB_0|}$ is the energy of nth Landau level and $n_F\ E_n\ = \left[1 + \frac{\mathrm{e}^{(E_n - \mu_c\ E_0\ )}}{k_B T}\right]^{-1}$ is its Fermi-Dirac distribution, Δ is the excitonic

band gap, $e, k_B, \hbar$ are the charge of an electron, Boltzman constant and reduced Planck constant. v_F = 1.1×10^{6}m/s, as mentioned earlier, is the Fermi velocity of graphene, and μ_c E_0 is the chemical potential, the same as Fermi energy level, and is dependent on the external electric field E_0 for doping. B_0 is the external magnetic field applied TO the graphene, and Γ is the intrinsic scattering rate of graphene. Both diagonal and off-diagonal conductivities are very complicated and cannot be evaluated analytically. In this thesis, we assume both the magnetic bias field and the excitonic band gap are negligible. In this case, the off-diagonal conductivity term will vanish as $B_0 \to 0$, and the graphene can thus be regarded as isotropic. This will also simplify equation the to an approximation expression [159]:

$$\sigma = \sigma_{\mathrm{D}} \cong \frac{ie^2 k_B T}{\pi\hbar^2\ \omega - \mathrm{i}2\Gamma}\left[\frac{\mu_c\ E_0}{k_B T} + 2\ln\left(\mathrm{e}^{\frac{\mu_c\ E_0}{k_B T}} + 1\right)\right] + \frac{\mathrm{ie}^2}{4\pi\hbar}\ln\left(\frac{2|\mu_c\ E_0\ | - \ \omega + \mathrm{i}2\Gamma\ \hbar}{2|\mu_c\ E_0\ | + \ \omega + \mathrm{i}2\Gamma\ \hbar}\right) \tag{2.20}$$

As can be observed from Equation (2.20), the final expression of graphene conductivity model is the sum of two terms. The first term accounts for the carrier transitions within the same band, known as intraband transitions, while the second term stands for interband transitions, transitions between different bands.

Based on Equation (2.20), Figure 2.11(a) plots the surface conductivities as a function of wavelength for monolayer graphene with different Fermi levels. In the terahertz and far-infrared regions, the conductivity of graphene is determined by the intraband transitions of electrons while interband transitions are dominant in the near-infrared band. A huge increase in graphene conductivity in the mid-infrared band can be observed as intraband transitions switch to interband transitions. Figure 2.11(b) also shows graphene has a very strong plasmonic behaviour ($Im(\sigma)/Re(\sigma)$ >1) in the mid-infrared band.

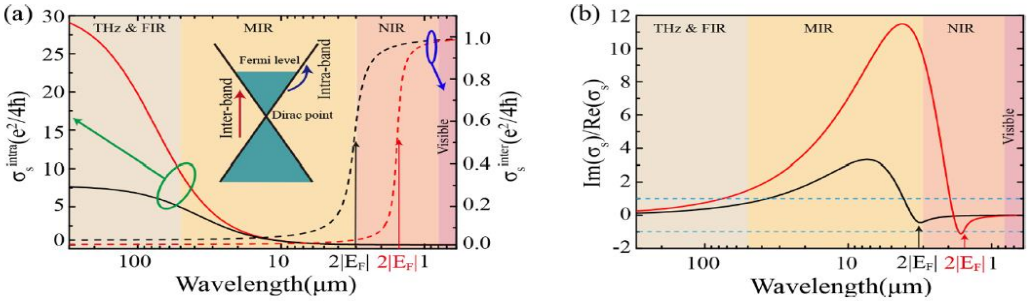

Figure 2.11(a) Real parts of intraband (solid lines) and interband (dash lines) surface conductivities of graphene with $|E_F|$ = 0.2 eV (in black) and $|E_F|$ = 0.4 eV (in red). The inset shows the band structure of graphene. (b) The optical response of moderately doped graphene in different spectral ranges (illustrations from Ref [163]).

These features, together with the high carrier mobility opens up a new era of plasmon research. Compared to the noble metal plasmon, graphene plasmon exhibits stronger energy confinement [158,164-166] and tunability [153,160]. Those two prominent properties can help to achieve the enhancement of light-matter interaction in a tiny area at a controllable frequency, which is ideal for selective sensing. Over the past 5 years, graphene nanoribbons have been intensively studied in the terahertz and mid-infrared regions to excite localized plasmon for detecting polar phonons of the substrate [160,167,168], molecular vibrations of adsorbates [151,164,166], and lattice vibrations of other atomically thin layers [169]. However, monolayer graphene can only achieve at most 2.3% absorption which limits its modulation depth. In order to reach the full potential of graphene plasmons. A metasurface can be used in conjunction with graphene to achieve a deeper modulation width [157,170].

2.3.2 Thermal Properties

Thermal conductivity is usually used to describe a material's ability to transfer heat. In solid materials, heat is generally carried by electrons or through vibrations of atoms, known as phonons. As a result, the thermal conductivity K can be calculated as $K = K_p + K_e$, where K_p and K_e are the phonon and

electron contribution, respectively. For heavily doped semiconductors or metals, electrons are the main heat carriers due to the large concentration of free charges in those materials. K_e can be thus evaluated by the conductivity of the material σ via Wiedemann-Franz Law [171]

$$K_e = \left(\frac{\pi k_B}{e}\right)^2 \frac{\sigma T}{3} \tag{2.21}$$

where e = 1.602×10^{-19} C is the charge of an electron, k_B = 1.38×10^{-23} J/K is the Boltzmann's constant and T is the temperature of the material. However for non-metallic materials, K_p is dominant in thermal conductivities. This is even applicable to some materials like graphite [160] or graphene which also have high electrical conductivity because of their strong covalent sp^2 bonding as introduced in the last section. The phonon distribution K_p can be calculation as the summation of each phonon mode [172]:

$$K_p = \frac{1}{4\pi^2 k_B T^2 d} \sum_j \int \{[\hbar\omega_{\mathrm{j}}\ q\ ]^2 N_0\ q\ [N_0\ q\ +1] v_j^2\ q\ \tau_j\ q\ \} d\mathrm{q} \tag{2.22}$$

where d is the thickness of the material, $\hbar\omega_{\mathrm{j}}\ q$ is the phonon energy of the j^{th} phonon mode at wave vector q, $\mathrm{N}_0\ q\ = [\exp\left(\frac{\hbar\omega_j\ q}{k_B T}\right) - 1]^{-1}$ is the Bose-Einstein phonon equilibrium distribution function. $v_j(q), \tau_j(q)$ are the group velocity and relaxation time of the phonon from j^{th} branch. For graphene, its hexagonal lattice leads to the formation of six phonon modes (j = 6), three optical (O) and three acoustic (A) phonon modes [136]. Like other materials,

graphene has both longitudinal (L) and transverse (T) modes for acoustic and optical phonons. L modes correspond to atomic displacement along the propagation direction while T modes stand for the in-plane movement of atoms perpendicular to the propagation direction. However, the unique 2D nature of graphene also allows out-of-plane atomic displacements, known as flexural (Z) modes, which usually cannot be observed in typical 3D materials. The phonon dispersions of all these 6 modes are shown in Figure 2.12. For TA and LA modes, it can be observed that their dispersion relations are linear when

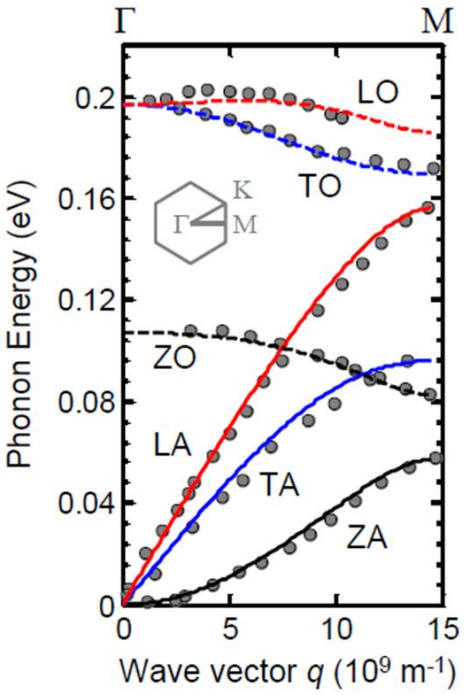

Figure 2.12 Phonon dispersion diagram of single-layer graphene along the Γ-to- M crystallographic direction (illustration taken from Ref [136]).

wavevector is low ($q \to 0$). Thus their group velocities can be calculated as the slope of the dispersion curves, $v_j(q) = \omega_j(q)/q$. The values of the group velocities of those two modes are v_{TA} = 13.6 km/s, and v_{LA} = 21.3 km/s, at least 4 times larger than those in germanium or silicon due to its three strong in-plane σ covalent bondings. Although the group velocity for ZA mode almost vanishes when q is approaching 0, Lindsey *et al* pointed out that ZA phonons are still the main contributors to the ultrahigh thermal conductivity of graphene because of their higher density of states resulted from less phonon scattering [173]. Their theory is supported by the fact that the thermal conductivity of suspended graphene is larger by an order of magnitude than that of supported graphene [174], in which graphene substrate interface scattering occurs to dissipate heat into the substrate and suppress the contribution of ZA phonons to the thermal conductivity. As a consequence, the graphene supported on a substrate can have an over 100-fold anisotropy of heat flow between the in-plane and out-of-plane directions [136].

Attributed to its excellent thermal properties and high strength, there have been increasing research interest in using graphene as an incandescent emitter for light generation. Barnard et al encapsulated graphene grown by chemical vapour deposition in h-BN films on Si/SiO_2 substrate for mid-infrared emitters [175]. These emitters were later experimentally tested by Mahlmeister

et al with a measurable modulation speed observed at 100kHz [19]. Kim et al fabricated the light source based on freely suspended, mechanically exfoliated graphene flakes [176]. One of the most fascinating phenomena of graphene emitters is the formation of the hotspot, where maximum emission occurs, and which can be manipulated by the gate voltage when a large source-drain current is applied [177]. As introduced in the electronic properties of graphene, the gate doping can introduce holes or electrons into the graphene channel. The gate voltage is equal to Dirac voltage of the graphene when the carrier density in graphene reaches a minimum (charge neutral point (CNP)) where the graphene has its maximum resistivity. Freitag *et al* found the Dirac voltage along the graphene channel becomes position dependant when a source-drain current is applied. By setting a constant gate voltage, one can manipulate the position where Dirac voltage is equal to gate voltage by change the source drain current. As consequence, a hot-spot (heat maximum) will be observed in Figure 2.13 (a) at the position where the CNP is located (hotspot). However, the hotspots are usually spatially broad and thus make their positions challenging to be fine-tuned. Bae *et al* enhance the capacitive coupling between the back gate and the charge carriers in the channel by reducing the thickness of underneath oxide layer to 90 nm, the thermal distribution, as shown in Figure 2.13(d) become more localized and sharper [178].

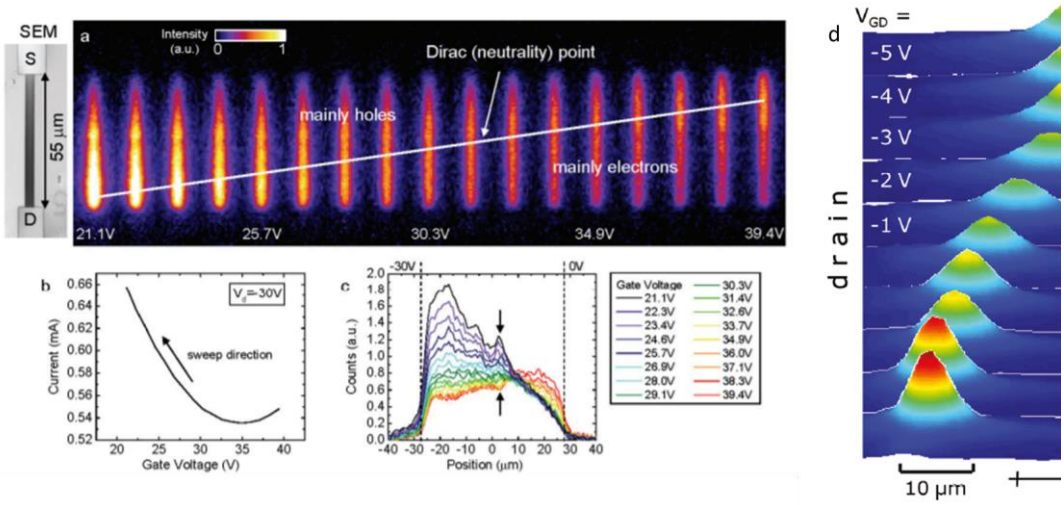

Figure 2.13 (a) Spatial images of the integrated infrared emission from graphene channels with different gate voltage, (b) Corresponding I-V characteristic, (c) Infrared intensity profile along the length of the graphene sample, (d) More localized hotspot with bias graphene on a substrate with thinner oxidized layer ((a-c) taken from Ref. [177], (d) taken from Ref. [178]).

3 Numerical Simulations

3.1 Introduction

Numerical modelling plays a critical role in the study of optoelectronic devices for identifying new structures in the development of novel or improved applications. The most obvious advantage of numerical simulations is that it assists the prediction and optimisation of the design behaviour without unnecessary fabrication iterations, saving researcher lots of time and effort. It also provides such key information as field distribution, current density and far-field projection that cannot be easily measured in experiments. In this chapter, we will mainly focus on two most popular technique for solving electromagnetic problems, the finite element method (FEM) and the finite-difference time-domain (FDTD) method, as the device studied in this thesis were all simulated by these two mathematical modelling methods. We will first briefly introduce both algorithms and then discuss how to set up the material property, mesh size, boundary conditions in two commercial software package, COMSOL Multiphysics based on FEM and Lumerical FDTD Solutions based on FDTD method. These settings are crucial for us to build a valid simulation model and obtain a reliable, accurate simulation result.

3.2 Solving Maxwell's Equations

Maxwell's equations [179] are a set of equations describing the properties and interrelations of electric and magnetic fields. The propagation of all electromagnetic radiation, from hard X-rays to ultra-low frequency radio waves, under any circumstance is governed by those four equations whose differential form can be expressed as follow:

$$\begin{aligned} \nabla \cdot \vec{E} &= \frac{\rho}{\varepsilon_0} \\ \nabla \cdot \vec{B} &= 0 \\ \nabla \times \vec{E} &= -\frac{\partial \vec{B}}{\partial t} \\ \nabla \times \vec{B} &= \mu_0 (\vec{J} + \varepsilon_0 \frac{\partial \vec{E}}{\partial t}) \end{aligned} \tag{3.1}$$

where E and $\vec{B}$ are the electric and magnetic fields, which we aim to solve, ε_0 and μ_0 are the permittivity and permeability in vacuum and ρ and J are the density of charge and current, respectively. As indicated in Equation (3.1), Maxwell's equations are a set of coupled partial differential equations (PDEs) that cannot be solved with analytical methods for the vast majority of geometries and problems. In order to predict the interaction between the proposed structure and the electromagnetic field, Maxwell's equations need to be calculated by numerical methods. In this section, two main approaches, the

FEM [180] as well as the FDTD method [181], for solving the differential equations are discussed. Although apart from these two numerical methods focusing on solving Maxwell's equations in differential form, there are other means like the method of moments (MoM) [182], the finite integration technique (FIT) [183], the finite-difference frequency-domain (FDFD) method [184] can serve the same purpose under certain circumstances. However, those techniques suffer from disadvantages [185] which makes them not as common as the FEM and the FDTD method.

3.2.1 Finite Element Method

The development of the FEM can be traced back to early 1940s when Richard Courant first proposed this method in solving torsion problems for multiply-connected domains [186]. Although he recognized such method can be applied to solve a range of problems, it took several decades before the approach became widely used in solving space-dependent problems which can usually be expressed in terms of PDEs. In the FEM, the target PDE over the desired solution domain is discretized in small regions, known as finite elements. For instance, as illustrated in Figure 3.1, in 2D applications, the domain is normally discretized into triangles while the most common shape of finite element for 3D models is tetrahedron. Such shapes of FEM elements provide

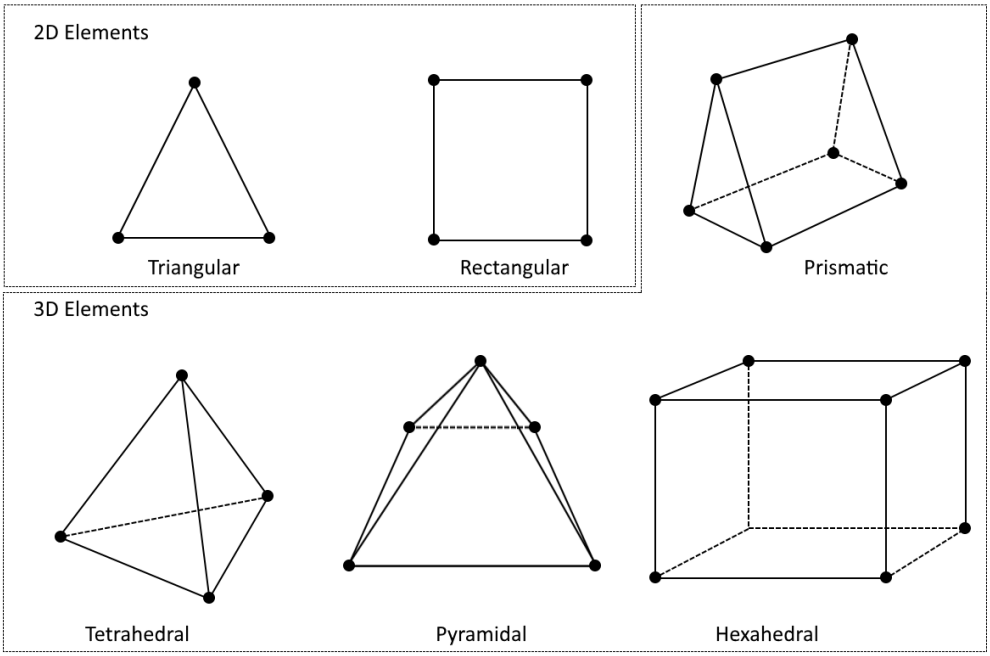

Figure 3.1 Geometry for 2D and 3D meshes (elements) in COMSOL.

advantages on modelling structures with irregular geometries and capturing local effects. The numbered vertices of each created finite element are specific points (nodes) at which the value of the dependent variables are explicitly calculated. The calculated values at these nodes are then used to approximate the values of the dependent variables at non-node points inside the finite element. The nodes of this element are exterior nodes because they lie on the element boundary. Multiple elements are then used, connected at the exterior nodes, to approximate the entire domain geometry. After that, interpolation functions are selected for elements. Usually, interpolation functions are first, second or higher-order polynomials. Then, a system of equations is formulated

by using either the Ritz variational method or the Galerkin method. With related boundary conditions of the selected domain, the target PDE can be approximated by the equation system solved using linear algebra techniques. The numerical stable approximation will also guarantee the iteration will lead to a convergent result.

3.2.2 FDTD method

The FDTD method, also known as Yee's method, named after K. S. Yee who first proposed this method in 1966 [187], is a numerical technique specifically using finite difference approximation to solve Maxwell's equations in partial differential form. As observed in Equation (3.1), Maxwell's curl equations are first-order partial differential equations related the electric and magnetic fields. All these first-order derivatives can be approximated by central difference formulas. For instance, the first-order derivative with respect to x for function $f(x)$ can be approximated by:

$$\frac{df(x)}{dx} \approx \frac{f\left(x+\frac{\Delta x}{2}\right) - f\left(x-\frac{\Delta x}{2}\right)}{\Delta x} \qquad \Delta x \to 0. \tag{3.2}$$

as illustrated in Figure 3.2(a), the value of the first-order derivation of a continuous function $f(x)$ at certain point $x = x_0$ can be evaluated by the slope of two points adjacent to $f(x_0)$. Similarly, in order to apply this central

difference method approximation to the 3D electric and magnetic fields, the electric and magnetic fields to be studied are defined and divided into discrete spatial and temporal grids, known as Yee grid, illustrated in Figure 3.2(b). The electric field is firstly solved at a given instant in time, then the magnetic field is solved at the next instant in time. This calculates each field component at a slightly different location within the grid cell. Because the FDTD method uses central difference approximation, the vector components of electric fields and magnetic fields of Yee cells are spatially staggering in the Cartesian computational domain, meaning that each electric field vector is located midway

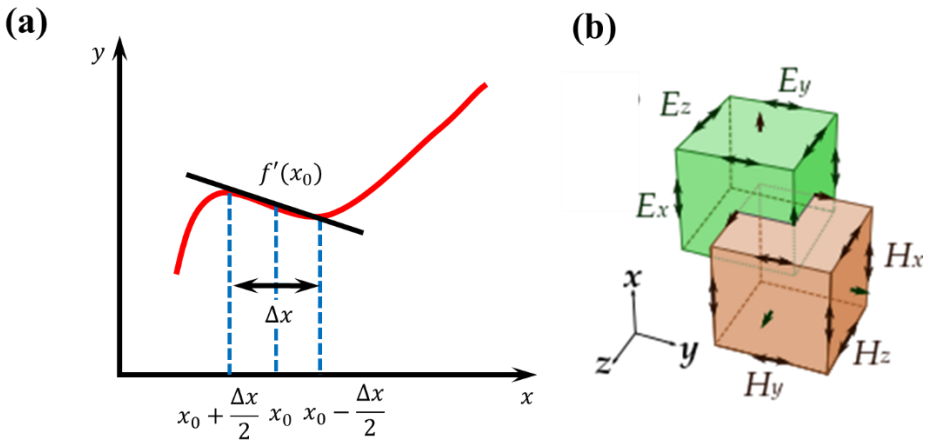

Figure 3.2 (a) A graphical representation of a central-difference approximation to the gradient at a point x_0 (b). Illustration of a standard Cartesian Yee cell used for FDTD which is composed of an electric cell and a magnetic cell staggering in space (illustration taken from [188]).

between a pair of magnetic field vectors, and vice versa. Furthermore, as H-fields are sampled at a half sampling interval difference than that of E-fields sampling, E-fields and H-fields are updated in a leapfrog scheme for marching forward in time. The process is repeated over and over until the desired transient or steady-state electromagnetic field behaviour is fully evolved.

This algorithm is capable of finding the corresponding electric and magnetic fields $\boldsymbol{E}(t)$ and $H(t)$ at any point in space for any time t with any given excitation source. Because it solves the problem in the time domain, a wide range frequency as well as a fine frequency resolution can be obtained through Fourier transform. This is extremely useful in applications where resonant frequencies are not exactly known, or anytime that a broadband result is desired.

3.3 Simulation software and settings

3.3.1 Simulation Software

Although both the FEM and the FDTD method offer proven approaches to numerically calculate the interaction between any artificial design and electromagnetic field, it still needs a vast material, financial support, manpower

and time to build a generalized 3D electromagnetic solver which contains the full 6-vector Maxwell's equations. Thanks to the progress in computer technology, various commercial software with automatic adaptive and graphical user interface (GUI) features nowadays can provide a fast, stable, accurate and multifunction EM simulator. The software packages which we chose in the simulations are COMSOL Multiphysics and Lumerical FDTD Solutions.

COMSOL Multiphysics is a general-purpose simulation software based on FEM analyses for modelling designs, devices, and processes in all fields of engineering, manufacturing, and scientific research. The module mainly used in the simulations described in this thesis is the RF module. It provides a simulation environment to solve PDEs not only for electromagnetics but also for heat transfer, structure deformation, fluid flow, and so on. The commercial software chosen for the FDTD method is Lumerical FDTD Solutions, which is a leading 2D/3D Maxwell’s equation solver for the design, analysis, and optimization of nanophotonic devices, processes and materials. It implements the FDTD method to analyze the interaction of a broad spectrum of radiation with complicated designs and deliver reliable results.

With the help of the powerful commercial software, we still need to make the right configurations on our model to obtain a trustworthy simulation result. The

following paragraphs will mainly focus on the settings on material properties, boundary conditions and mesh sizes.

3.3.2 Material Properties

The most important settings of material properties are similar in both COMSOL Multiphysics and Lumerical FDTD Solutions. As the type of materials to be defined can usually be chosen from a list. Here we will list some of the most common materials.

i) Dielectric

For most non-conductive materials, the materials can be defined as '(n,k) material' in Lumerical FDTD Solutions and 'refractive index' as the displacement field model applied on the material in COMSOL Multiphysics. In this case, the refractive index of the material will simply be modelled as $n = n_r + i\kappa$, where n_r and κ are the real and imaginary part of the refractive index. The value of κ is usually positive which corresponds to the energy loss in the wave propagation. If the refractive index of the dielectric material is dispersive over the frequency of interest, its frequency dependant n_r and κ can be extracted from the metrology of the material, like ellipsometry or spectrophotometer [189]. The result refractive index datasets can be loaded to

COMSOL Multiphysics and Lumerical FDTD Solutions and will be fitted by a generalized multi-coefficient function for simulation.

ii) Metal

For conductive materials like metal, since the current density J in Equation (4.1) can now be directly calculated by Ohm's Law $J = E/\sigma$, the permittivity of conductive materials can thus be derived as $\varepsilon(f) = 1 + i\sigma/(2\pi f\varepsilon_0)$. It is straightforward that in this relation, the loss of the metal is proportional to its conductivity. This is consistent with the fact that the metal will block the electromagnetic wave in low frequency. In COMSOL Multiphysics, the region for metal needs to be selected 'real permittivity' as the electric displacement field model, with the real part of permittivity and permeability set to 1, and a specified electrical conductivity. In Lumerical FDTD Solutions, an "3d conductive material" can be defined in the material library with ε_∞ = 1, and the conductivity of the metal.

iii) Monolayer graphene

For two dimensional materials like monolayer graphene, it is no longer precise to use volumetric parameters like permittivities or refractive indices to represent their properties due to their atomic thickness. In the case of monolayer graphene, a surface conductivity model derived from the Kubo

formula is the preferable approach used in all our simulations. In Lumerical FDTD Solutions, this can be simply realized by defining 'Graphene' as the type of material while in COMSOL Multiphysics graphene can be set as a resistive surface with the conductivity represented by Kubo formula.

3.3.3 Boundary Conditions

The boundary conditions are critical in solving Maxwell's equations, thus the boundaries set in the simulation model will dramatically affect the final result. Additionally, in some cases, the design of interest can be simplified in the simulation model by applying correct boundary conditions to save enormous simulation time. Take the simulation of a metasurface device as an example, due to its native periodic nature, this allows us to calculate the response of the entire device by using only one unit cell in the simulation. This can be done by applying Floquet/Bloch boundary conditions on all four boundaries perpendicular to the metasurface unit cell in COMSOL Multiphysics and Lumerical FDTD Solutions. The Floquet/Bloch boundary condition is a generalized type of periodic boundary condition. With a normal incident wave, the boundary condition will perform just like periodic boundary condition, simply copying the EM fields that occur at one side of the simulation and injecting them at the other side. For the case in which the wave injected on the device with an

angle, the Floquet/Bloch boundary condition will correct the phase discontinuity due to the oblique incidence in the EM fields between every two adjacent unit cells. For the remaining two boundaries parallel to the metasurface, perfectly matched layers (PMLs) are utilized to truncate the simulation region in order to absorb outgoing waves from the interior of the simulation region without reflecting them back into the interior. The type of source set for all the simulations is a plane wave. Although in fact, the source performs more like a Gaussian beam in the experiment, the Gaussian beam is equivalent to the plane wave in the case of simulating a single unit cell, as the waist beam diameter is usually thousands of times larger than the unit cell size. For

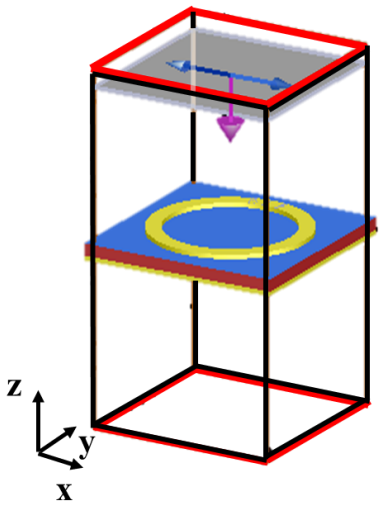

Figure 3.3 The Lumerical FDTD Solutions model of the unit cell of graphene-based metasurface modulator as introduced in Chapter 8.

example, in the case shown in Figure 3.3, the wave propagates along the z-axis. Thus all the x-z boundaries and y-z boundaries in the black rectangle are set for Floquet/Bloch boundary conditions to make the design periodic in x- and y-axis directions. Meanwhile, all the x-y boundaries in the red rectangle are set for PML boundaries to eliminate the reflection from the top and bottom of the simulation region.

3.3.4 Mesh sizes

Another critical parameter in both simulation software packages is the mesh size. As mentioned in Section 3.2, both methods are based on discretizing the model into smaller units (elements for the FEM and Yee cells for the FDTD method). Although a finer mesh may provide a more accurate result, it will also significantly increase the simulation time and memory usage in the meantime. The memory usage for a 3D model whose volume is V with a mesh step size dx at certain wavelength λ is approximately $\mathrm{V}\ \lambda/dx\ ^{3}$ and simulation time is around $\mathrm{V}\ \lambda/dx\ ^{4}$ [190]. Thus finding an appropriate mesh size to balance the result accuracy and simulation time is always a challenging work in every simulation model. Generally speaking, the mesh size should be at least smaller than half of the wavelength in the medium and the maximum size of meshes is approximately one-fifth of the wavelength in the medium. For both commercial

software packages, the automatically generated mesh sizes are classified to different levels, mesh sizes are classified by extremely coarse, coarser, coarse, normal, fine, finer, extremely fine in COMSOL Multiphysics and are divided to Level 1 (coarsest) to Level 8 (finest) in Lumerical FDTD Solutions. However, for small structures like thin films in the design, a refined mesh need to be manually defined to ensure there are at least three elements included in the smallest feature.

3.4 Comparison between FEM and FDTD method

As a summary, both FEM and FDTD method provide proven computational electromagnetic approaches in solving Maxwell's equations for different designs in 3D geometries. Although both of them are generalized numerical methods, they have their own advantages in some of the circumstances to make one more favourable than the other.

Using the FDTD method, because it is based on the Fourier transform of the simulation result in the time domain, the final spectrum is usually in very high frequency resolution, which makes it preferable for simulating a broadband response from the design. Its meshing settings are also fairly easy and the

simulation won't use so much memory compared to the FEM. However, simple meshes are also less suitable when discretizing curved edges or sharp corners. The staircase approximation error in meshing may lead to an error in the simulation results. The oblique incident will cause major difficulty in implementation of the FDTD method because the phase difference between corresponding points in different unit cells lead into time advance or delay that cannot be solved directly using the time-domain method. This delay requires knowledge of the future values of the fields at any step in the transverse plane which makes the FDTD method, the method depends mainly on the simultaneous time and space, difficult to implement the oblique source.

In contrast, the FEM can also realize simulation covering a broadband frequency range. It normally divides the frequency range into several steps, runs the simulation at each discrete frequency and combines several discrete results into a spectrum result. This makes the FEM far less efficient comparing to the FDTD method. Furthermore, the meshing in COMSOL Multiphysics sometimes can be problematic and occupy a large amount of memory in PC, especially for some structures including anisotropic geometries like ultrathin films. However, the complicated mesh also has some advantages, it represents the original structure much better than FDTD meshes as shown in Figure 3.4, and leads to a more precise result. Apart from this advantage, for COMSOL

Multiphysics, we can use Multiphysics function to take other effects like heat transfer, chemical reaction, etc into the consideration of the simulation.

The simulation results shown in Chapter 6 & 8 all used Lumerical FDTD Solutions as the simulation engine while the results in Chapter 7 used COMSOL Multiphysics because of the oblique incidence of the wave on the prism.

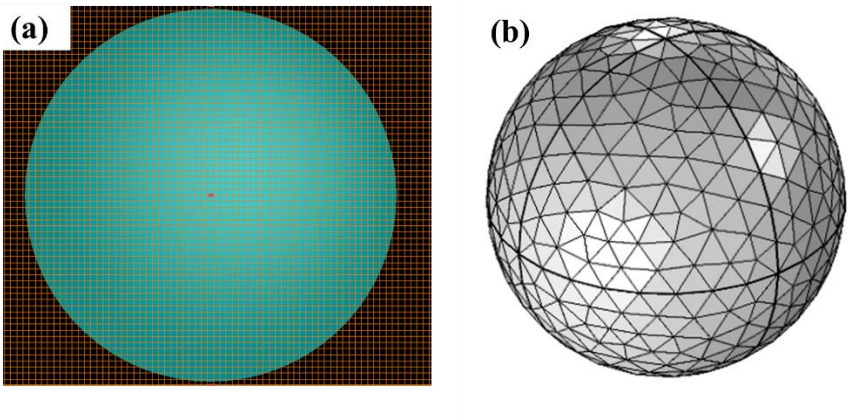

Figure 3.4 The automatically generated mesh for a sphere with 5 μm radius in (a) Lumerical FDTD Solutions (mesh setting: level 4) and (b) COMSOL Multiphysics (mesh setting: normal).

4 Device Fabrication

4.1 Introduction

Due to the fact that the scale of mid-infrared metasurface devices is usually in the order of sub-micrometers, high precision in fabrication is required to realize devices. Thanks to the significant advances in lithography technology in the past decade, which has dramatically shrunk the size of devices that can be achieved, the discoveries of nanoscience can be implemented in real-world nanoscale devices. In this chapter, we will introduce the nanofabrication techniques involved in the fabrication of our devices. The lithography, deposition and lift-off processes for metasurface fabrication and transfer, etching processes for 2D materials like graphene, and h-BN will be discussed in Section 4.2 and 4.3, respectively. Finally, in Section 4.4, a list of all the fabricated devices used in the experiments presented in this work is provided. All the devices presented in this thesis are all fabricated in an ISO Class 5 cleanroom, whose temperature and humidity are strictly controlled to ensure the precision of fabrication.

4.2 Metasurface fabrication

4.2.1 Electron beam lithography

Lithography is the process of transferring patterns from one medium to another. For many years, particle beams of various types have been used in lithography. The electron source has the benefit of extremely high diffraction-limited resolution due to its extremely low wavelength and has been used for transferring patterns with nanoscale feature sizes. Unlike conventional optical lithography, which needs a mask for each design, electron beam lithography (EBL) doesn't require a mask as the pattern could be directly loaded from computer-aided design (CAD) files. This maskless lithography system uses an electron gun to generate a collimated electron beam that has precise kinetic energy. This kinetic energy, which is controlled by the electron beam current, defines the resolution of the lithography. The beam of electrons is then introduced to a conductive surface covered with an electron sensitive resist layer at certain area depending on the pattern. As depicted in Figure 4.1, due to the exposure to the electron beam, the solubility of the resist will change, enabling selective removal of either the exposed or non-exposed regions of the resist by immersing it in a developer.

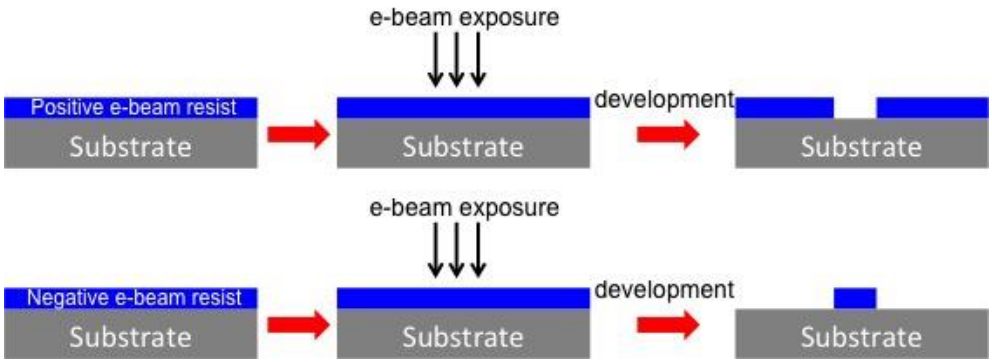

Figure 4.1 Schematic diagrams of the lithography processes on positive resist (top row) or negative resist (bottom row).

In the lithography process, there are three main important parameters for that need to be optimized for a reliable fabrication recipe: beam current, exposure dose and development time. The beam current defines the resolution of the exposure, and normally needs to be set corresponding to the smallest geometric feature in the design. Although smaller beam current can give us higher spatial resolution in fabrication, it will take much longer time in doing the lithography and thus result in low production efficiency. Exposure dose, together with the beam current determine how many electrons are emitted from the gun per unit area, which is directly relevant to the pattern quality. Development time is another crucial parameter that needs to be controlled precisely. The resist will not dissolve completely if the sample is underdeveloped, and the pattern will be distorted if overdeveloped. There are

also other parameters that could affect the quality of a lithography process, such as resist types, the thickness of the resist, developer concentration, and so on.

In our device fabrication process, the EBL system used is a Nanobeam nB4 system which is able to attain a minimum beam current as low as 1 nA, and the photoresist chosen is 6% single layer polymethyl methacrylate with 950,000 molecule weight in anisole (950K PMMA, A6), which is spun on the prebaked substrate in a spinner at 4000rpm to form a uniform 400 nm-thick positive resist layer. After exposing in the EBL, the sample is rinsed for 40 seconds in a solution of isopropyl alcohol (IPA), methyl iso-butyl ketone (MIBK) and methyl ethyl ketone (MEK) in a ratio of IPA:MIBK:MEK = 3:1:0.2. before placing in IPA to wash the developer away and blowing dry by nitrogen. Finally the sample will be inspected using optical microscopy, and is then ready for post-processing like etching or metallization. The aforementioned parameters of dosage, beam current, development time, and concentration of the developer in the recipe were optimized through dose tests and proved to downscale the pattern resolution to ~50 nm.

4.2.2 Metallization

Metallization is required to form the metallic structure based on the patterned PMMA resist after the lithography process. This normally includes two main steps, coating and lift-off. Sputtering and thermal evaporation are the two most common ways to deposit metal material on a sample. A sputter generates energetic ions to collide with a metal target to thus eject target material, while the thermal evaporator relies on heating the metallic material over the vaporization temperature. Although, in theory, sputtering can form a metallic layer with higher uniformity and purity than thermal evaporation, thermal evaporation was chosen for all the graphene devices as the high energy of the sputter atoms will inevitably cause damage to the graphene on the substrate for all the graphene-integrated devices. The thermal evaporator used in the fabrication process is an HHV Auto306 Thermal Evaporator, which is able to evaporate up to 4 different kinds of metal at one time. In the device fabrication, gold is chosen as the material for metamaterial structure as well as the contacts due to its high conductivity. However, due to the poor adhesion of the gold layer on the substrate, a thin layer of chromium is needed to be deposited as the adhesion layer before the gold layer is coated. The thickness of the Cr layer is usually about 5-10 nm, not thick enough to alter the property of the fabricated device, but helps to prevent gold from flaking off

from the substrate. The deposition process starts with mounting the sample on the holder and loading Cr pellets and Au wires in separate carrier boats. After sealing and evacuating the chamber to a pressure < $2e^{-6}$ mbar, the metals in carrier boats will be heated through a resistive heating process. This causes the evaporation of the metal, whose deposition is controlled by the amount of current applied to the boat, which then condenses on the much cooler sample and forms a metal thin film. The rate of deposition is kept constant at 0.8 Å/s for both the Cr and Au deposition, which is monitored using a quartz crystal. In all of these cases, 5 nm of Cr followed by 100 nm of Au was deposited on top of PMMA as well as directly on the substrate where the PMMA has already been developed. As shown in Figure 4.2, in order to remove the unwanted metal and PMMA, a lift-off process is required to reveal those metallic nanostructures after the deposition. In this process, the sample will be rinsed in a beaker with warm acetone at 60°C for several hours to dissolve the PMMA. In some small gaps

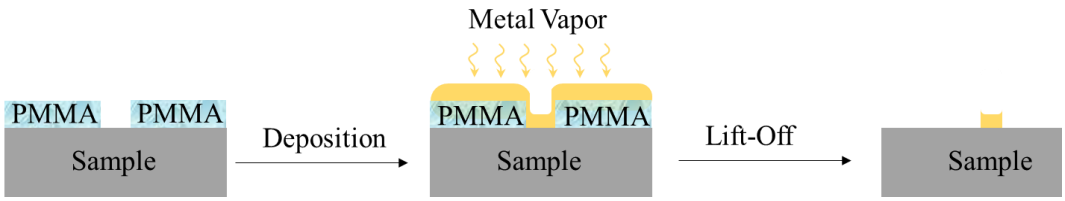

Figure 4.2 Schematic diagram of metallization process on an EBL patterned sample.

where the acetone is unable to dissolve PMMA entirely covered by metallic sidewalls, an ultrasonicator is needed to aid in the lift-off process.

4.3 2D-material fabrication

4.3.1 2D material transfer

Apart from metasurface, another group of nanoscale constituents in most of the devices discussed in this thesis is 2D materials which include graphene and hexagonal boron nitride (h-BN). Due to the recent progress in synthesizing 2D materials through chemical vapour deposition (CVD), large-area 2D materials, which can never be realized by conventional mechanical exfoliation method, are now commercially available [191]. Mono- and multi-layer CVD 2D materials like graphene and h-BN are all commercially available through multiple outlets and are widely used for research purpose. However, the CVD method usually requires a metal substrate such as Cu, Ni, Al [192,193], to form 2D materials, so 2D materials need to be transferred on an appropriate substrate before device fabrication. For all the fabrication described in this thesis, all CVD 2D materials used are grown on copper foil (from Graphene Supermarket) and Si/SiO_2 substrate is the target substrate on which the devices are fabricated. To achieve transferring 2D materials grown on Cu foil to Si/SiO_2 substrate, the

transfer methodology we adapted is the wet transfer method [194]. This method, whose illustration is shown in Figure 4.3, takes advantage of PMMA as a supporting layer. A 200 nm-thick PMMA layer is spun on top of the whole sheet of monolayer 2D material grown on Cu foil. After the spinning process, the sample is placed on a hot plate and baked at 150 °C for 8 minutes to remove the solvent in PMMA. As the CVD process results in the growth of 2D material on both top and bottom sides of the Cu foil, the 2D material on the bottom side of the Cu foil which is not coated by PMMA needs to be removed by reactive ion etching (RIE) whose details will be discussed in § 4.3.2. The PMMA coated 2D material only on the top side of Cu foil is then cut into the desired size before floating it on top of a 0.1 M solution of ammonia persulfate (APS). Due to the high transparency of PMMA, a visual inspection can be conducted directly to check if the Cu foil underlying has been sufficiently removed or not. Most

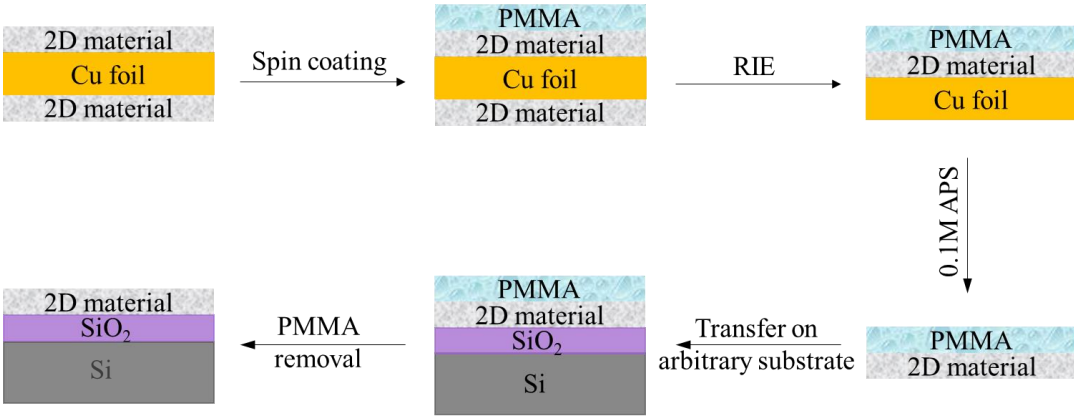

Figure 4.3 Schematic diagram of transferring of CVD 2D material grown on Cu foil to a Si/SiO_2 substrate.

importantly, because of the flexibility and dissolubility to etchant of PMMA, the 2D material with PMMA on top will remain floating on top of the solution when the Cu foil is totally etched. This is then scooped out with a glass spoon and then rinsed in DI water six times, based on a standard recipe, in order to remove any remaining etchant residue. This PMMA covered 2D material is then transferred to the Si/SiO_2 substrate and finally removed with warm acetone after the water between the Si/SiO_2 substrate and 2D material is completely dried out in the air.

4.3.2 Reactive ion etching

RIE, in conjunction with EBL, is used in order to pattern the 2D materials into desired shapes. EBL process as described in § 4.2.1 is firstly conducted on the Si/SiO_2 substrate with CVD 2D material(s) on top and will leave a layer of patterned PMMA which will act as a hard mask later in RIE. The RIE process is a high-resolution etching process based on reactive gas discharges. Specific process gases are introduced into the vacuum chamber and then ionized by radiofrequency (RF) power to form the plasma. Meanwhile, a negative DC bias is applied on the substrate plate to accelerate the positively charged ions colliding with the negatively biased sample on the plate and results into a high anisotropic, selectivity etch profile.

A JLS Designs RIE 80 Etching System is used in our fabrication process for etching 2D material, the sample is first loaded into a vacuum chamber which is then pumped down to low pressures (around 1 milli-Torr). Selected process gases, oxygen and argon, with a flow rate of 10 sccm (standard cubic centimetre per minute) and 20 sccm respectively, purge the chamber for 20 seconds. Once the concentration of process gas stabilizes, the plasma is then initiated by applying a 15 W RF field and -100 V DC to the sample. Such plasma is able to etch a single layer of 2D material or 50 nm-thick PMMA in 30 seconds. Due to the different etching rates of PMMA and 2D material, we can control the etching time and the thickness of the PMMA mask to ensure the 2D material under PMMA is kept while the rest part is removed, as illustrated in Figure 4.4. Finally, the whole sample is rinsed in a beaker of warm acetone to remove the PMMA residue on the 2D material.

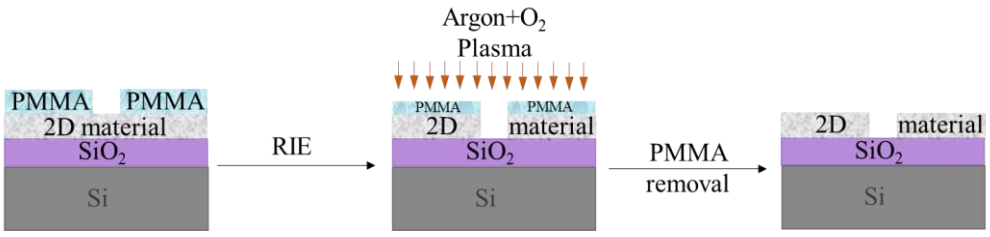

Figure 4.4 Schematic diagram of etching 2D material transferred on Si/SiO_2 substrate.

4.4 Fabricated Devices

The results presented in the experimental chapters of this thesis are from devices listed in Table 4.1 below.

Chapter No.	Project name	Device Name	Measurement setup
6	Metamaterial-based surface thermal emitter	GTE_MM_1	FTIR Reflection & FTIR Emission
		GTE_MM_2	
		GTE_MM_3	
		GTE_MM_4	
7	Enhanced attenuated total reflection detection	ATR-Si-MM01	FTIR-ATR
		ATR-SO-MM01	
		ATR-SO-MM02	
		ATR-SO-MM03	
8	Graphene metasurface modulator	GMM_01	FTIR Reflection

Table 4.1 List of fabricated devices characterized and discussed in this thesis

5 Characterisation

5.1 Introduction

This chapter mainly focuses on introducing the equipment used in testing the fabricated samples, both for morphology and spectroscopic characterization. Three common microscopy technologies for assessing nanoscale structures, optical microscope, scanning electron microscope (SEM) and atomic force microscope (AFM) are introduced and compared in Section 5.2. Section 5.3 describes a series of spectroscopic measurement setups based on a Bruker Vertex 80v FTIR spectrometer. More details on the measurement steps for acquiring the transmission, reflection or emission spectrum can be found in § 5.3.1-5.3.3. The attenuated total reflection (ATR) measurement setup is also presented in § 5.3.4. This technique is particularly useful when measuring samples in liquid form.

5.2 Metrology

5.2.1 Optical Microscopy

Optical microscopy, as the name suggests, utilizes light and optical systems to visualize objects of small sizes that are not visible to the human eye. As the oldest form of microscopy, it does not compete with modern microscopy techniques such as electron-based SEM and TEM or laser-based AFM. Nonetheless, optical microscopy requires no sample preparation and does not suffer from charging issues; it serves as a good candidate in checking sample morphology on large scales.

A Nikon LV150 upright optical microscope equipped with 5×, 10×, 20×, 50× and 100× bright field objective lenses as well as camera operated in reflective light mode was used in this study.

5.2.2 Scanning Electron Microscopy

Due to the fact that most of the smallest features in the metasurface structures designed and fabricated in this thesis are the size of several hundred nanometers, which is below the resolution limit of optical microscopes, the nanoscale structures cannot be directly observed under the optical microscope even with its maximum magnification. In order to inspect and measure the

fabricated nanostructure, an SEM is used as the alternative because of the extremely short wavelength of electron beam. SEMs are special kind of microscopes making use of the interactions between an electron beam and sample to examine conductive objects on a very fine scale. An SEM usually generates electrons in high vacuum with an electron gun fitted with a tungsten filament cathode, similar to how EBL form electron beam as introduced in § 4.2.1. Figure 5.1 shows the schematic diagram of a conventional SEM. After the electrons are emitted, they are then accelerated down and passing through a combination of lenses and apertures to produce a focused beam of electrons which hits the surface of the sample. As the electrons interact with atoms at a depth of a few microns within the sample, depending on the accelerating voltage and the working distance between the sample and the bottom lens, various types of signals are produced including secondary electrons, backscattered electrons and characteristic X-rays, etc [194]. These signals are collected by one or more detectors to form images which are then displayed on the computer screen.

The SEM used in the metrology of our fabricated samples is an FEI Nova NanoLab DualBeam FIB-SEM system. The system is able to supply the accelerating voltages up to 30 kV to achieve a high resolution of 1.1 nm and a maximum magnification factor up to 600000×. A comparison between the

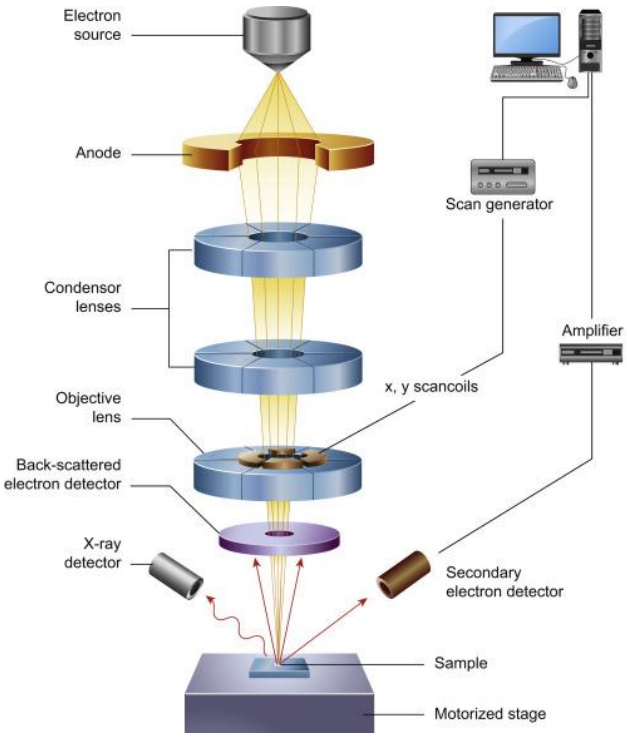

Figure 5.1 Schematic diagram of SEM working principle (illustration taken from [194]).

optical microscope and SEM is shown in Figure 5.2, in which the images of metasurface composed of split-ring resonators were taken under both conventional optical microscope with a 2000× magnification factor and under SEM. Although the image obtained from the optical microscope can still show the shape of each split ring resonator, the resolution is too low to measure the geometry parameters precisely. In contrast, the photo acquired from SEM is much clearer and enables accurate measurement of the geometry size of the structure for characterizing the fabrication errors.

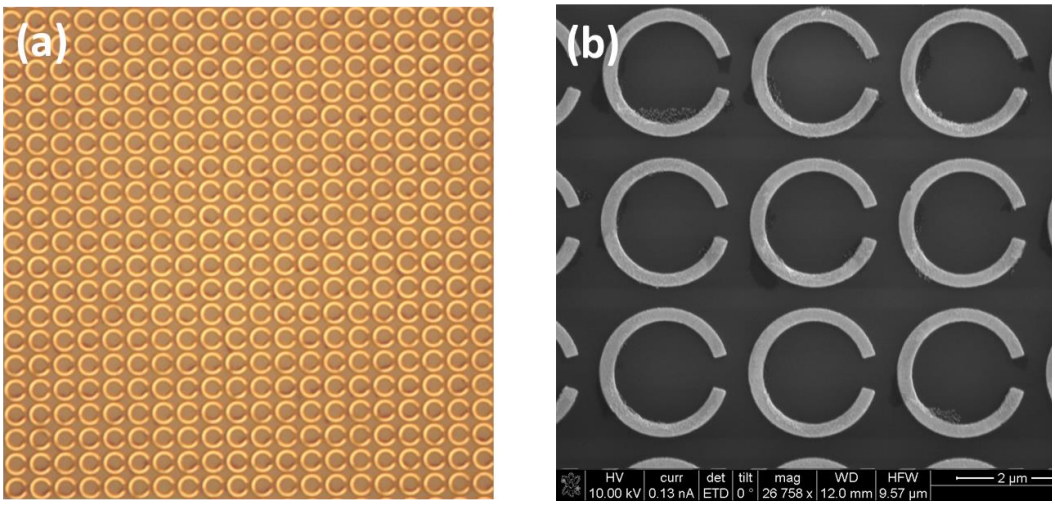

Figure 5.2 Images of a split ring resonator structure proposed in Chapter 8 measured under (a) optical microscope and (b) SEM by using a secondary electron detector.

5.2.3 Atomic Force Microscopy

Although the SEM is powerful enough to provide an informative image for characterizing nanoscale structures on the surface, the image based on the intensity of the secondary electron emission from the sample at each point during the raster scanning of the electron beam across the surface does not contain too many conclusive information in the direction perpendicular to the surface. In order to measure the height of metasurface on the structure still under SEM, the sample has to be tilted during the measurement or cross-sectioned. Both of those methods have obvious drawbacks, the former method

still unable to provide precise height information as usually the sample plate can only be tilted to a limited angle, while the latter one will inevitably to lead to irreversible damage to the sample. Complementary to SEM measurement, AFM measurement provides a non-destructive method to map the 3D topography of a sample surface with Angstrom scale resolution height information. An AFM, usually in the configuration as shown in Figure 5.3, composed of a sharp tip mounted on a cantilever, a laser source, a quadrant photodiode detector and a piezoelectric stage. With the tip raster scanning on the sample, the atomic force the sample imposes on the tip deflects the spring cantilever and thus changes the position of the laser as detected by the photodiode, which is outputted as a voltage difference and fed back to an XYZ piezoelectric motor. The piezoelectric motor will be self-adjusted by the controller to ensure that the laser is always situated in the centre of the photodiode. The voltage difference compensated by the piezoelectric motor on each stage is finally recorded and converted into images with information on all three dimensions [196]. Figure 5.4 shows the AFM image of a ring resonator metasurface designed for thermal emitter in Chapter 6 by using Gwyddion software [197].

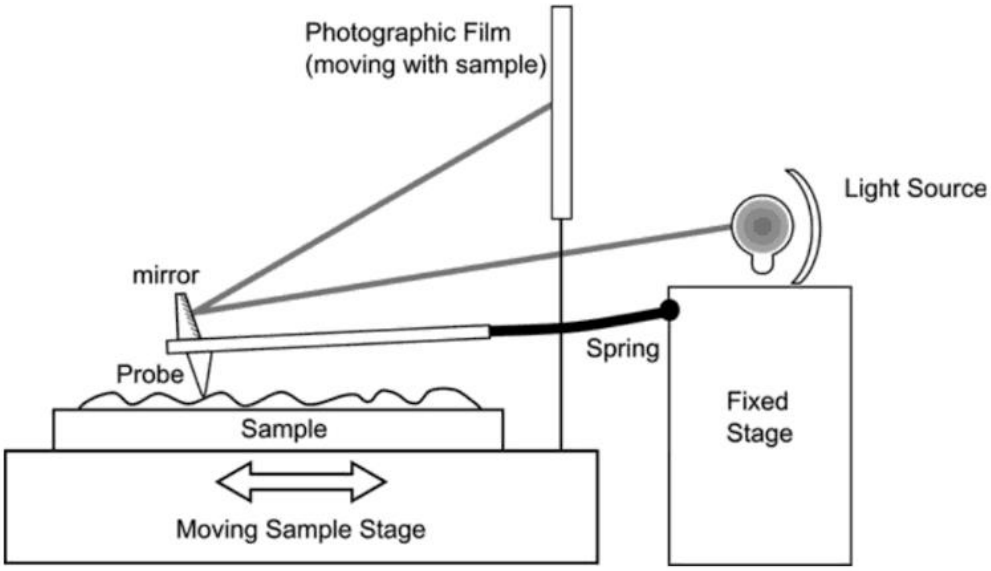

Figure 5.3 Schematic diagram of AFM working principle (illustration taken from [196]).

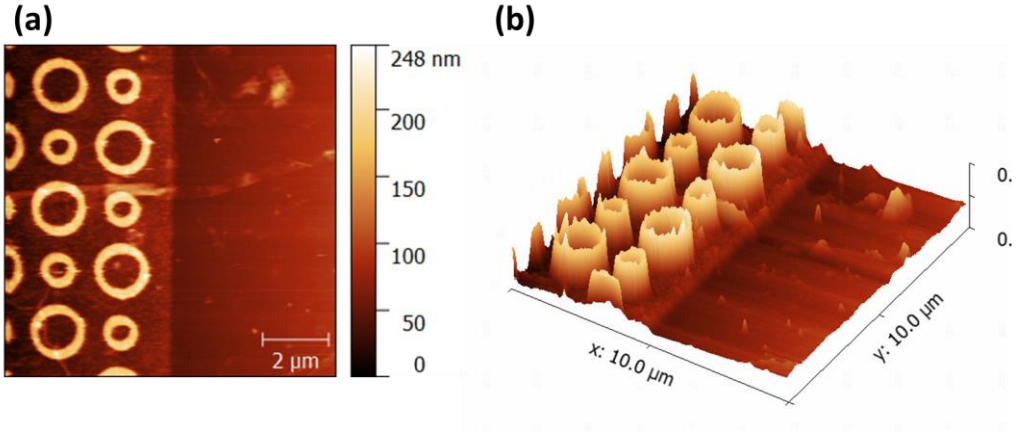

Figure 5.4 (a)2D image and (b)3D image of ring resonators on an h-BN encapsulated graphene filament.

5.3 Electromagnetic response characterization

5.3.1 Transmission Measurement

A state-of-art FTIR spectrometer from Bruker GmBH was used in most of the experiments conducted in this study to measure the electromagnetic response of the device in the mid-infrared range. The Bruker FTIR Vertex 80v, whose schematic is shown in Figure 5.5, is an ideal instrument to measure the transmission spectrum of the sample. The infrared wave emitted from the source passes through an aperture wheel which can reduce the beam size down from 8mm to 0.25mm. The beam with a desired size is then collimated by a parabolic mirror before entering into the Michelson interferometer composed of a beamsplitter, a precise linear air bearing scanner [198] and a stationary mirror. In the interferometer, the beamsplitter transmits half of the wave to the mirror on the scanner and reflects the remaining half to the stationary mirror. Since the mirror mounted on the scanner moves, it changes the optical path length in comparison to the light reflected from the stationary mirror and results in periodic interference known as interferogram when the beams recombine at the beamsplitter. The output signal from the interferometer then passes through the sample compartment and finally the transmission spectra will be obtained by Fourier transforming the interferogram data recorded at the detector located

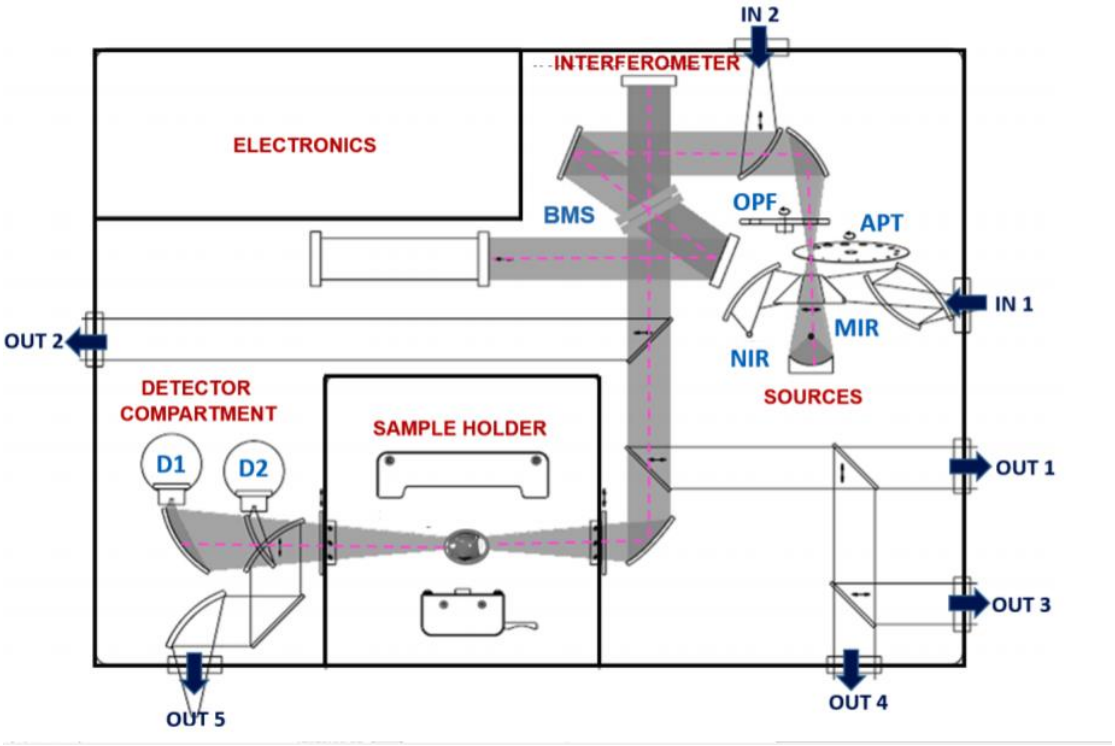

Figure 5.5 Schematic diagram and beam path of a Bruker Vertex 80v FTIR spectroscopy (illustration taken from [198]).

at the left side of the sample compartment. The FTIR comes with a wide range of sources, beamsplitters and detectors which enable the spectra to cover far-IR, mid-IR, NIR, ranges from 80cm^{-1} to 7000 cm^{-1}. Because the frequency band under our interest is mainly mid-IR, globar emitter, KBr beamsplitter, and liquid nitrogen cooled mercury-cadmium-telluride (MCT) detector are chosen in all the experiments to ensure high precision measurement between 800 to 4000 cm^{-1} with a wavenumber resolution less than 1 cm^{-1} in transmission mode. For the transmission measurement, a reference spectrum is usually firstly measured

without the presence of the sample. After that, the sample is mounted on the sample holder located at the focal point in the sample compartment for another transmission spectrum measurement. The transmittance of the sample is calculated by normalizing the spectrum from the sample to the reference spectrum. The optical bench can be evacuated rapidly down to a pressure of 3 mbar via a mechanical pump to reduce absorption due to the water vapour and carbon dioxide in the air.

5.3.2 Reflection measurement

For the measurement in reflection mode, a self-built reflection setup based on the Bruker FTIR Vertex 80v was built in order to measure the reflection spectrum of samples, including graphene thermal emitters introduced in Chapter 6 and graphene modulator presented in Chapter 8. In the reflection mode which is schematically sketched in Figure 5.6, the computer will control the internal mirrors in the FTIR to guide the beam from the interferometer to exit port 4 as illustrated in Figure 5.5 instead of the sample compartment. The size of the collimated beam is first reduced by using a pair of Au parabolic mirrors. Then the small collimated beam will pass through another beamsplitter and later be collected by a 40× reflecting objective lens mounted on a motorized XY stage, which focused the collimated beam onto the sample. The reflected wave

from the sample will be collimated again by the reflecting objective lens and then pass through the beamsplitter one more time. The refracted portion will be focused onto the MCT detector with a third Au parabolic mirror. Unlike in transmission where one can easily align the area to be measured to the infrared beam spot which is indicated by the built-in HeNe laser, it is hard to estimate where the infrared beam is incident on the sample in the reflection mode. In order to make sure the beam locates on the desired area, a raster scan is usually run on the sample before the spectrum measurement. However, due to the existence of the second beamsplitter in the setup as well as the inevitable misalignment of the system, the reflection signal coming back to the MCT

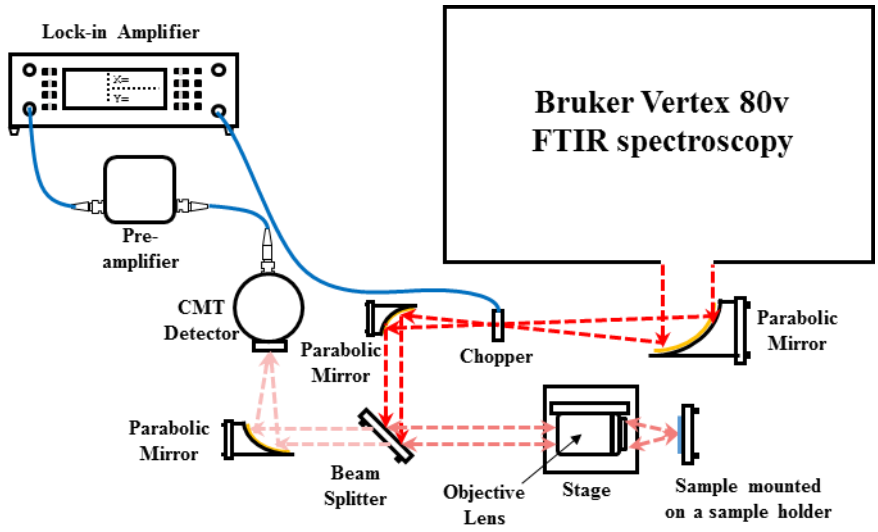

Figure 5.6 The external setup of FTIR spectroscopy for reflection measurement.

detector will be very faint compared to the signal obtained in transmission mode. A lock-in amplifier is thus used in the reflection mode in combination with an optical chopper in order to increase the signal-noise ratio of measurements. The optical chopper is placed at the focal point of the first external parabolic mirror to modulate the beam at a specified frequency, which is usually a prime number to avoid magnifying higher-order harmonic of electric hums (multiple of 50 and 60 Hz). For all the experiments conducted in this thesis, the rotation frequency of the chopper is chosen as 647 Hz. Another important function of the chopper is to provide a synchronous reference signal driving the reference channel of the lock-in amplifier whose input channel is connected to the MCT detector and its corresponding pre-amplifier. The MCT detector converts any recorded infrared signal into voltage and the lock-in amplifier rejects any discrete frequencies or noise voltages not equal to the reference frequency. In such a way, the lock-in amplifier magnifies the signal while getting rid of most of the noise. A MATLAB script was written to plot the spatially resolved reflection map by recording the lock-in amplifier readings while moving the XY stages. Judged on the surface map obtained, the stage is then moved to the coordinates of interest for reflection spectrum measurement. For the reflection spectrum measurement, the lock-in detection method is abandoned because the chopper will interrupt the measured time signal in the rapid scan mode. The

reflection spectra are measured without optical chopper and lock-in amplifier, but with averaging more scans to increase the signal-noise ratio. Like the way we calculate the transmittance, the reflectance is computed by normalizing the reflection spectra of the sample to that of a standard reflector, 100 nm Au film on Si substrate.

5.3.3 Emission measurement

An emission measurement system based on the same Bruker FTIR was also built to measure the metasurface-based graphene thermal emitter, result from which will be presented in Chapter 6. As illustrated in Figure 5.7, the

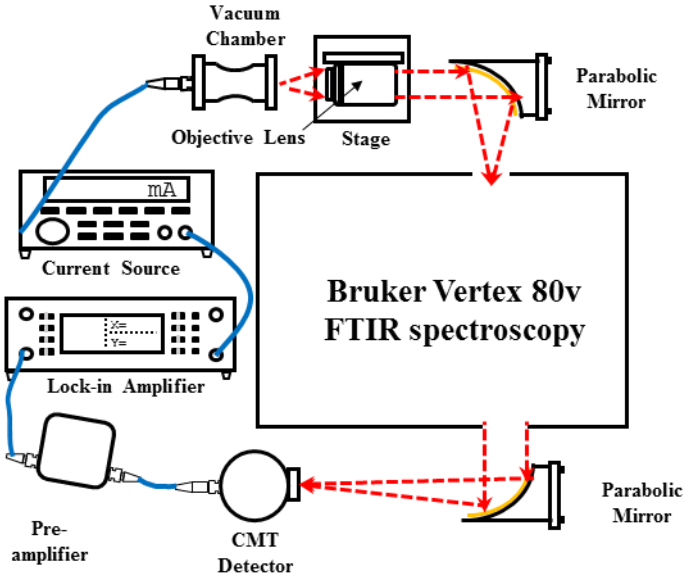

Figure 5.7 The external setup of FTIR spectroscopy for emission measurement.

thermal emitter is placed in a vacuum chamber with a polished 2 mm-thick calcium fluoride (CaF_2) window for optical access. The beam generated from the emitter will be first collected and collimated by the same 40× objective lens used in the reflection measurement. Similarly, the objective lens is also mounted on the XY motorized stage to enable the spatially resolved emission measurement to identify the location of the filament of the emitter. The beam is then guided to the input port 2 of FTIR by a parabolic mirror. After the beam going through the interferometer, it exits from output port 4 and will be finally focused on the MCT detector via another parabolic mirror. As the power supplied to the thermal emitter is only several milliWatts, the signal recorded on the MCT detector is mostly buried in noise. Similar to the configuration for reflection setup, lock-in detection method is also used in this experiment to filter out the noise and increase the sensitivity of the system to the signal. In contrast to the optical chopper used in the lock-in detection of reflection, electrical chopping is chosen as an alternative to modulate the signal at a certain frequency, thanks to the fast response time of the graphene emitter. For the emission spectrum measurement, because the signal-noise ratio remains faint even after averaging over 256 spectra in the rapid scan mode, lock-in detection in conjunction with step scan mode is applied to distinguish the signal from the noise instead. In step scan mode, the FTIR interferometer mirror moves in

discrete steps to each of the interferogram points and data is acquired at each point which means it will take minutes to perform one full scan instead of running tens of scans per second, as the rapid scanning method does. However, step scan mode is necessary because the lock-in needs time to measure and average the signal at each point (at least 3× the time constant). By moving the mirror in the interferometer step by step, this enables us to retrieve the whole spectrum of the chopped signal.

5.3.4 Attenuated total reflection Measurement

The previous three setups are ideal for solid samples because the samples all need to be mounted on a sample holder in the measurement. To measure samples in a liquid state or an aqueous environment in these systems, liquid cells are usually required to hold to the liquid analytes with a fixed and suitable optical path length. However, it is hard to achieve a quantitative conclusion based on this method because the thickness is usually not constant from measurement to measurement. This method is also not suitable for volatile chemicals that may vaporize during the measurement. Alternatively, the attenuated reflection measurement provides the possibility to measure a wide variety of liquid samples without complex sample preparation. As shown in Figure 5.8, the crucial part of the ATR measurement is the ATR crystal, which

is usually an IR transparent material with a high refractive index and a polished surface. The infrared beam is incident on the ATR crystal at an angle larger than the critical angle and is totally reflected at the crystal to sample interface. Due to its wave-like properties, the light is not reflected directly on the boundary surface but penetrates a certain distance, in the form of an evanescent wave, into the sample which is in intimate contact with the crystal. Its penetration depth, typically a few microns, depends on the wavelength, the refractive indices of ATR crystal and sample and the angle of the entering light beam. After the interaction with the sample, the IR beam exits the ATR crystal and will be finally directed to the IR detector. For the work presented in Chapter 7, a Bruker Platinum ATR unit [199] was used to characterize the chemical analytes and also the metasurface device to enhance the sensitivity of such ATR measurement. This ATR unit is designed specifically to be used in Vertex series FTIR spectrometer so that it can be locked at an exact and reproducible position when putting inside the sample compartment of the spectrometer. The crystal integrated into this ATR unit is diamond, whose refractive index is around 2.65 in the waveband of our interest. In this case, the theoretical critical angle for the wave impinges from air to the crystal is 22.6°, while in the real setup, the wave injects on the diamond crystal with an incident angle of 45°, much larger than the theoretical critical angle to guarantee the generation of total internal

reflection. The wave will only go through one total internal reflection and then exit to the MCT detector located in the detector compartment. The analytes of the ATR measurement can either be dripped on the surface if they are liquid or be pushed firmly on the crystal surface by lowering the lever if the samples are in solid form.

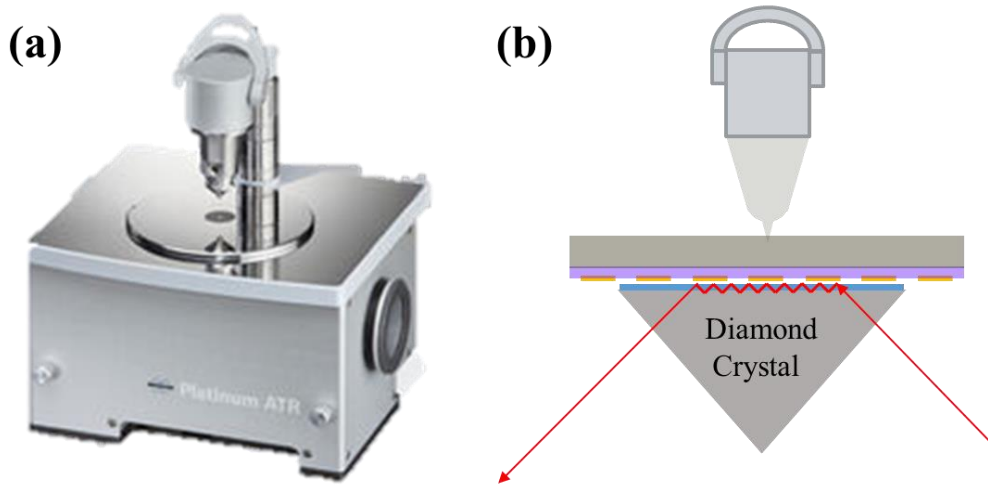

Figure 5.8 (a) Bruker Platinum ATR module (illustration taken from [199])

(b) Schematic diagram of the mechanism of ATR measurement.

5.4 Conclusion

To summarize, for the metrology, AFM is mainly used to extract the thickness information from the samples while SEM is widely used in our experiment to check the fabrication tolerance of the samples. The fabricated samples, which were found within the design tolerance, were then characterized in the FTIR. Several setups were built up to extend the capabilities of FTIR spectroscopy. With the assistance of these setups, we were able to obtain reliable transmission, reflection, emission and ATR spectrum results for the study of mid-infrared devices.

6 Metamaterial-based Graphene Thermal Emitter

6.1 Introduction

Efficient sources of light are a critical component of optical systems. Especially in the mid-infrared wave band which ranges from 3-12 μm, there is a continuing need for the development of new sources for low cost portable mid-infrared gas sensors for applications such as emission detection, and gas monitoring. There are two main streams in the research of emitting devices operating in the mid-infrared frequency band: thermal emitters [200-202], which include conventional incandescent bulbs [203], membrane filaments and photonic sources, like lasers [204] or light-emitting diodes (LEDs) [205,206]. Although conventional incandescent sources have a larger output power and are easier to fabricate, their performance is restrained by a number of drawbacks including slow response time and limited lifetimes due to the fragility of the source. In addition, they are usually enclosed in a glass bulb with inert gas, which limits the emission wavelength range due to the spectrum will be cut off by thick glass from 3.5 μm [16]. Improvements on the incandescent sources, like thin membrane emitters, can be essentially regarded as thin film versions of the conventional incandescent sources. As

the thermal mass of the filament is decreased, this complementary metal-oxide-semiconductor (CMOS) compatible design offers a slightly faster responding time compared to incandescent bulbs, leads to higher modulation frequency ranging from 20-100 Hz [201,202,207], but still not fast enough to monitor the biological events in situ and in real time. In contrast, semiconductor LEDs can respond in a much faster speed, normally in nanosecond scale, often limited by the delay in a driven circuit, which makes it a natural route for the replacement of these sources. However mid-infrared LEDs also suffers from relatively poor internal and external quantum efficiencies [208] due to the narrow bandgap required to achieve emission at the relatively long wavelengths for sensing gases such as NO_x. Furthermore, sophisticated material growth and extreme growth temperatures [209] increase not only the difficulty but also the cost of fabrication.

Graphene, two-dimensional graphite, has some unique properties as atomic thickness [210], excellent electrical conductivity [211], superior strength [139], and thermal stability [212], which qualify it as an attractive candidate for the use as an emission source. On one hand, the atomic thickness of graphene made it much thinner than any other micro-machined thin membrane. Thus it can achieve an extremely low thermal capacitance and high modulation frequency [175]. Besides, it can also achieve a higher

radiation power than those quantum emitters. All those made graphene thermal emitter to be the promising source in the mid-infrared range. The previous work of my group has shown that the encapsulated graphene emitter architecture allows sustained operation of the devices in the air, and that there is measurable modulation of the emission up to a drive frequency of 100 kHz [19], which is capable of achieving a responding time in sub-milliseconds. Although graphene thermal emitters seem to be favourable alternatives to those conventional incandescent emitters, its emission spectrum is broadband due to the thermal radiation mechanism defined by Planck's law. In reality, researchers are more interested in the emission at specific wavelength than over a broad wavelength range. For example, in order to measure the concentration of CO_2 gas precisely, we only need to detect its main fingerprint absorption peak at 4.2 μm, the signal-noise ratio (SNR) and conversion efficiency could be improved by removing any other wavelength that is out of interest.

In this chapter, we demonstrate the feasibility of patterning a layer of ultrathin metasurface design on top of a multilayer graphene filament encapsulated by multilayer hexagonal boron nitride (h-BN) in order to achieve the narrowband emission spectrum. We also show that even a relatively simple metamaterial consisting of annular ring resonators can be used in this

architecture to engineer the spectral characteristics, with an enhancement in the thermal emission at the characteristic absorption wavelength of the target molecule, and at a second wavelength that could be used for a reference channel. The integration of the metasurface into the h-BN encapsulated graphene thermal emitter to tailor the spectral characteristics, and the huge scope for optimization, demonstrates the feasibility of ultimately creating IR sources that have some of the attractive features of semiconductor LEDs, but that also could be more sustainable and cost-effective to manufacture.

As the infrared community prefers to describe the spectrum in terms of wavelength, the unit throughout this chapter will be chosen to wavelength unless otherwise specified. Wavelength will also be set as the primary axes for all plots of spectra in this chapter, while secondary axes will be chosen as frequency, which is the preference of academic scholars, for comparing to other results in this thesis or others' papers.

6.2 Design

6.2.1 Single Band Emitter

The randomly polarized wave emitted from the graphene requires the frequency selective surface (FSS) designed to tailor the broadband grey body

emission spectrum to be insensitive to the polarization state of the emitted beam. We start with closed-loop annular ring resonators, the most symmetric structure, as schematically shown in Figure 6.1. It has already been shown and proved in previous research that an induced current along the circumference of the annular ring resonator will be generated when an external electric field is applied, and thus lead to interesting spectral features that enable its applications as bandpass or band stop filters [213], or perfect absorbers [82,214]. The relation between the resonance wavelength of the metallic annular ring resonator and its geometric parameter is given by [215]:

$$\lambda = \frac{2\pi r_1 \sqrt{\varepsilon_{eff}}}{n} \tag{6.1}$$

where n is the mode number $r_1 = r + w/2$ is the effective radius of the annular ring, and ε_{eff} is the effective permittivity of the whole structure which

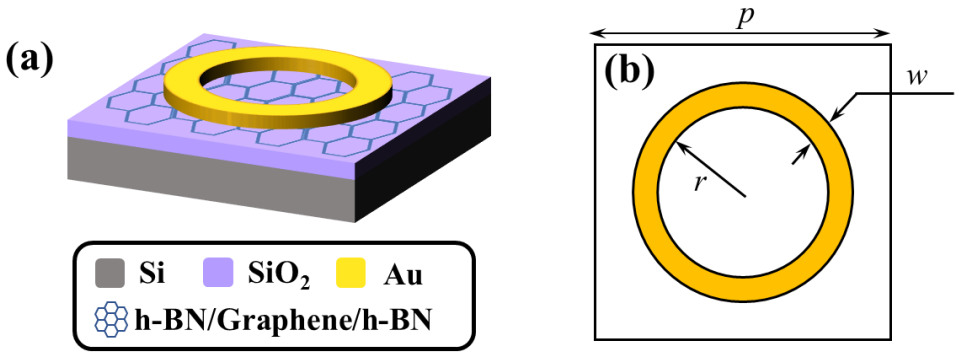

Figure 6.1 (a) 3D schematic and (b) top view of the unit cell of the design modelled in the simulation.

can be extracted from the S-parameters obtained from the simulation results [62].

Numerical simulations were then undertaken using Lumerical FDTD solutions. The gold annular ring resonators in the design are 50 nm-thick with a conductivity σ = 4.57×10^7 S/m. Due to the fact that those annular ring resonators need to be integrated into the hexagonal boron nitride (h-BN) encapsulated graphene thermal emitter, the substrate of annular ring resonators is thus selected as multilayer graphene encapsulated in 13 nm-thick h-BN film on both sides topped on a 300 nm-thick thermal oxidized SiO_2 layer followed by a 500 µm-thick highly doped Si wafer. Although previous research has demonstrated the existence of surface optical (SO) phonon modes in thermal oxidized SiO_2 layer, those SO phonon modes doesn't interfere with our design as the working wavelength of our device is designed for 3 to 7.5 µm, out of the range where phonon modes occur. This allows us to set the relative permittivity of h-BN and SiO_2 for 4.1 and 3.9, respectively [216,217], while the conductivity of the silicon is 5×10^4 S/m, given by the wafer supplier. The graphene is also modelled as a conductive sheet as introduced in § 2.3.2. In order to investigate the electromagnetic response of such a metasurface design, we start our simulation with aforementioned simulation configuration as well as electric field applied on x-axis direction and magnetic field along y-axis direction

for unit cells with following geometric parameters: periodicity p = 1.8 μm, width of annular ring resonator w = 200 nm and the inner radius of annular ring resonator r = 200 nm.

The simulation results, as plotted in Figure 6.2, demonstrate the design has a negligible transmission of the infrared wave due to the high loss of the heavily doped silicon substrate while a minimum is observed at ~ 4.5 μm in the simulated reflection spectrum. As the total absorbance of the metasurface can

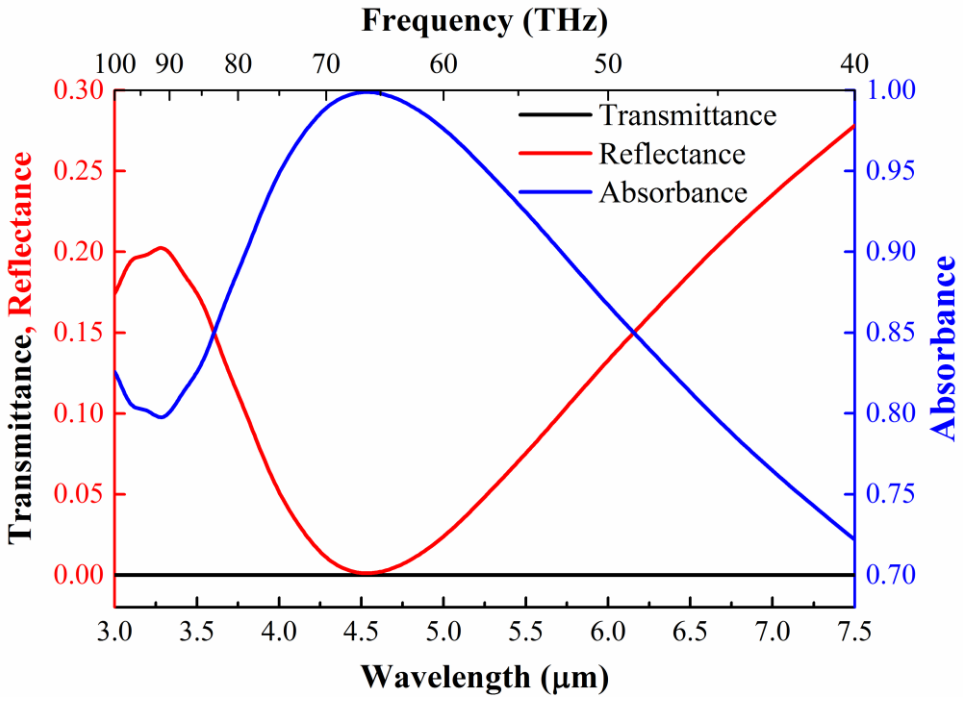

Figure 6.2 Simulated transmission (black line), reflection (red line) and absorption spectrum of the unit cell of single annular ring resonator on the top of h-BN encapsulated graphene thermal emitter.

be calculated as $A = 1 - T - R$, where T *and* R are the transmittance and reflectance, the minimum in the reflection spectrum will hence lead to a gain in the absorbance. In order to further investigate the origin of the minimum in reflection spectrum, cross-sectional electric field distribution at resonance wavelength in the x-y plane is extracted from the simulation results for analysis. Figure 6.3 clearly shows that at the resonance wavelength, the current on the metasurface (red arrows in Figure 6.3) flows in parallel from left to right at the

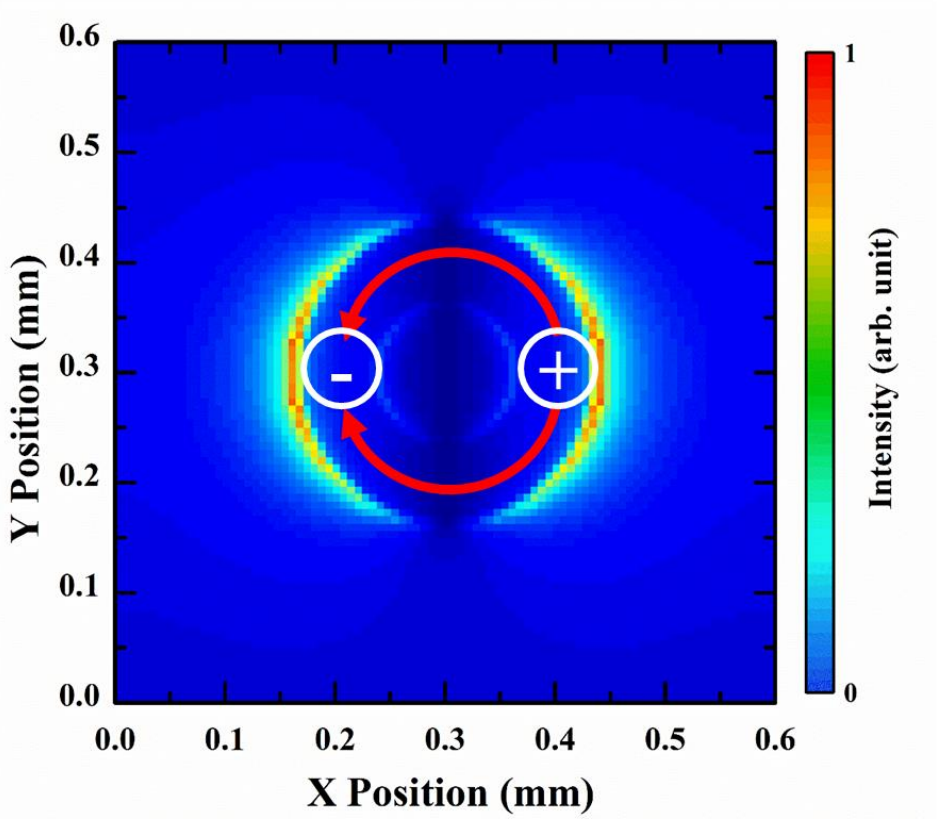

Figure 6.3 Cross sectional electric field distribution (colour plot) and surface current (red arrows) in x-y plane between metasurface and substrate at λ = 4.4 μm.

upside and the bottom side of the annular ring resonator, leading to an electric dipole mode like electric field distribution. The excitation of this electric dipole oscillation will trap the energy at resonance wavelength and achieve an increase in absorbance. As the absorbance of the device is equal to the radiation emitted from the device at thermodynamic equilibrium according to the well-known Kirchhoff's law of thermal emission [218], the mid-infrared emitter will thus have an emission peak as well at the resonance wavelength.

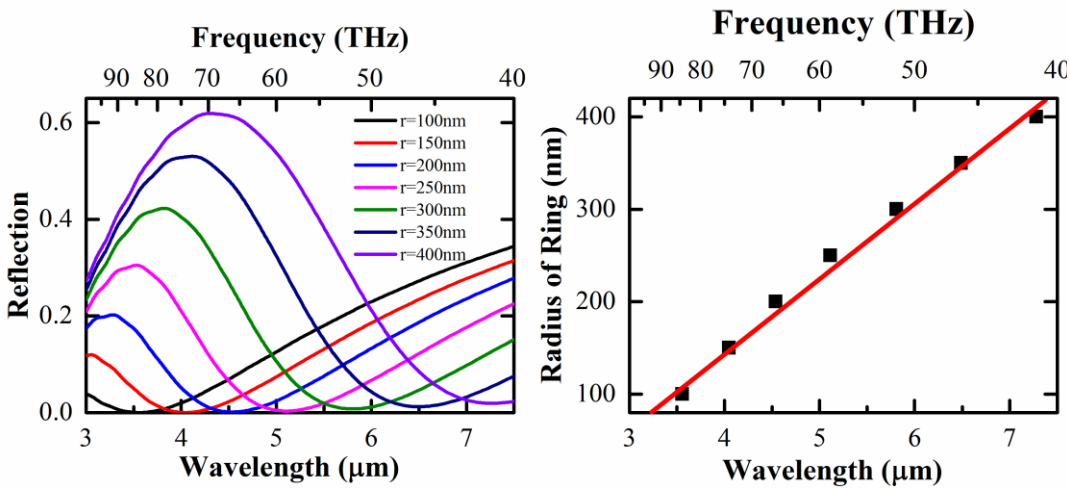

Figure 6.4 (a) Simulated absorption/emission spectra of single annular ring resonator unit cell with different radii ranges from 100 nm to 400 nm. (b) The resonance wavelength of single annular ring resonator as a function of radius of the annular ring resonator.

Another advantage of such a metasurface design is that the resonance wavelength can be directly controlled by the geometric parameters of the annular ring resonators. Figure 6.4(a) shows the simulated emissivity (absorbance) of the device with annular ring resonators of different inner radii. A clear trend of redshift of the emissivity peak is observed as the radius increases from 100 nm to 400 nm. The resonance wavelengths corresponding to the emissivity peaks were extracted and plotted as a function of the radius of annular ring resonators in Figure 6.4(b). A linear relationship is shown between the resonance wavelength and the radius of the annular ring resonator in the metasurface, which matches the early prediction in Equation (6.1)

6.2.2 Dual Band Emitter

Bearing in mind that our design is potentially aimed for mid-infrared sources applied in gas sensing, an advantageous design for such application will be a dual-band emitter instead of a single band one, with the wavelength of one emission band resonant with the absorption of the target gas, and the other emission band being centred at the wavelength of a transparent window, providing a reference. For example, if we choose CO_2 as our target gas for monitoring, we can allocate our detection window at 4.2 μm which is corresponding to the wavelength where strong absorption appears due to the

asymmetric stretching of C=O double bond while set the reference window to another wavelength far apart from the detection window or strong absorption of other gases in atmosphere, i.e. 6.6 μm [3] in our following design.

So as to obtain two emissivity peaks for detection and reference windows, two annular ring resonators with different radii are needed. According to Equation (6.1) and Figure 6.4, we calculated the corresponding inner radii of annular ring resonators should be 200 nm and 400 nm respectively. We also extend our design into a fourfold symmetric 2×2 unit cell by placing annular ring resonators with r_1 = 400 nm on the diagonal direction and the other set of annular ring resonators with r_2 = 200 nm on the off-diagonal direction while

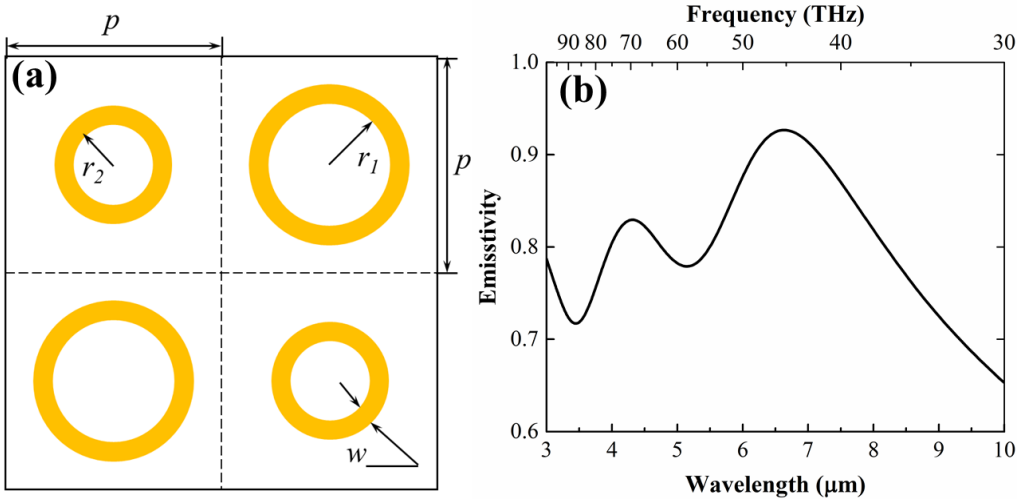

Figure 6.5 (a) Top view and (b) simulated emission spectrum of double annular ring resonator designs for dual band metasurface-based graphene thermal emitter.

remaining p = 1.8 μm and w = 200 nm. Numerical simulations, as depicted in Figure 6.5(a), confirmed that two emission peaks are achieved at desired wavelengths by the improved metasurface structure. The electric field distribution, together with the surface current density of the metasurface in Figure 6.6 also suggests that the emission peaks at 4.2 and 6.6 μm originate from the electric dipole oscillation mode from the small ring resonators in the anti-diagonal direction and large ring resonators in the diagonal direction,

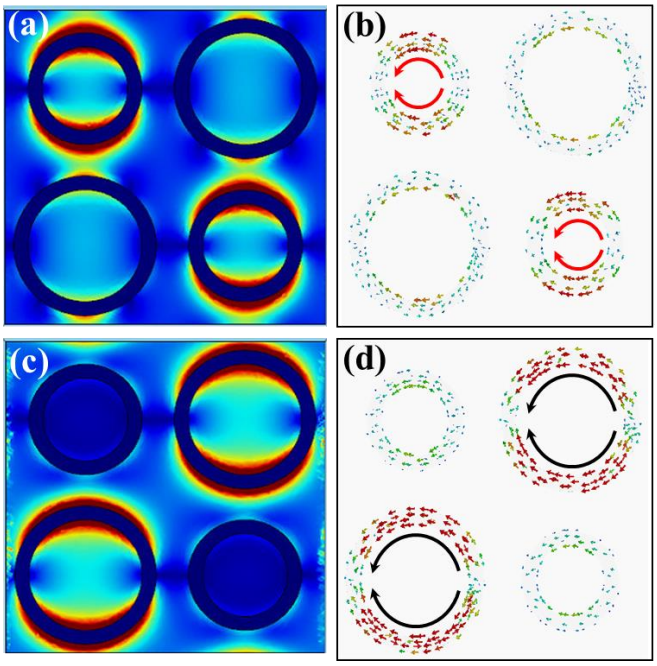

Figure 6.6 (a) Electric field and (b) surface current distributions in x-y plane between the metasurface and substrate at 4.2 μm, (c) Electric field and (d) surface current distributions in x-y plane between the metasurface and substrate at 6.6 μm

respectively. In order to verify the flexibility of the metasurface design, four graphene/h-BN encapsulated thermal emitters with metasurface of different geometric parameters were designed for fabrication and characterization as shown in Table 6.1.

Sample	r_1 (μm)	r_2 (μm)	p (μm)	w (um)	λ_1 (μm)	λ_2 (μm)
GTE_MM_1	0.35	0.1	3.4	0.2	3.3	6
GTE_MM_2	0.4	0.2	3.6	0.2	4.2	6.5
GTE_MM_3	0.45	0.3	3.8	0.2	5.5	7.5
GTE_MM_4	0.5	0.35	4.0	0.2	6.3	8.3

Table 6.1 A list of double annular ring resonators based emitters with different geometric parameters for fabrication and measurement. λ_1 and λ_2 are the theoretical resonance wavelengths related to the large annular ring resonators and small annular ring resonators.

6.3 Fabrication

The fabrication process of graphene/h-BN encapsulated thermal emitters with metasurface, as sketched in details in Figure 6.7, starts with a 525 μm-thick silicon substrate with 300 nm silicon dioxide layer. The multilayer chemical

vapour deposition (CVD) h-BN film on Cu foil and multilayer CVD Graphene film on Ni are all commercially obtained from Graphene Supermarket. The wet transfer method is applied to transfer the h-BN and graphene on the surface of the substrate. After that, an area of 500 µm×500 µm emission area was patterned by electron beam lithography (EBL) and the surrounding area was etched in reactive ion etching (RIE) machine. A 50 nm-thick Au followed by 7/70 nm-thick Cr/Au contacts were then deposited on the outer edge of the emission area for improved contact resistance. Another h-BN layer was then wet transferred and etched again on the top of the sample which ensures the total encapsulation of

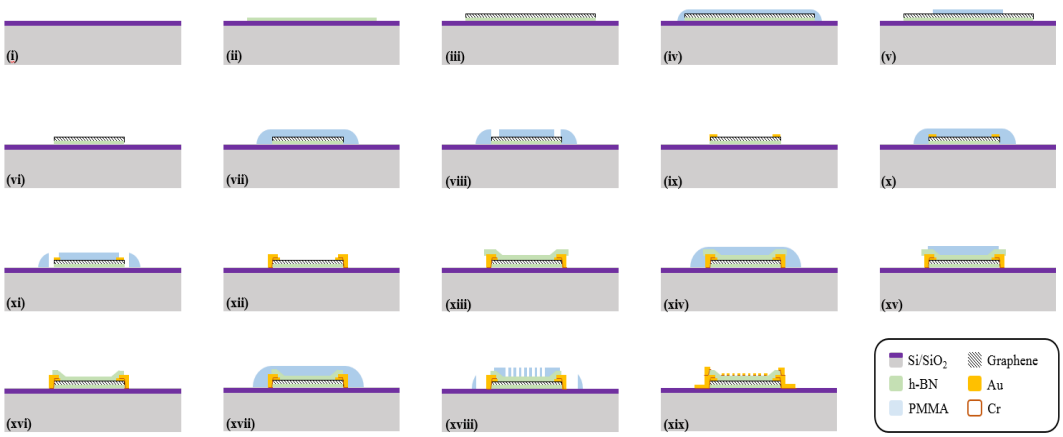

Figure 6.7 *The cross section diagrams of fabricating the sample (i)-(vi): Formation of the emission area. (vii)-(xii): Deposition of first and second contact on outer edge. (xiii)-(xv) Transfer of top layer h-BN. (xvi)-(xix) Evaporation of contact pads and metamaterial ring resonators.*

the graphene film. 5/50 nm-thick Cr/Au bonding pads and metasurface structure were finally patterned and deposited on the sample. In order to gain a direct comparison between the performance of an emitter with and without metamaterial structure, devices in which the emitting area was divided into four

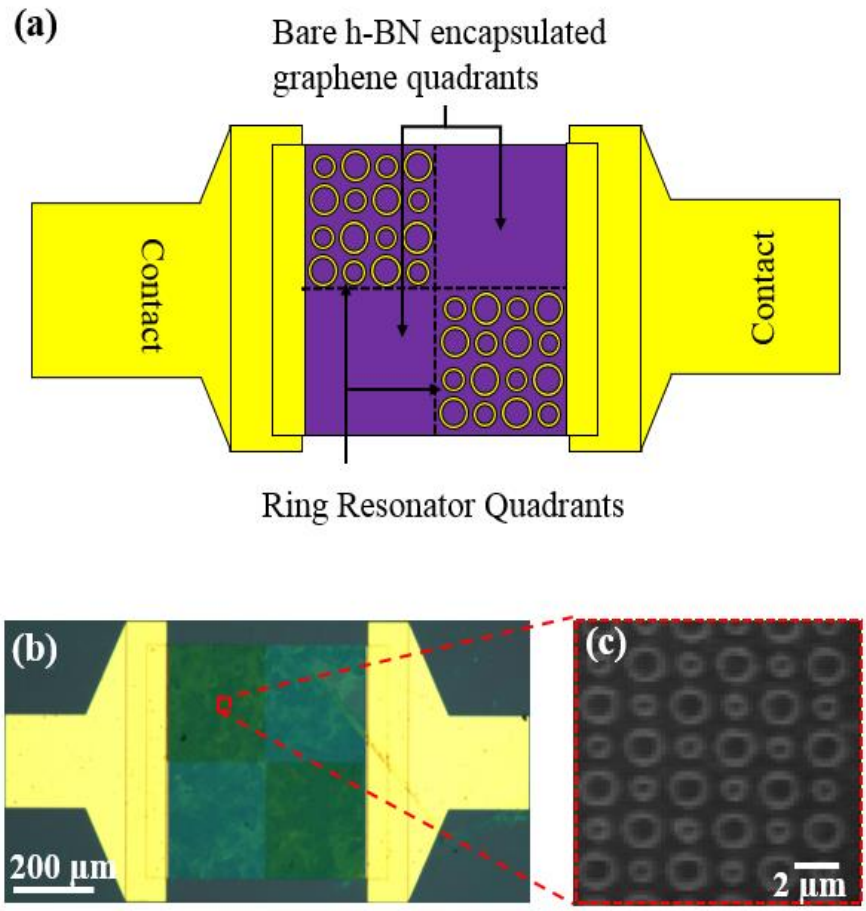

Figure 6.8 (a) Top view of the schematic illustration of graphene narrowband thermal emitter with quadrants. (b) Microscope image taken at 50× magnification of the top of the emitter. (c) AFM image taken from within the red dash box shown in (b).

250 µm × 250 µm quadrants were fabricated, as shown in Figure 6.8. The two quadrants in the diagonal direction were patterned with metasurface while the two quadrants in the anti-diagonal direction had no metasurface structure as a reference.

6.4 Reflection Measurement

As all those four fabricated devices are designed on the basis of the same principle, their reflection spectra are all expected to have two dips except the discrepancies in the resonance wavelength where dips are observed due to different annular ring resonator radii. Thus results from GTE_MM_2, the device with the same geometric parameters used in the previous simulation will be mainly discussed here. The devices were first mounted on a chip holder and their reflectivity was characterized using a Fourier transform infrared (FTIR) Spectroscopy with reflection configuration as introduced in full details in § 5.3.2. As identifying the position of the beam spot in a reflection configuration is not as trivial as in transmission configuration, scanning of the entire reflection intensity from the surface of devices were first undertaken to identify each quadrant on the surface. The measured spatial variation of reflection from GTE_MM_2 on a logarithmic scale is presented in Figure 6.9, where the areas with the largest overall measured intensity, the red regions at the right and left sides of the images, are the gold contacts. In the middle of the images, two distinct regions are clearly visible pertaining to two groups of quadrants. The two green quadrants on the anti-diagonal direction are the quadrants with double annular ring resonators on top of the encapsulated graphene filament,

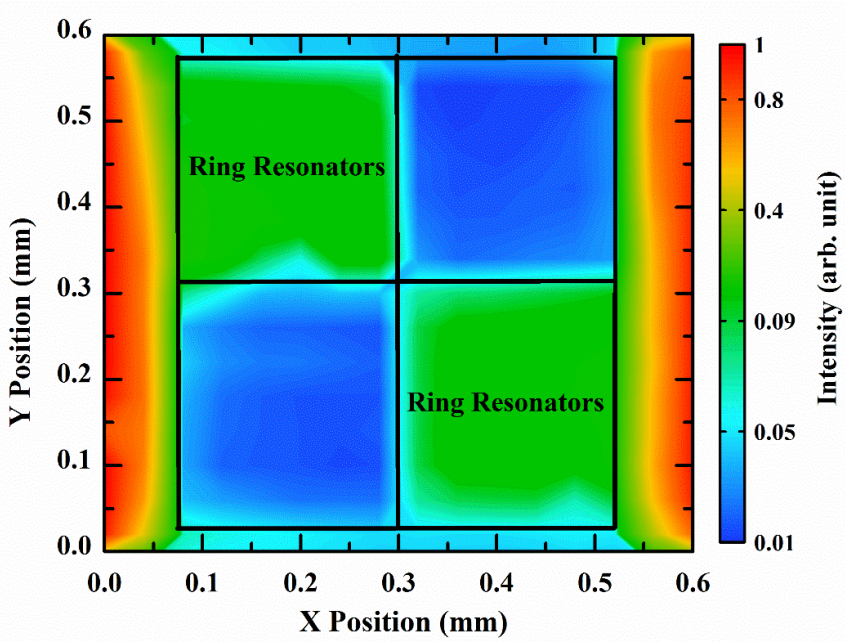

Figure 6.9 Measured spatial variation of the total reflection intensity from the surface of GTE_MM_2 on a logarithmic scale.

whilst the two blue quadrants on the diagonal direction, with lower measured intensity compared to the green quadrants, are the two quadrants of encapsulated graphene filament without metasurface on top. Quadrants with metasurface have a higher overall reflection intensity than those without metasurface as expected due to the higher reflectivity of metallic annular ring resonators in its non-resonance wavelength compared to bare h-BN encapsulated multilayer graphene without metasurface. Spectral measurements were then performed from the centre of quadrants with and without metasurface under atmospheric conditions. The reflection spectra from

both quadrants on all four samples, as well as the reference reflection spectrum obtained from a flat gold mirror, are plotted in Figure 6.10. Although the results from quadrants without metasurface on every sample all show little dependence on wavelength, the reflection spectra from quadrants with different metasurface appear more dispersive and vary across all devices. However, it is hard to draw any quantitative conclusions at this point due to atmospheric absorption and the overall spectral response of the measurement system. To correct for this, the reflectance of quadrants with and without metasurface are calculated by normalizing the spectra measured from the quadrants to that from the gold mirror. Figure 6.11 plots the reflectance as a function of wavelength for all device from different quadrants as well as the simulated reflectance of quadrants with metasurface for comparison. As expected, the reflectance from quadrants without metasurface are consistently non-dispersive through the wavelength range except the peak at 4.2 μm corresponding to CO_2 absorption,

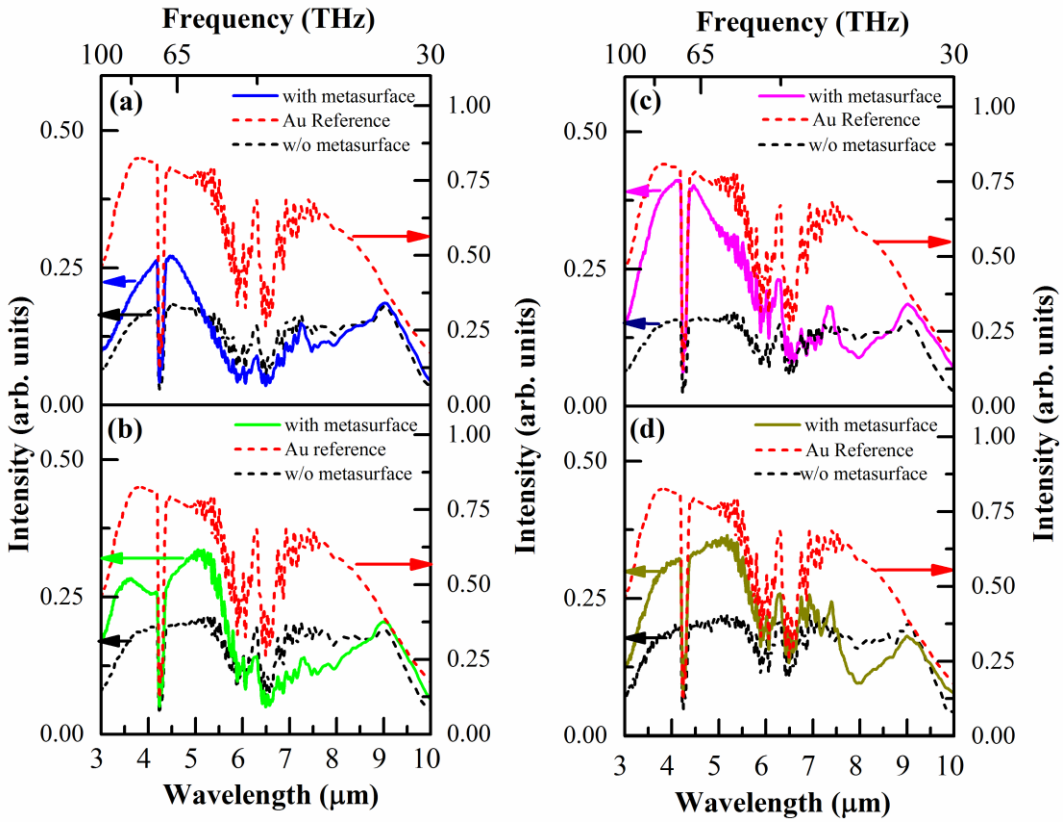

Figure 6.10 Measured reflection spectra of gold mirror reference (red dash lines), quadrants without metasurface (black dash lines) and quadrants with metasurface (solid lines in different colors) from (a) GTE_MM_1; (b) GTE_MM_2; (c) GTE_MM_3; (d) GTE_MM_4.

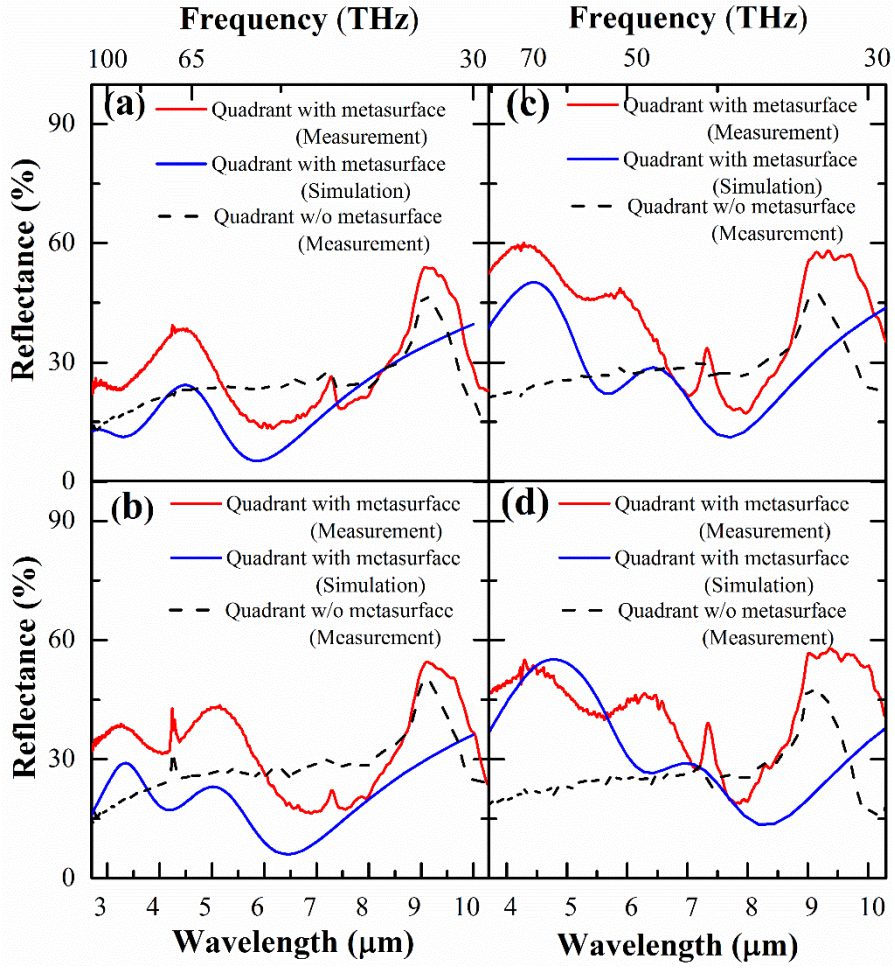

Figure 6.11 Normalized (red solid lines) and simulated (blue solid lines) reflectance of the quadrants with metasurface and normalized reflectance (black dash lines) of quadrants without metasurface from (a) GTE_MM_1, (b) GTE_MM_2, (c) GTE_MM_3, (d) GTE_MM_4.

7 and 9 μm due to the phonon mode of the underlying h-BN film and SiO_2 layer, respectively [160,219]. However, the reflectance spectra from quadrants with metasurface show a strong wavelength dependence. A two main reflection minima feature, 'W' shaped spectral response, can be observed in all four

spectra, in good agreement with simulated results. The two resonance wavelengths, where the reflectance minima occur, also change across all devices because of their different radii of the annular ring resonators and periodicities.

6.5 Emission Measurement

The emission characteristics of the same device were also measured via the emission setup of FTIR, the device mounted in a chip carrier was fixed on a ceramic chip holder and placed in a vacuum chamber. The chamber was evacuated to approximately 10^{-5}mbars by a turbo pump. A low DC bias current generated by Keithley 2400 source meter was applied on the contacts of the device to heat up the graphene filament. In order to avoid thermal shock on the graphene filament, the applied current is gradually increased to a peak injection current 50mA, where the radiant power from the device is strong enough for measurement. A similar routine of measurements, surface scanning to locate the position of each quadrant followed by emission spectra at the centre of each quadrant was carried out for all four devices, Figure 6.12 shows the spatial variation of the emission from GTE_MM_2 on a logarithmic scale. There is a noticeable difference between the emission from the quadrants with and without

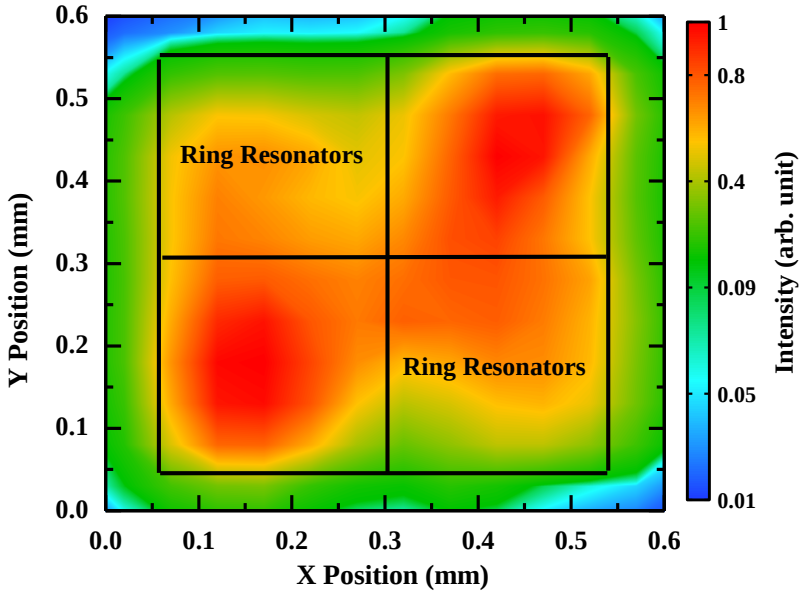

Figure 6.12 Measured spatial variation of the total emission intensity from the surface of GTE_MM_2 on a logarithmic scale.

resonators, with a higher emission intensity from the quadrants without resonators, consistent with the lower reflection intensity obtained from the same quadrants in Figure 6.9. Measured emission spectra under atmospheric conditions, plotted in Figure 6.13, from both quadrants with and without resonators are broadly that of a grey body with same CO_2 absorption at 4.2 µm and h-BN and SiO_2 phonon modes at 7 and 9 µm as observed in the reflection measurements. However, when the emission spectrum from the quadrants with metasurface is normalized to that from quadrants without metasurface, a strong wavelength-dependent response is observed. The normalized emissivity

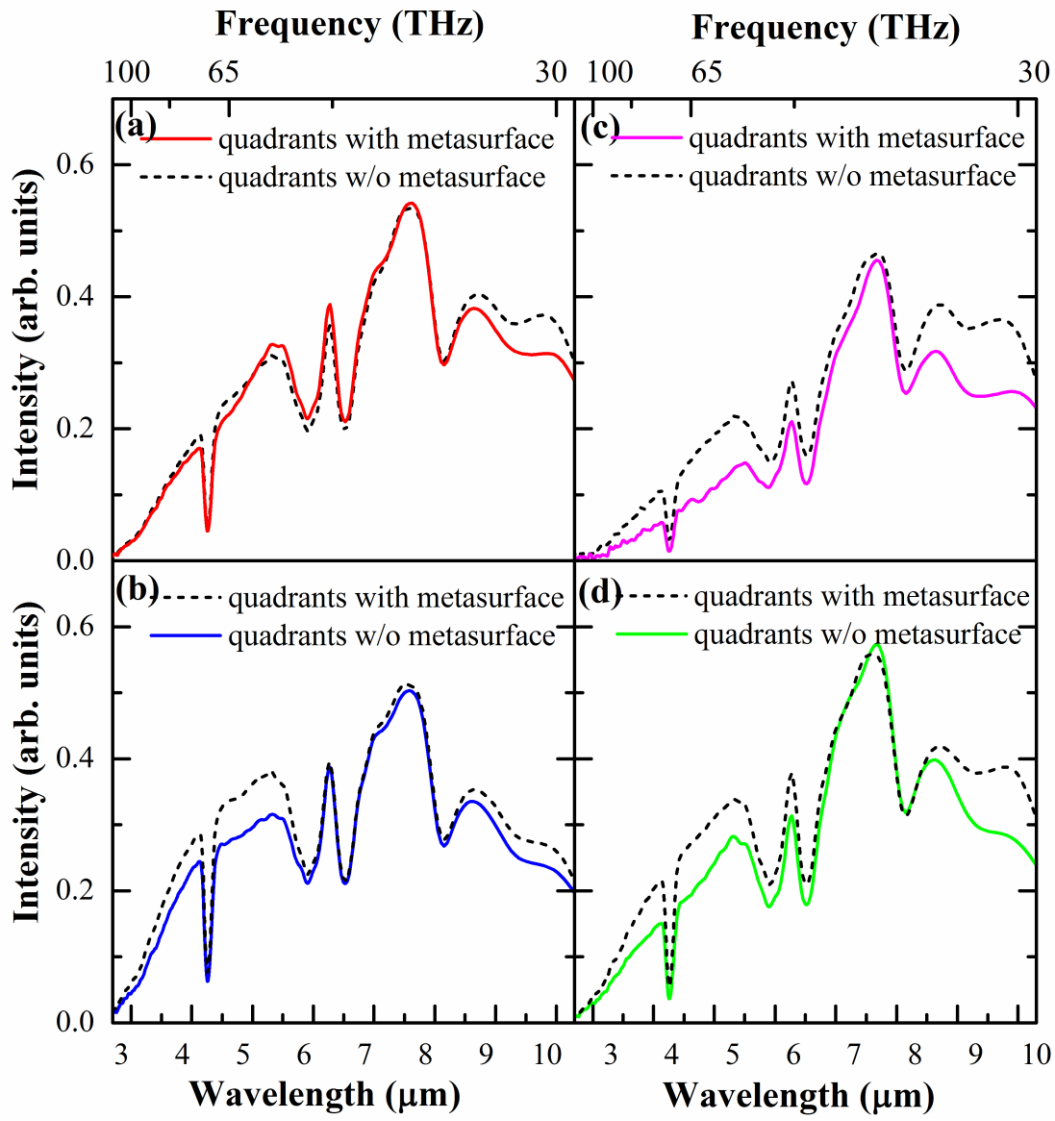

Figure 6.13 Measured emission spectra of quadrants without metasurface (black dash lines) and quadrants with metasurface (solid lines in different colors) from (a) GTE_MM_1; (b) GTE_MM_2; (c) GTE_MM_3; (d) GTE_MM_4.

obtained, after Savitzky-Golay smoothing, as plotted in Figure 6.14. An 'M' shaped spectral response is observed which, as predicted, is an opposite trend with respect to that of the reflectance of the devices. Overall there is a good qualitative agreement between the simulations and the experiments as both reflectance and emissivity data sets exhibit the increment in resonance wavelengths with increasing r_1, r_2 and p. Additionally, the quantitative agreement between the emission and reflection measurements is also good in

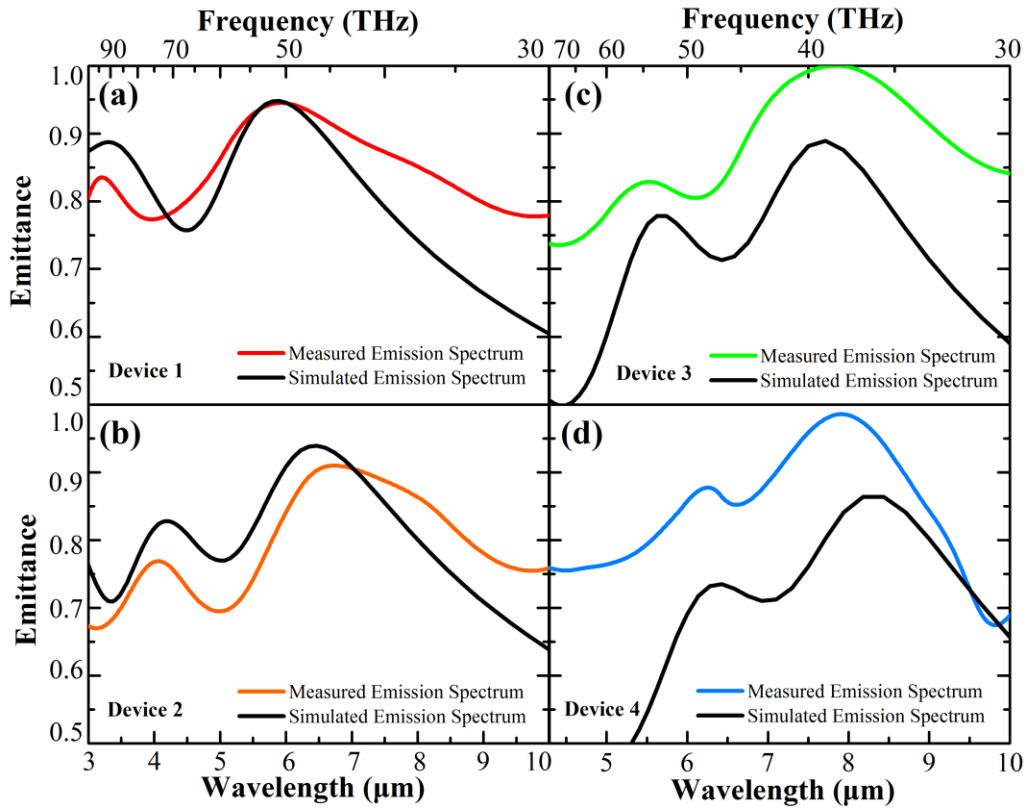

Figure 6.14 Normalized (solid lines with different colors) and simulated (black solid lines) emissivity of the quadrants with metasurface from (a) GTE_MM_1, (b) GTE_MM_2, (c) GTE_MM_3, (d) GTE_MM_4.

terms of the resonance wavelength. These results clearly demonstrate the metasurface enhance the thermal emission from the graphene-based filament, leading to maxima in the emission at wavelengths determined by their geometry. This ability to tune the broadband graphene emission spectra through the careful design of the metasurface unit cell, highlighting the potential of this device architecture to be used to engineer devices with specific characteristics, for example for sensing of different gases.

6.6 Quality Factor Improvement

Although the metasurface-integrated graphene thermal emitter on a Si/SiO_2 substrate demonstrate its capability of tailoring the broadband graybody emission into a dispersive emission, the quality factor (Q-factor) of both emission peaks are still low due to the lossy silicon substrate. The relationship between the variation in conductivity of the substrate and the Q-factor of the resonance was also studied as shown in Figure 6.15. Numerical simulations revealed that the performance of the emitter will be dramatically improved when the conductivity of substrate is increased from 0.05×10^6 S/m to 50×10^6 S/m. As the substrate becomes more conductive, more energy reflects into and resonances in the lossless SiO_2 and h-BN cavity which results into the

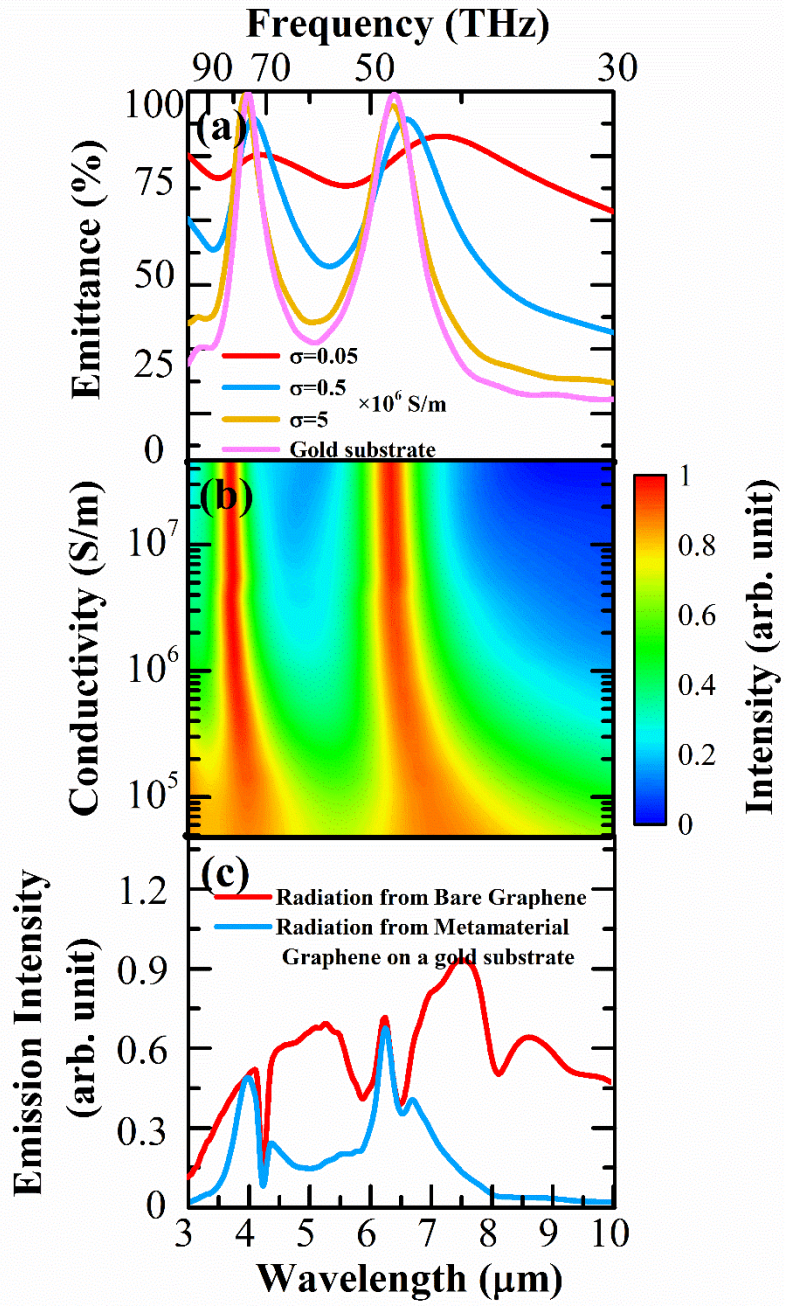

Figure 6.15 (a) and (b) Emission spectra for substrates with different conductivities. (c) Calculated radiation spectrum of the metamaterial-based graphene thermal emitter on an aluminium substrate (blue line) based on the measured radiation spectrum of a bare graphene thermal emitter (red line).

increasing decay rate of the emission peak. As a result, the amplitude together with the Q-factor of the emission peaks will be logarithmically increased. This feature results from the fact that the resonance of the metasurface at resonance wavelength will constructively interfere with the thermal radiation and consequently enhance the emission energy. As the silicon used in the fabrication is already the highest doped silicon wafer can be purchased from the commercial market, the Si/SiO_2 substrate needs to be replaced by an aluminium substrate on which a 300 nm-thick SiO_2 was ion beam sputtered as a spacer layer in order to increase the Q-factor from 6.5 to 13 (*Figure 6.16*).

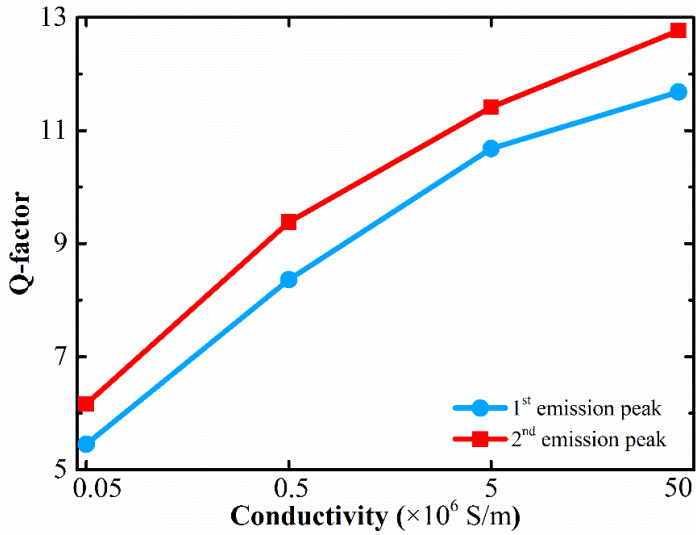

Figure 6.16 Calculated Q-factors of both emission peaks (blue line for 1st emission peak and red line for 2nd emission peak) for substrates with different conductivities.

6.7 Summary

In summary, a metasurface composed of annular ring resonator is first investigated for tailoring the randomly polarized, broadband emission from h-BN encapsulated graphene filament into a narrower bandwidth. Numerical simulations present that the electric dipole oscillation of the annular ring resonator can lead to an emission peak at a specific resonance wavelength. The annular ring resonator design is then extended to a fourfold 2×2 unit cell with a set of large annular ring resonators on diagonal direction and the other set of small annular ring resonators on anti-diagonal direction for the purpose of building up a gas sensor with dual emission peak, one interacting with the target gas while the other one providing the reference. Four emitters with such metasurface of different geometric parameters were designed for emission peaks located at various points between 3 - 8.5 μm. The initial measurements performed on the fabricated emitters were FTIR reflection measurements. Distinct overall spatial variations of total reflection intensity can be observed between the quadrants with and without metasurface. Normalized reflection spectra also demonstrate that all four devices exhibit a ‘W’ shaped spectral response at different resonance wavelengths due to the different radii and periodicities of the design, as we predicted. Similarly, when the devices are

driven by DC current, the emission measurement under FTIR with emission configuration also shows distinguishable total emission intensities from quadrants with and without metasurface. The normalized emission spectra all exhibit a dual-peak ‘M’ shaped spectra response as desired. Both the normalized reflection and emission spectra of four devices also show the resonance wavelengths increase with the increment in the radii of annular ring resonators, r_1, r_2 and periodicity p, all agree well with the simulated results, which can be concluded that such dual annular ring resonators metasurface design can be utilised to predictably tune the graphene emission spectrum. Finally, simulations show that the addition of a conducting layer below the SiO_2 layer can greatly increase the Q-factor of the resonance features in the emission spectrum. The possibility of tailoring the emission characteristics of these devices, which can reduce manufacturing costs and allow for modulation at relatively high frequencies, demonstrates their potential for use in applications such as infrared gas sensing.

7 Wave Trapping Sensor for Attenuated Total Reflection Spectroscopy

7.1 Introduction

As highlighted in previous chapters, the infrared region of the spectrum is highly attractive due to its use in providing a powerful, label-free, non-destructive analytical technique to identify chemicals [2,7,220]. The mid-infrared photon, whose energy ranges from 0.06 to 0.4eV, can be absorbed by the unique vibrational mode of specific chemical bonds. Since different bonds, or the same bond with different vibrational modes have their own unique infrared absorption spectra, known as the molecular fingerprint, corresponding to the photon energy they require to excite their vibrational transitions, this enables us to analyse the compound in the chemical by simply observing the spectrum obtained from an infrared spectroscopy. However, conventional infrared spectroscopies have two main drawbacks. Firstly, the interaction between the mid-infrared wave and molecule is weak due to the size mismatch. The spot size of the infrared wave is in the size of tens or hundreds of microns far bigger than the scale of atoms. So the spectroscopic measurement on trace amounts of analytes remains an intractable challenge [221]. Secondly, due to

the native aqueous environment of many analytes under test, the strong absorption of water will severely interfere with the measurements on the absorption of target molecules. Hence additional sample preparations, such as drying the samples or applying the samples in the form of a thin film with the same thickness [222], are required for the measurements which makes it unrealistic to characterize those samples in real time.

Attenuated total reflection (ATR) infrared spectroscopy, as introduced in Chapter 5.3, can be viewed as an improvement on the conventional infrared spectroscopy, to some extent overcomes both aforementioned disadvantages. Under ATR condition, the evanescent wave generated through total internal reflection mechanism interacts with the analytes will be confined within a distance, which is on the order of the wavelength, from the interface [223]. This dramatically reduces the detection volume of infrared radiation, which is normally the spot size in conventional infrared spectroscopy cases, and thus results in an enhanced light-matter interaction. Meanwhile, the water absorption is also suppressed under ATR condition which also allows straightforward analyses on samples in its aqueous form, without specific sample preparation [224,225]. Although the ATR approach has improved the capability of achieving qualitative measurement *in situ*, the relatively weak interaction between the infrared radiation and the analytes limits the sensitivity for quantitative analysis.

In order to make the light-matter interaction stronger, the evanescent wave needs to be confined in a subwavelength volume with minimal energy loss. Metasurfaces, once again turns out to be the solution as they offer high flexibility in controlling the propagation of surface waves and the resultant field distributions [226,227]. Pioneering research on such metasurface structure as aggregates [228], arrays [158], and nano-antennas [229,230] have already demonstrated the enhancement in absorption at the resonance frequency under conventional transmission or reflection setup. The localization of the collective oscillations of electrons at the surface enables those designs to confine the wave in a subwavelength scale area without significant energy loss.

In this chapter, an equivalent model was built to simulate the electromagnetic response of the device tested under ATR configuration. Based on that model, a metasurface design was proposed to enhance the interaction between the evanescent wave in mid-infrared and different trace chemical analytes. Different substrates, Si and Si/SiO_2 were used as substrates in fabrication to determine whether the phonon mode in SiO_2 will further improve the detection sensitivity.

From the result obtained, we show that a metasurface can be used to relatively easily increase the sensitivity of infrared attenuated total reflection

spectroscopy. Using such an approach, improved trace chemical detection was demonstrated in mixtures of butyl acetate and oleic acid, which are two important constituents in many foods. These results offer researchers, both in academia and industry, a new tool for higher sensitivity infrared spectroscopy that could be used, for example, to investigate the adulteration of food items.

Wavenumbers expressed in reciprocal centimetres, cm^{-1}, will be chosen as the major unit throughout the chapter as it is commonly used in spectroscopy. It will also be the primary axis for all spectrum figures while the frequency will be selected as the unit of the secondary axis for comparison. The conversion of a wavenumber in cm^{-1} to a frequency in THz should follow $f = c \times k /10^{10}$, where f is the frequency in THz, c is the speed of light and k is the wavenumber in cm^{-1}. Special thanks are given to the undergraduate students Ms Jacqueline Pitts and Mr Callum Penrose and my colleague Dr Prarthana Gowda for their assistance in making chemical solutions and doing the ATR measurements.

7.2 Modelling

7.2.1 Modelling of ATR configuration

It is clear that under the ATR configuration, it is the evanescent wave generated by the total internal reflection mechanism that interacts with the analytes. As a result, in order to investigate the responses of the device and

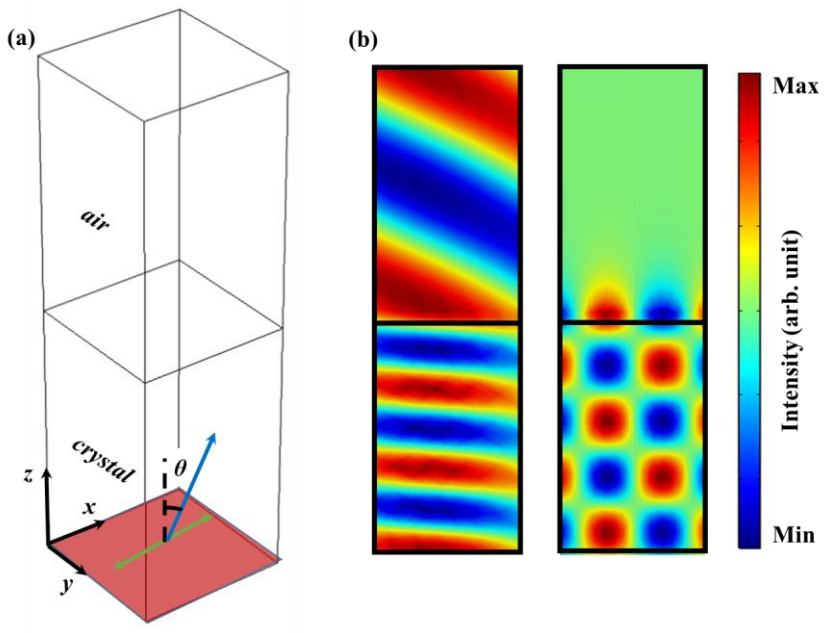

Figure 7.1 (a) 3D schematic of the simulation model used to generate evanescent wave with incident wave propagates along z-axis with an angle of incidence θ and electric field polarized along x-axis. (b)The electric field distribution in x-z plane at k = 1000 cm^{-1} with incident angle = 10° (left) and 45° (right).

analytes in an ATR setup, the evanescent wave is required to be used as the source in our simulation. Unfortunately, few commercial software packages can directly choose evanescent wave as the source for simulation. Here a simulation model, which is equivalent to the ATR setup used in our experiment as shown in Figure 5.8, is introduced for the purpose of generating the evanescent wave. The simulation model as schematically shown in Figure 7.1, generates the evanescent wave by total internal reflection through injecting an oblique incident wave on the diamond ATR crystal towards the air. The area highlighted in red is the source port, which generates an oblique electromagnetic wave along the blue arrow direction. The green arrow in the schematic shows the polarization of the wave. In addition, the refractive index of the diamond crystal is set to 2.64, same refractive index as the ATR crystal used in the measurement according to the manual and periodic boundary conditions are applied on all x-z and y-z boundaries. Here restricted by the shortage of FDTD method in simulation oblique source, FEM-based software COMSOL Multiphysics was used for all the simulation work in this chapter, as it performs much better in the case of simulating oblique incident wave with a broad frequency range. The electric field distributions in Figure 7.1(b) suggest that when the angle of incidence θ is low, wave beam can still penetrate into air through refraction while when θ increases, for instance θ = 45° as the

incident angle in our experiment, it can be seen that instead of getting any refraction, there is evanescent wave propagates along the interface between the crystal and air. This is also verified by the simulation results when the angle of incidence is swept from 0° to 45°. The reflectance as a function of incident angles shown in Figure 7.2, and clearly illustrates that total internal reflection condition is achieved when the angle of incidence exceeds θ = 22°, agrees well with the theoretical critical angle $\theta_c = sin^{-1}(n_{air}/n_{crystal})$ ≈ 22.5°.

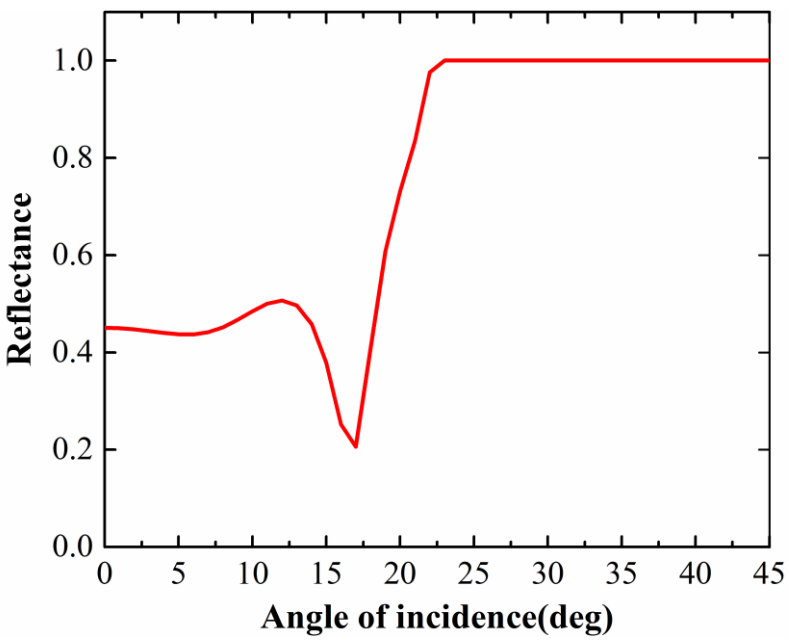

Figure 7.2 Reflectance obtained from the simulation model as a function of incident angle.

7.2.2 Modelling of the device

The metasurface designed for the aim of achieving high spatial confinement as well as enhancement of randomly polarized infrared radiation is a periodic gold complimentary annular ring resonator structure on top of a supporting substrate as schematically shown in Figure 7.3. The periodicity, p, in both vertical and horizontal directions are 4 μm; the inner radius of the ring, r, equals to 1.6 μm while the width of the air gap, w, is 300 nm. Non-doped silicon (ρ = 3000ohm·cm) was initially chosen as the substrate for our design attributed to its low absorption in the mid-infrared regime. The design was simulated in the configuration as introduced in the last section. Simulation result presented

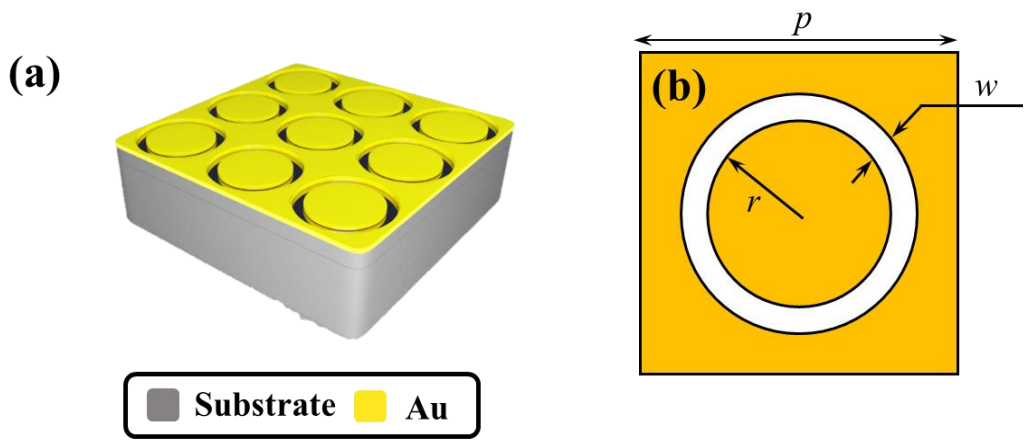

Figure 7.3 (a) 3D perspective view and (b) top view with geometric parameters of the device proposed for enhancing the sensitivity of ATR spectroscopy.

in Figure 7.4(a), shows a series of reflection minima throughout the spectrum. Investigations on the electric field distribution at the wavenumbers where reflection minima are observed were carried out to identify the origin of these spectral features. The magnitudes of the electric field, $|E|$, in Figure 7.4(b)&(c) indicate that those reflection minima correspond to the even-order resonance mode of the metasurface. As can be clearly observed, the electric field intensity is mainly confined at the top and bottom of the air gaps, forming a dipole mode for the resonance at 450 cm^{-1}. As the resonance frequency increases, the dipoles split into quadrupoles, hexapoles, and so on. Due to the oblique incident

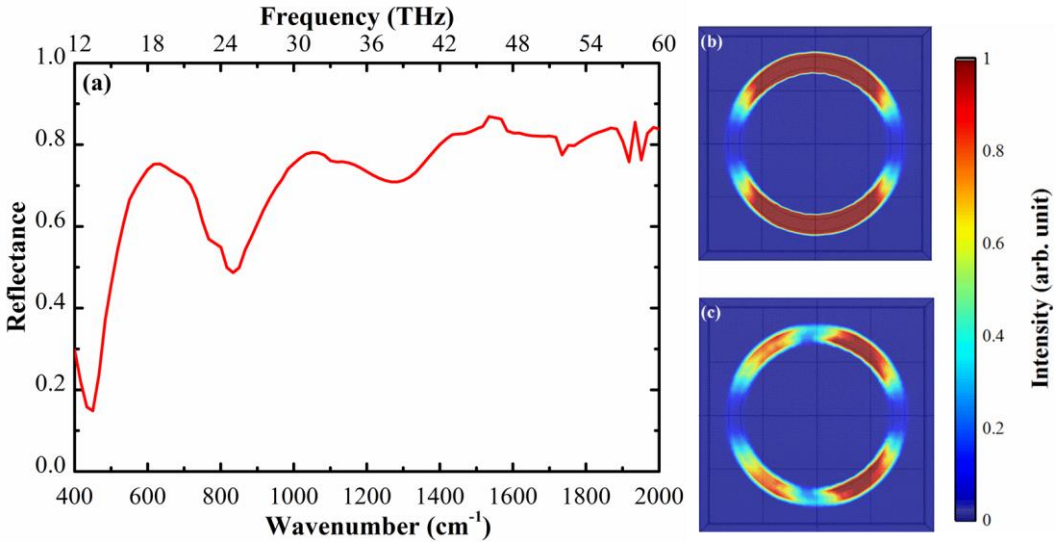

Figure 7.4 (a) Simulated reflectance spectra of the metasurface on Si substrate (b) and (c) shows the electric field distribution for x-y plane at 450 cm^{-1} (dipole mode) and 860 cm^{-1} (quadrupole mode).

of the electromagnetic wave in the ATR system the resonant modes also become less symmetric, and weaker in electric field confinement for a higher order of resonance. Although the confinement of the electric field in the small gap at its resonance mode is what we expected, the low reflectance at the resonant frequency which will directly lead to a low SNR and thus poor sensitivity for the measurement, make it not a good design for ATR system. In fact, having a good confinement of the energy at the surface of the device and achieving high reflectance from the device seems to conflict with each other. In order to overcome this obstacle, the substrate is changed to 300 nm thermal oxidized SiO_2 on top of the non-doped Si wafer. Previous research has proved the existence of surface optical phonon modes in thermal oxidized SiO_2 in the range of 400 to 1300 cm^{-1} [160]. By overlapping the resonance modes of metasurface and the phonon modes of SiO_2, these two modes will couple with each other and the energy trapped in the gap will excite the collective oscillation of phonons in SiO_2. Numerical simulations are conducted to prove the existence of this hybrid resonance model. The permittivity of SiO_2 is modelled by using the ionic dielectric function of the form:

$$\varepsilon_{SiO_2}\ \omega \quad = \ \varepsilon_\infty + \sum_{n=1}^{N} \frac{f_n \omega_n^2}{\omega_n^2 - \ \omega^2} + 1 \qquad (7.1)$$

where ω_n is the frequency of the n^{th} phonon mode, and their values are taken to be [464.8, 810.9, 1129.0] cm^{-1} for three phonon modes (N = 3), following data obtained from the literature [231,232], providing that $\omega_{SO,n+1}$ is larger than $\omega_{SO,n}$ under any circumstance. $f_n = \varepsilon_n - \varepsilon_{n+1}$ is the oscillation strength of the n^{th} mode, and are taken [0.75, 0.15, 0.60] and ε_∞ = 2.4 is the high-frequency dielectric constant for the SiO_2 substrate. Figure 7.5 shows the calculated real part and imaginary of the refractive index of SiO_2 which agrees well with previously reported values. Based on this, the dispersion diagram of the device on Si/SiO_2 substrate is also calculated by simulating the device with different scales, as shown in Figure 7.5. The figure clearly shows the coupling between the dipole and quadrupole resonance modes of the metasurface and the SO phonon mode of SiO_2 layer at 470 cm^{-1} and 1084 cm^{-1}. It should be noted that although SiO_2 also has another phonon mode at 810 cm^{-1}, the oscillation strength of phonon mode is only ¼ of the other two phonon modes, this makes its coupling with metasurface resonance mode quite weak. The data can be extracted from the dispersion diagram for the wavevector υ = 15.8×10^3 cm^{-1}, the same parameter as used for simulation of the device on Si substrate and compare the reflection spectra of both spectra. It can be observed from Figure 7.6 that despite of the slight blueshift of the resonance frequency caused by the lower refractive index of the SiO_2 layer, there now appears to be two

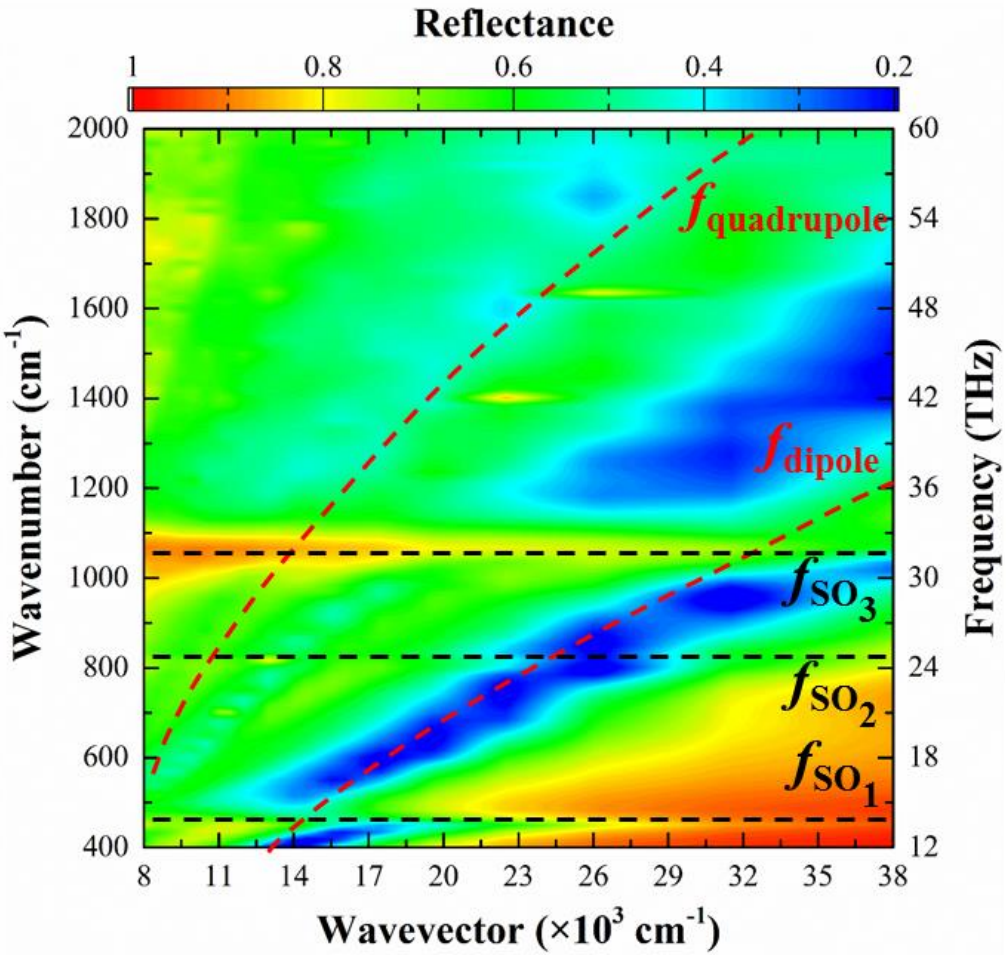

Figure 7.5 Simulated dispersion diagram of metasurface on Si/SiO_2 substrate. The two red dashed lines show the calculated resonance frequencies (dipole mode and quadrupole mode) of uncoupled metasurface. The three black dash lines represent frequencies of three surface optical phonon modes in SiO_2. The vertical white line represents the spectral response of the metasurface on Si/SiO_2 substrate presented in this paper.

peaks at the resonant frequencies of dipole mode and the quadrupole mode due to the hybridization of metasurface resonance and SiO_2 phonon mode. This hybrid resonance mode has a much higher Q-factor as well as reflection amplitude, which can reflect up to 80% of the signal back while confining the energy on the surface at 1100cm^{-1}.

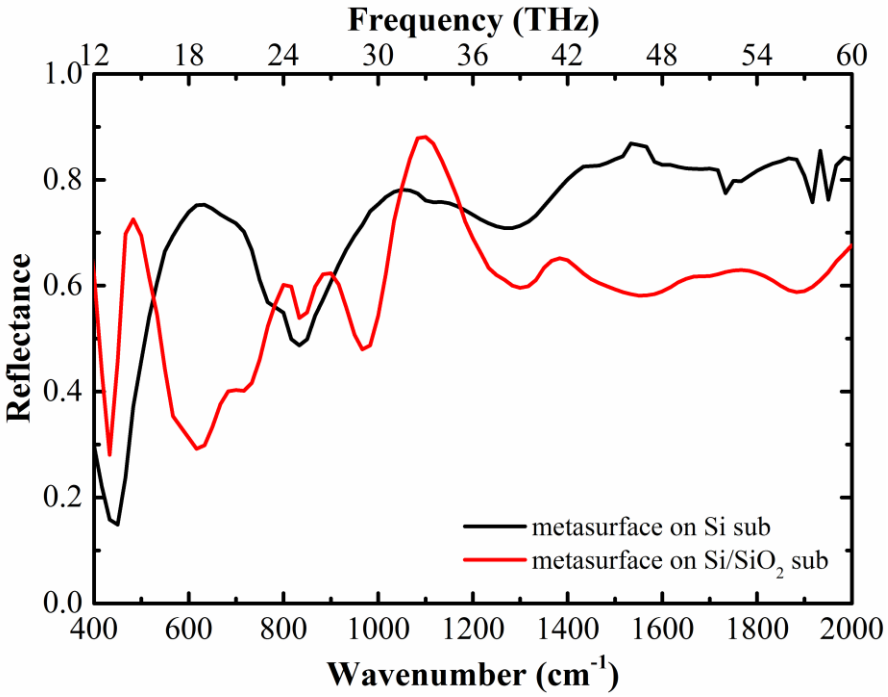

Figure 7.6 Comparison between the reflection spectra of metasurface on Si substrate (black line) and on Si/SiO_2 substrate (red line).

Device	p(μm)	r(μm)	w(nm)	Substrate
ATR-Si-M01	4	1.3	0.3	Si
ATR-SiO_2-M01	4	1.3	0.3	Si/SiO_2
ATR-SiO_2-M02	3.2	1.04	0.24	Si/SiO_2
ATR-SiO_2-M03	4.8	1.56	0.36	Si/SiO_2

Table 7.1 List of devices fabricated and measured in the experiment as well as their geometric parameters.

7.3 Fabrication and Measurement

7.3.1 Device Fabrication and Measurement

Four devices, as listed in Table 7.1, were fabricated using standard semiconductor fabrication technique as introduced in details in Chapter 4. The substrates chosen were 525 μm low-doped silicon (ρ = 3000~5000 Ω·cm) wafer and the same wafer but with 300 nm-thick thermal oxidized SiO_2 on the top, all commercially purchased from Inseto Inc. The metasurface was patterned on top of the substrates by using electron beam lithography, followed by gold deposition on the surface on the device using thermal evaporation and a lift-off process with the assistance of ultrasonication. The substrates were finally diced to ensure that only the area covered with metasurface will be left

on the device for testing. Fourier Transform Infrared Spectroscopy (Bruker Vertex 80v) in conjunction with Attenuated Total Reflection module (Platinum ATR Accessory) which has been introduced in Chapter 5 was used to characterize the devices first in the experiment. Spectra were recorded with 8cm^{-1} wavenumber resolution and 8.0 mm size aperture in the wavenumber range from 400 to 2000 cm^{-1} that are averaged over 256 scans per measurement. All samples were placed on top of the ATR spectrometer with the metasurface side of the device always facing the ATR crystal and a pressure application device was pivoted on the sample to ensure the distance between the ATR crystal and the metasurface is the same throughout the measurement. Figure 7.7(b) plots the reflectance spectra of the devices with the same metasurface structure but different substrate (ATR-Si-M01 and ATR-SiO_2-M01). Two minima in the reflection spectra of the metasurface on Si substrate (ATR-Si-M01) are observed at 450 and 858 cm^{-1} while two hybrid resonance modes occur at 476 and 1076 cm^{-1} instead for metasurface on SiO_2 substrate (ATR-SiO_2-M01). Measurements are also conducted on metasurface structure with different size scales on Si/SiO_2 substrate (ATR-SiO_2-M01, ATR-SiO_2-M02, ATR-SiO_2-M03). The reflectance spectra obtained from the measurement, shown in Figure 7.8(a) reveal that although the resonance of

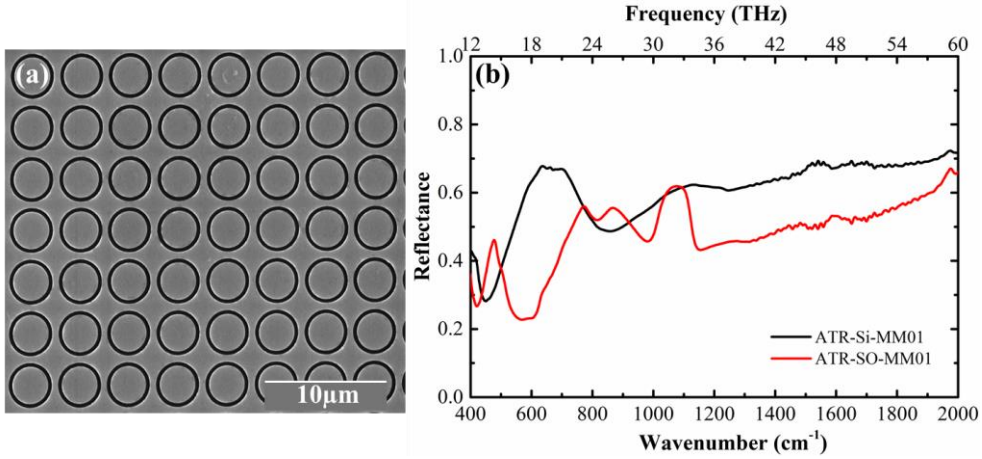

Figure 7.7 (a) the SEM photo of ATR-Si-M01; (b) measured reflectance spectra of ATR-Si-M01 and ATR-SiO_2-M01 under ATR configuration.

metasurface (indicated by ▼in different colours) will redshift with the increasing size of the metasurface structure, the wavenumber of hybrid resonance mode (indicated by ▲ in different colours) will remain the same due to the phonon in SiO_2 can only be excited at specific wavenumber. The corresponding wavenumbers of maxima and minima shown in the spectrum were extracted and overlaid on the dispersion diagram previously shown in Figure 7.5. It is quite clear to see all the minima (▼) drops in the blue area representing the metasurface resonance modes while the maxima (▲) all aligned in the red area which stands for the hybrid modes (Figure 7.8 (b)). The good agreement between the measurement results and simulation results proves the previous prediction that the coupling of phonon mode in SiO_2 and the resonance mode of metasurface can generate the hybridized resonance mode.

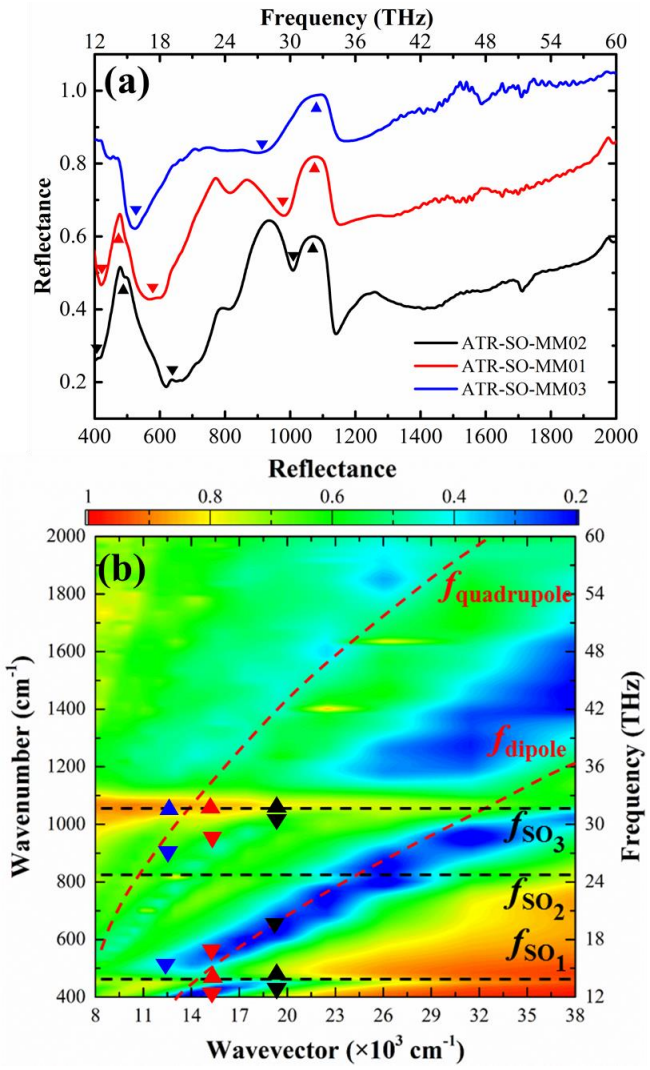

Figure 7.8 (a) Measured reflection spectra of metasurface with different scales on Si/SiO_2 substrate in the ambient atmosphere, spectra are consecutively shifted by 0.25 vertically for clarity; (b) dispersion diagram as shown in Figure 7.5 with extracted wavenumber of maxima and minima overlaid. ▼ and ▲ in blue, red and black corresponding to the maxima and minima observed in the spectrum of ATR-SiO_2-M03, ATR-SiO_2-M01, and ATR-SiO_2-M02 respectively.

7.3.2 Chemical Analytes Measurement

Butyl acetate and oleic acid were chosen as analytes in our experiment. Both chemicals are key constituents in most kinds of edible oil. Detecting the concentration of those two chemicals is thus crucial for identifying the quality and adulteration of the edible oil. In the experiment, the butyl acetate (purity ≥ 99.9%) and oleic acid (purity ≥ 99.9%) used were purchased from Sigma Aldrich. For each measurement, 5 µL of chemical was dropped uniformly on the surface of ATR crystal via an air displacement micropipette. Measurements were first carried out on pure butyl acetate and oleic acid. The measured absorption spectra of both analytes are shown in Figure 7.9, which are in agreement with the results shown in the online database [233,234]. A distinct difference in the wavenumbers of the characteristic absorption peaks between these two

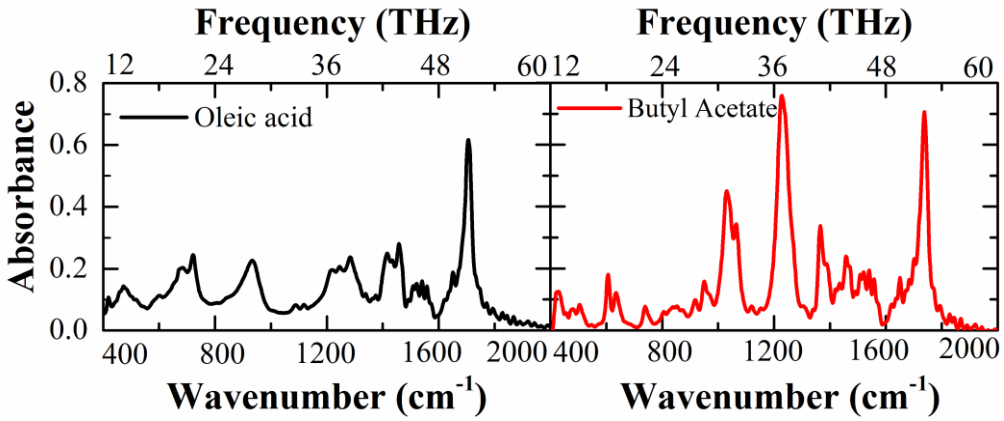

Figure 7.9 Measured absorption spectra of (a) 99.9% oleic acid and (b) 99.9% butyl acetate.

chemicals was observed due to their different molecular structure.

For example in the absorption spectra of oleic acid, the first fingerprint region between 660 cm^{-1} and 740 cm^{-1} are due to the overlapping of out-of-plane vibration of *cis-disubstituted* olefins and CH_2 rocking vibrations, the absorption peak at 933 cm^{-1} is attributed to the O-H out-of-plane bending vibration, the absorption peak occurring in the region between 1193 cm^{-1} and 1321 cm^{-1}, 1394 cm^{-1}, 1475 cm^{-1}, and at 1706 cm^{-1} result from the stretching vibrations of C-O bond, in-plane O-H bending vibration, and C=O stretching vibration in the carboxyl functional group [45]. As for butyl acetate, several extra peaks can be observed at 595 cm^{-1} to 642 cm^{-1} which is due to the in-plane bending vibration of O-C=O group, 1029 cm^{-1} and 1250 cm^{-1} which are both led by the C-O vibration, and 1737 cm^{-1} due to the C=O stretching vibration from ester functional group [45]. Furthermore, butyl acetate was then diluted with different amount of oleic acid and produced four different liquid mixtures, 0.1%, 1%, 10% and 99.9% acetate, for testing the sensitivity of an ATR system in detecting the concentration of chemicals. The measured absorption spectra for different concentration of butyl acetate are plotted and compared in Figure 7.10. The extinction ratio spectra between the chemicals, calculated as$(I_1 - I_2)/I_1$, where I_1 is the measured amplitude of referenced chemical and I_2 is

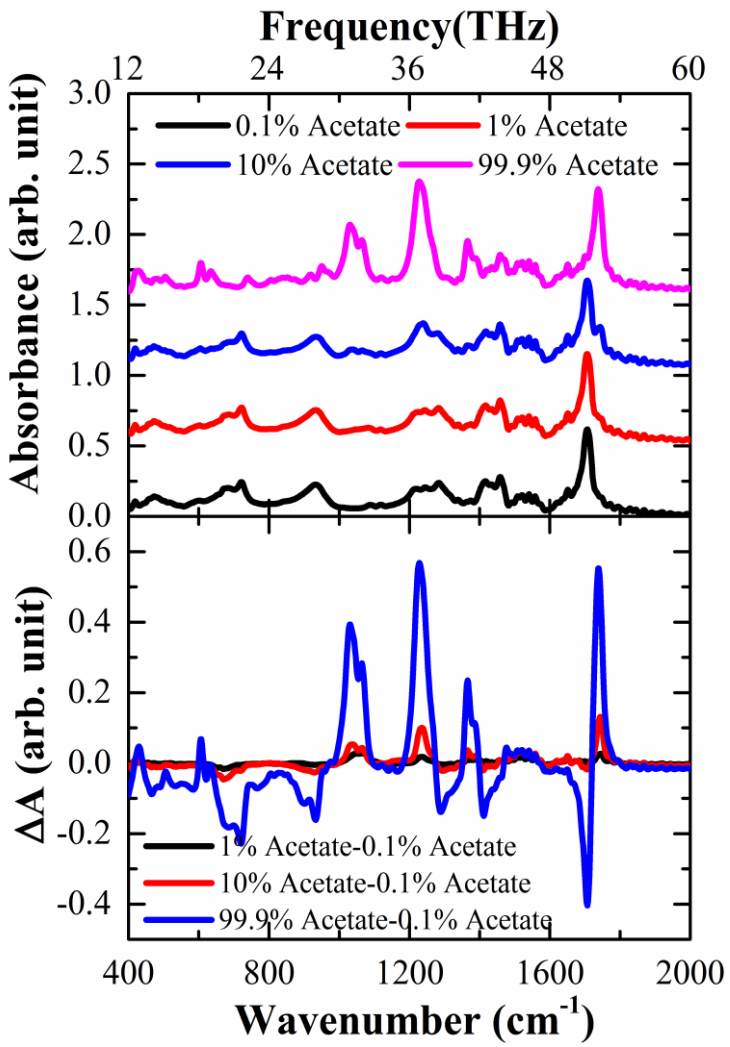

Figure 7.10 Measured absorption spectra for mixtures in the ambient atmosphere, spectra are consecutively shifted by 0.5 vertically for clarity; (b) Extinction spectra for mixtures without the presence of metasurface.

that of the chemical for comparison, demonstrate the current limitation of FTIR-ATR in detecting trace chemicals, it is able to detect analytes with a large difference in concentration, but unable to distinguish samples with a slight difference in concentration. In this case, it's the butyl acetate peak at 1029 cm-

[1], although it is easy to distinguish 99.9% butyl acetate from the rest three mixtures, the discrepancy between the other three mixture is hard to be observed. 10% butyl acetate yields an insignificant difference of 0.016 in this peak's absorption intensity from 1% acetate meanwhile the difference between the 0.1% butyl acetate and 1% butyl acetate is negligible.

7.3.3 Measurement of Chemical Analytes with metasurface devices

The electromagnetic response of these various concentrations of butyl acetate with ATR-Si-M01 and ATR-SiO_2-M01 was then measured for comparison. The pipette was again used to drop the mixture analyte on the crystal first, and then the metasurface devices with its metasurface structure facing towards the crystal were pressed firmly on the analyte via the pressure application device to ensure the same pressure. The absorption spectra for different mixtures in the presence of metasurface devices are calculated by normalizing the measured spectra of different concentrations of acetate with metasurface devices to that of metasurface devices along ($(I_{chem+MM+sub} - I_{MM+sub})/I_{MM+sub}$), as shown in Figure 7.11 and Figure 7.12. For the chemical analytes together with ATR-Si-M01, apart from the major fingerprint absorption

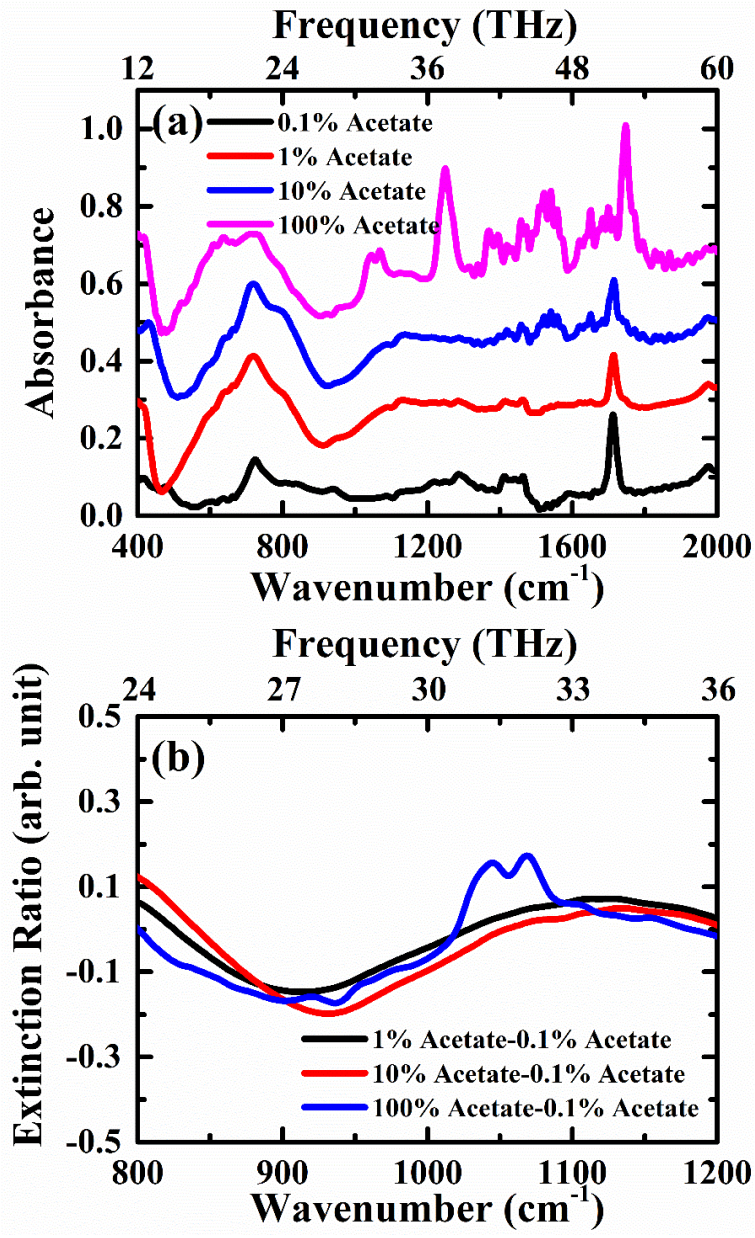

Figure 7.11 (a) Measured absorption spectra of mixtures in the presence of ATR-Si-M01 in the ambient atmosphere, spectra are consecutively shifted by 0.2 vertically for clarity; (b) zoomed extinction spectra of mixtures in the presence of ATR-Si-M01 for the carbon oxygen stretching band region between 800 cm^{-1} and 1200 cm^{-1}.

peaks which introduced in the article above, two main dips can be observed at 500 cm^{-1} and 950 cm^{-1} in Figure 7.11(a). These two dips resulted from the dipole and quadrupole resonance modes of the metasurface, proved that the interaction of metasurface on chemical analytes. These two resonance modes also shifted to a lower frequency with the increase in the concentration of butyl acetate. In this case, as the refractive index of butyl acetate is higher than that of oleic oil, this leads to the effective refractive index of metasurface with biological samples becomes higher with the increasing percentage of butyl acetate. However, apart from this tiny blue shift of both resonance dips, it is still not trivial to tell the difference between 0.1%, 1% and 10% butyl acetate from the extinction spectrum shown in Figure 7.11(b). For the measurements of chemical analytes with the presence of ATR-SiO_2-M01, there is much more overlap between the resonance modes of the metasurface and the vibrational modes in butyl acetate. This overlap has a strong effect on the measured FTIR-ATR spectra for the different mixtures on the metasurface, which are plotted in Figure 7.12(a). The plot of the extinction ratio, Figure 7.12(b), shows how the shape of the spectra now changes with the concentration of butyl acetate, indicative of coupling between the vibrational resonance of butyl acetate at 1029 cm^{-1} and the hybridised metamaterial phonon mode. As the concentration of acetate increases, the minimum seen at ~1000 cm^{-1} (marked by a black

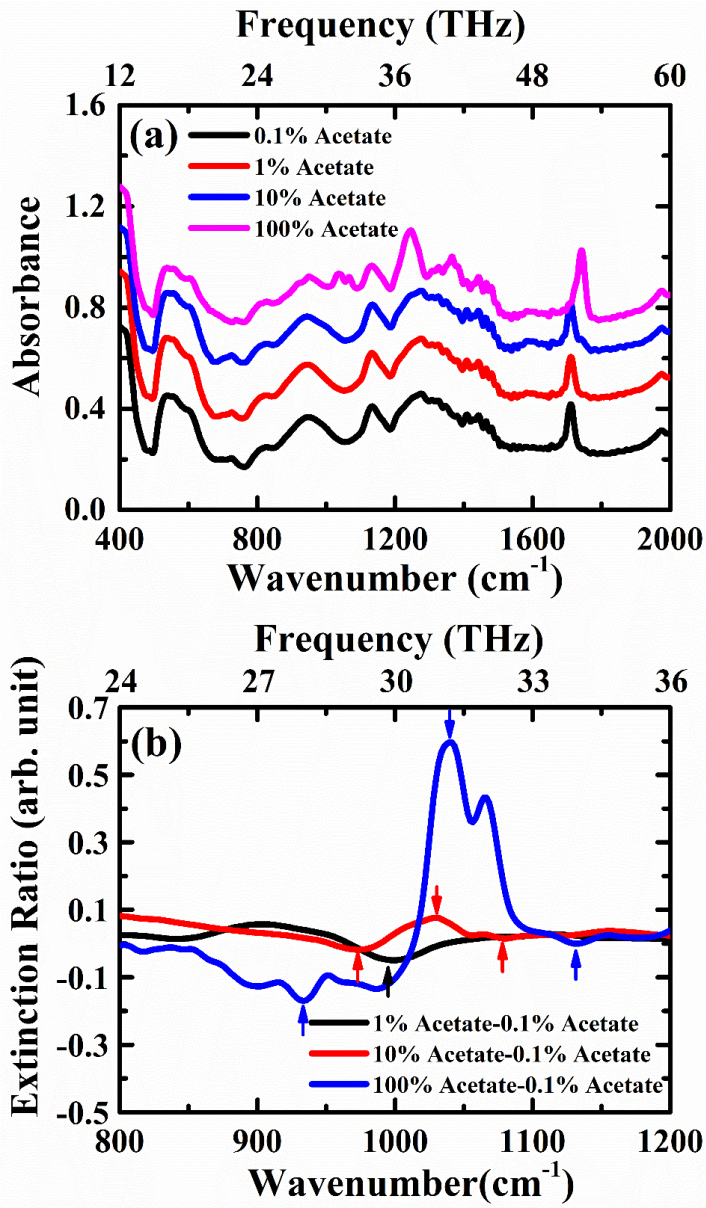

Figure 7.12 (a) Measured absorption spectra of mixtures in the presence of ATR-SiO_2-M01 in the ambient atmosphere, spectra are consecutively shifted by 0.2 vertically for clarity; (b) zoomed extinction spectra of mixtures in the presence of ATR-SiO_2-M01 for the carbon–oxygen stretching band region between 800 cm^{-1} and 1200 cm^{-1}.

arrow) splits into two minima (marked by up arrows in red) and form maxima in the middle (marked by a down arrow in red). In this case, even in the mixture containing only 1% butyl acetate, a clear maximum is seen in the measured spectra at around 1020 cm^{-1}. The coupling becomes even stronger for pure butyl acetate (see blue arrows), which results into the increase in the extinction ratio.

In summary, a COMSOL model was first used to generate evanescent wave as that produced by an FTIR spectroscopy with ATR configuration. With the assistance of this ATR-equivalent model, a complimentary annual ring resonator was investigated. Numerical simulation results present that at certain wavenumbers, the metasurface will produce resonance in a dipole mode, and this resonance mode will split into higher even-order resonance mode with increasing wavenumber. The electric field distribution also confirms that the electric field will be trapped in the annual gap at resonance modes which will potentially increase the sensitivity of ATR spectroscopy due to the enhancement in the interaction between molecular vibrations and the mid-infrared evanescent waves in an ATR setup. The design was patterned onto both Si and Si/SiO_2 substrates as simulation shown that the phonon modes in SiO_2 should couple with the metasurface resonance mode according to the simulation and further increase the sensitivity of the measurement. The spectral

properties of both devices were characterised using an FTIR-ATR system. Resonant features were observed corresponding to the resonance of the metasurface on the Si substrate device, and the hybrid resonance of phonon modes and metasurface resonance on the Si/SiO_2 substrate, both in good agreement with simulations. Preliminary experiments were undertaken using four different mixtures of butyl acetate diluted with oleic acid. Without the use of a metasurface, the minimum concentration of butyl acetate that could be detected was 10%, whereas the use of the metasurface on the Si/SiO_2 substrate allowed the detection of 1%, due to the coupling of the vibrational resonances of the butyl acetate with the hybridised metamaterial phonon mode. These results demonstrate the potential of the use of metamaterials to improve the sensitivity of FTIR-ATR measurements, and offers a new route for improved trace chemical detection.

8 Graphene-based Mid-infrared Modulator

8.1 Introduction

It has been illustrated in the last two chapters that a metasurface can be used to control mid-infrared light spectrally and spatially. However, the metasurface devices described so far are considered to be passive as their response to mid-infrared light are fixed with the geometric parameters of the metasurface structure. For example, to change the emission wavelength of the metasurface-based graphene thermal emitter introduced in Chapter 6, another emitter with different geometric parameters has to be fabricated to achieve this goal. Lack of sufficient tunability limits the applications of conventional metasurface devices in certain fields like high data rate communication [132,133], reconfigurable surfaces [235,236], and imaging [237], etc. Intensive efforts have been made to control the response of metasurface devices dynamically [132-238], as modulators are of paramount importance for tunable devices. Although those fast, highly tunable modulator can easily be achieved by integrating metasurfaces with varactor diodes for millimetre wave [123,235] or compound of semiconductors like GaAs for terahertz band [132], such modulators in the mid-infrared range remain challenging due to a limited choice

of materials. Modulators based on electrical controlled liquid crystal (LC) [122] or thermal controlled vanadium dioxide (VO_2) [135] suffer from slow modulation speed, while others based on semiconductor quantum wells require precise control on material growth and temperature [238]. Recent work has also investigated devices based on a combination of a MEMS (micro-electro-mechanical-system) platform and metasurface to steer mid-infrared light [239], but such devices require sophisticated integration techniques to realize.

Thanks to its unique gapless band structure, graphene, whose carrier density can be easily and smoothly controlled by shifting the Fermi levels, provides a highly tunable conductivity via electrostatic gating, or optical excitation [210,240,241]. This modulation usually can be accomplished within the order of nanoseconds, far quicker than the conventional LC and VO_2 modulators. Thus, integrating graphene into metasurface is a promising approach for designing active mid-infrared modulators. Although up to now, theoretical studies have been intensively conducted on patterned graphene modulator [242,243] and graphene-integrated metasurface modulator [244-247], not too many experimental results are reported.

In this chapter, we present the experimental demonstration of a high-speed, compact graphene integrated metasurface mid-infrared modulator, which

allows a wide range of amplitude and phase modulations by tuning the Fermi level of graphene with gate voltage control. The tunability achieved by the design architecture of our device is essential for obtaining a highly modulated phase under ambient conditions. Furthermore, a prototype mid-infrared reconfigurable surface is proposed to function as a beam steering lens, realizing the switch from normal reflection to anomalous reflection with a high conversion efficiency and responding time.

8.2 Design

Our design integrates monolayer chemical vapour deposition (CVD) graphene into a metasurface Salisbury screen absorber, as sketched in Figure 8.1(a). The Salisbury screen absorber, named after American engineer Winfield Salisbury, was originally designed as an absorbent device for radar detection, and consists of three layers: a frequency selective surface (FSS) on the top, a lossless dielectric spacer layer, and a metallic ground plane to block all the wave propagations. As fully explained in § 2.3.2, the reflection from the device can be totally eliminated when the impedance matching condition is fulfilled, i.e. the effective impedance of the device Z_{eff} is equal to that of the wave in free space Z_0. The circuit diagram of the structure is shown in Figure 8.1(b), in

which Z_0 and Z_1 are the wave impedance of free space and the dielectric layer, respectively. Z_M is the impedance of metasurface and σ_{Gr} is the conductivity of monolayer CVD graphene. As the metasurface can be viewed as an RLC circuit, which can be used to match the wave impedance of free space and the device at the desired frequency. In addition, due to the integration of the monolayer graphene into the metasurface, the effective impedance of the graphene integrated metasurface can be directly tuned by shifting the Fermi energy level of the monolayer graphene via optical excitation

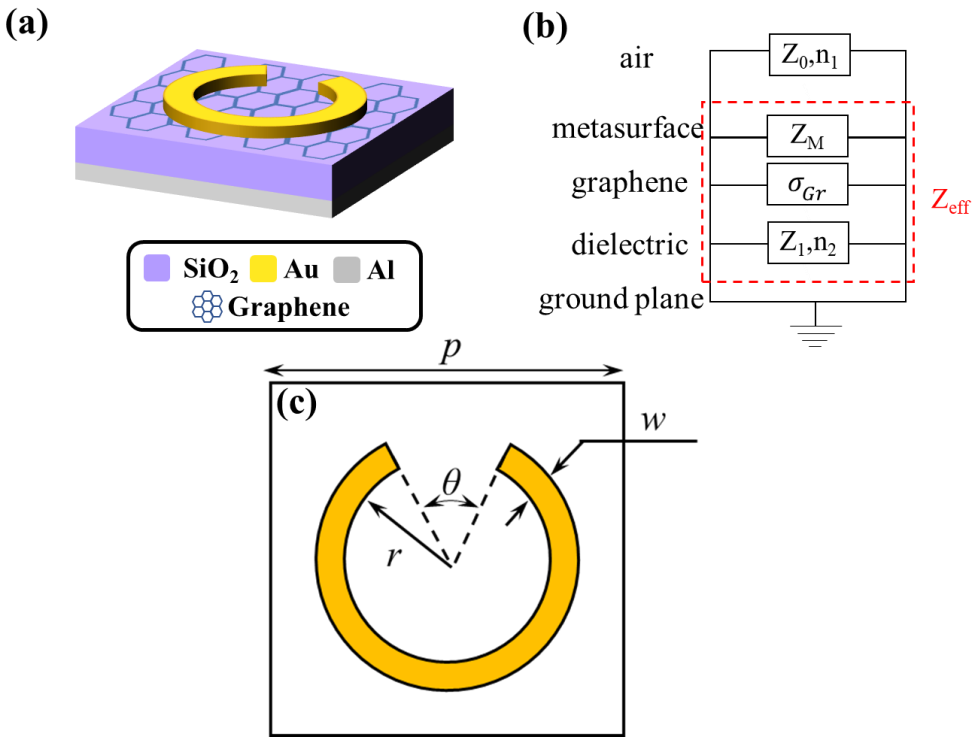

Figure 8.1 schematic of the graphene metasurface modulator (a) 3D view, (b) equivalent circuit diagram (c) top view.

or electrostatic gating. This will shift the frequency at which the impedance matching condition is met, thus leading to a dynamical control on the reflection spectrum.

The metasurface design, shown in Figure 8.1(c), is a split-ring resonator (SRR) structure as it leads to better confinement of energy, which is critical in obtaining a wide range of tunability. The inner radius of the SRR is r = 900 nm, with w = 200 nm ring width and θ = 32° angular split gap on the ring. The SRR is arrayed in both vertical and horizontal direction with the same periodicity p = 2.8 µm. The thickness of SRR is set to 100 nm, the same as that of the ground plane, while the thickness of SiO_2 spacer is chosen as 300 nm. Numerical simulations were carried out using Lumerical FDTD solutions. Unlike the previous two designs in Chapter 6 and 7, this design is sensitive to the polarization of the electric field due to its asymmetric geometry. In order to stimulate the resonance of SRR, the polarization of the electric field is set parallel to the direction of the gap. Moreover, in the simulation, the conductivity of the aluminium ground plane and gold SRR are set as 3.77×10^7 S/m and 4.1×10^7 S/m, respectively [248], and a value of 1.35 for the refractive index of ion beam sputtered (IBS) SiO_2 spacer layer according to the datasheet provided from the wafer manufacturer, Laseroptiks. The monolayer CVD graphene sandwiched between FSS and spacer layer in this device is modelled as a

conductive surface whose complex conductivity $\sigma(\omega, \mu_c, \tau, T)$ is defined by a simplified Kubo formula presented as equation (2.20) in Chapter 2. The parameters in this formula are chosen as T = 300 K for room temperature and τ = 50 fs for the carrier relaxation time, consistent with the measurement of the carrier mobility in similar devices [157,160]. Solid curves presented in Figure 8.2 are the calculated conductivities of monolayer graphene with different Fermi energy levels. An increase in the conductivity of the graphene is observed with higher doping level.

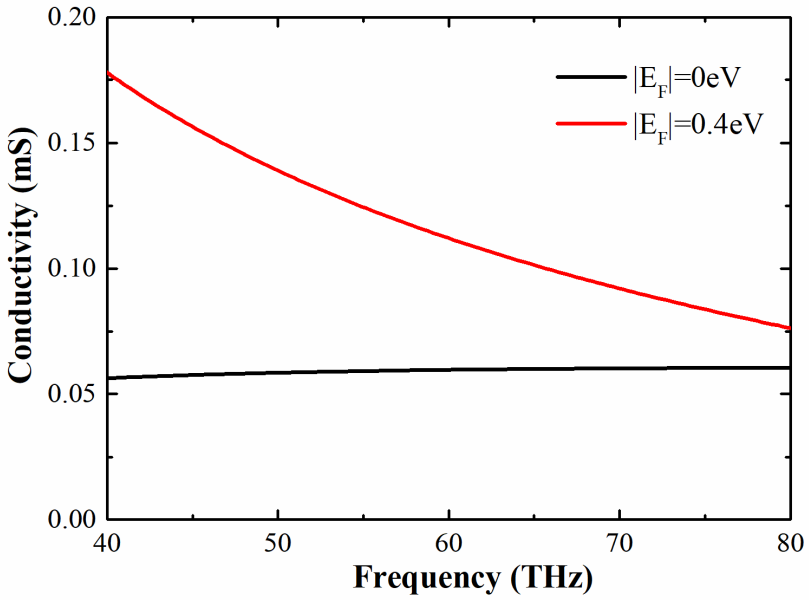

Figure 8.2 Calculated conductivity of non-doped ($|E_F|$ = 0 eV) and doped ($|E_F|$ = 0.4 eV) monolayer graphene-based on simplified Kubo formula.

The simulated reflection spectra, together with the relative effective impedance $z = Z_{eff}/Z_0$ retrieved by the method introduced in § 2.3.2 are plotted in Figure 8.3 for devices with non-doped graphene and doped graphene

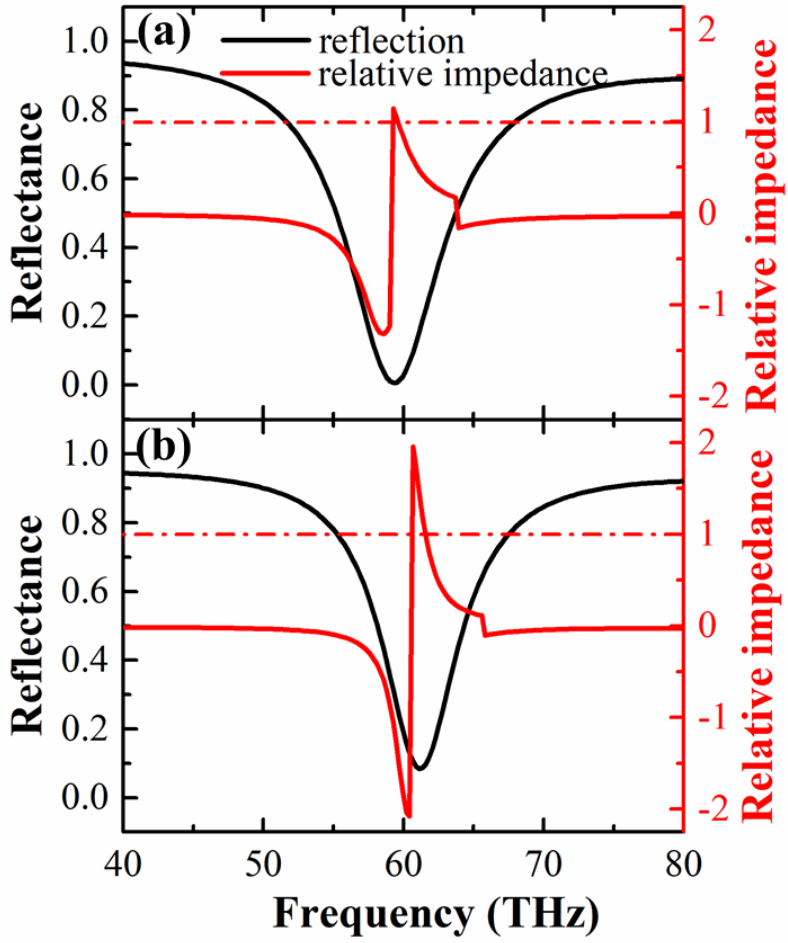

Figure 8.3 Reflection and normalized effective impedance spectra of designs with (a) non-doped graphene ($|E_F|$ = 0 eV); (b) doped graphene ($|E_F|$ = 0.4 eV). Minimum of reflection occurs when the normalized effective impedance equals to 1 (Z_{eff}/Z_0 = 1).

with $|E_F|$ = 0.4 eV. It shows clear evidence that the reflection minimum in the

spectrum occurs when the effective impedance is equal to the free space wave impedance (relative effective impedance z = 1). Furthermore, it also proved the effective impedance of the device is also changed due to the difference between the conductivity of graphene with different Fermi energy levels. This results in a shift in the intersection between the relative effective impedance and the impedance matching line (z = 1), and consequently move the frequency of reflection minimum in the spectrum from 59.2 THz to 61.3 THz.

Previous research has already proved it is practicable to tune the Fermi energy level of graphene between 0 eV and 0.4 eV by electrostatic gating. Numerical simulations were undertaken for designs with a number of different Fermi energy levels within that range. Figure 8.4(a) demonstrates that the frequency at which the reflection minimum occurs is directly dependant on the Fermi energy level of graphene. As a result of the spectrum shift, a modulation of amplitude at a certain frequency in reflection is obtained. For example, at 60 THz, a 40% modulation width in reflectance can be achieved by this design. In addition, following the method of Smith et al [62], precise phase information of the reflected wave is also extracted by subtracting the additional propagation phase from the wave source to the device and the device to the monitor. Substantial phase modulation can be observed in Figure 8.4(b) accompanied with the change on reflection amplitude when the Fermi level increases. The

phase modulation reaches a maximum of 150° at 60 THz when the Fermi level increases from 0 eV to 0.4 eV.

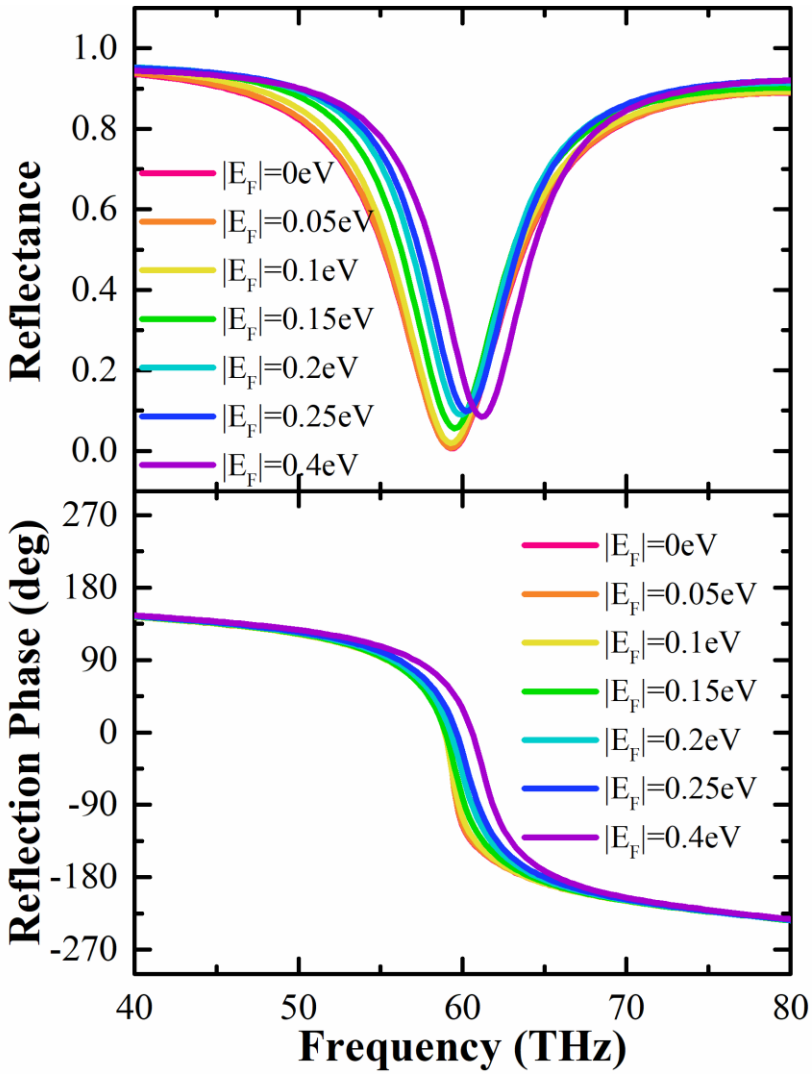

Figure 8.4 (a) Simulated reflection spectra and (b) retrieved phase information of reflection from designs with Fermi level of graphene ranging from 0 eV (non-doped) to 0.4 eV (doped).

The field distribution was also investigated to see the interaction between the ring resonators and the graphene. As shown in Figure 8.5, the electric field is highly confined in the gap of SRR both in x−y plane (laterally) and along z-axis (vertically). Since this strong localized field overlaps with the graphene, this strong coupling can introduce a wide tuning range to the device.

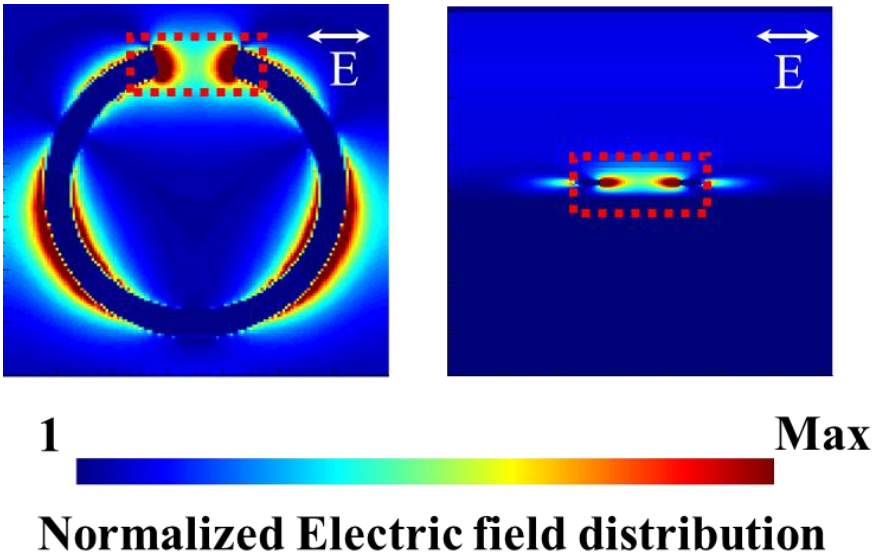

Figure 8.5 cross-sectional normalized electric field distribution at 60THz in the x-y plane (left) and in the x-z plane intersecting the gap of SRRs (right).

8.3 Experiment

Devices were fabricated by patterning periodic SRR arrays on a CVD graphene heterostructure. The whole fabrication process first started with

transferring monolayer CVD graphene on top of the substrate, which is a 300 nm-thick silicon dioxide (SiO_2) spacer layer and a 50 nm-thick Al layer ion beam sputtered on the silicon wafer. The graphene layer was then etched into a 2 cm×2 cm square by reaction ion. An array of periodic split-ring resonators as shown in Figure 8.6(a), together with electrical contacts, were patterned by electron beam lithography (EBL) and metalized by chromium and gold via thermal evaporation on this graphene square. The sample was finally mounted and wire bonded to a ceramic chip carrier for characterization, as shown in Figure 8.6(b)

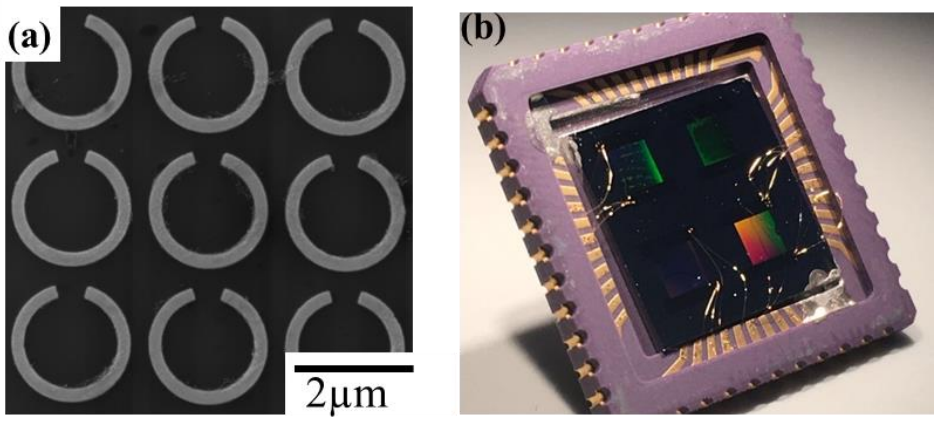

Figure 8.6 (a) SEM image and (b)photograph of the fabricated device.

Field effect characteristic of the device was first measured by the setup schematically shown in Figure 8.7(a). The resistance of graphene (R_{Gr}) with patterned metasurface, which was calculated by monitoring the voltage drop on

the electrodes (V_{DS}) with a constant 100 nA source-drain current (I_{DS}), is measured as a function of the applied gate voltage (V_G).The calculated resistance is then compared to that of the device without the metasurface. Measured field effect curves plotted in Figure 8.7(b), without too many differences, both show a peak value of resistance at V_G ≈ 60 V corresponding to the charge neutral point (CNP) where Fermi level is at Dirac point (|E_F| = 0 eV). Such result suggests that the metasurface doesn't have a huge impact on the field effect characteristic of the graphene as expected, and the CVD graphene used has a significant intrinsic hole doping indicated by the large positive value of V_{CNP} which is consistent with the previous experimental results [160].

Investigations were then conducted on how the reflection spectrum of the device can be dynamically controlled by the gate voltage driven on the device, the sample was mounted on a chip holder and measured in an FTIR spectroscopy with reflection setup. A polarizer was added to ensure the mid-infrared light sourced from FTIR is linearly polarized in the direction parallel to the gap of the SRRs. A surface scan was then run to locate the position of the metasurface structures and the spatial variation of reflectance is shown in Figure 8.8(a). The area with the smallest overall measured reflection intensity,

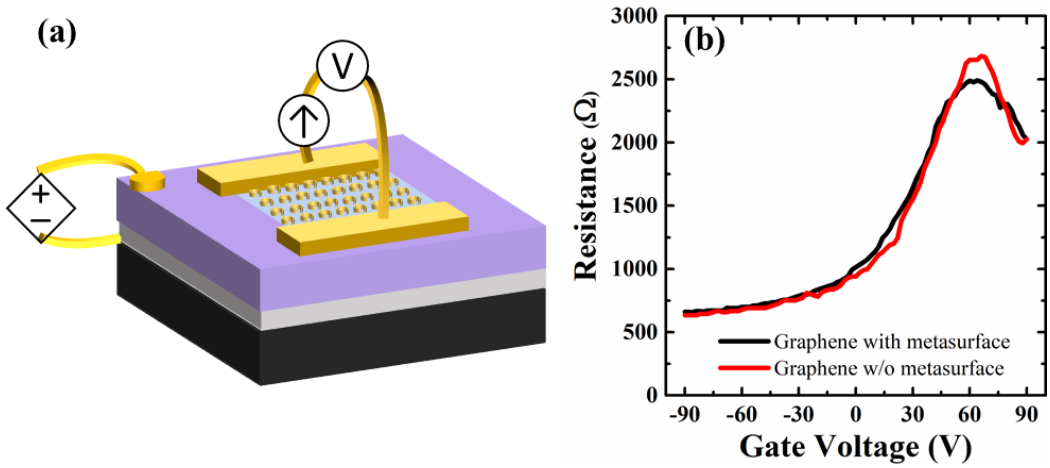

Figure 8.7 (a) schematic of the field effect characteristic measurement setup (b) Field effect characteristic curves of graphene with metasurface patterned on the top and without metasurface on the top.

the blue region in the middle of the image, corresponds to the location of the SRRs patterned on the graphene, as the metasurface cancels out the reflection at its resonance frequency where the impedance matching condition is fulfilled. After determining the location of the metasurface area through spatially resolved reflectance measurements, spectral measurements were carried out under atmospheric conditions from the middle of this area, with applied gate voltage varied from -90V to 90V. Results in Figure 8.8(b) revealed the frequency of main reflection minimum shifts from 59.47THz when graphene is at its CNP (V_G = 60 V) to 60.4 THz when a -90 V gate voltage is applied (note that at the feature at 70THz is due to the presence of CO_2).

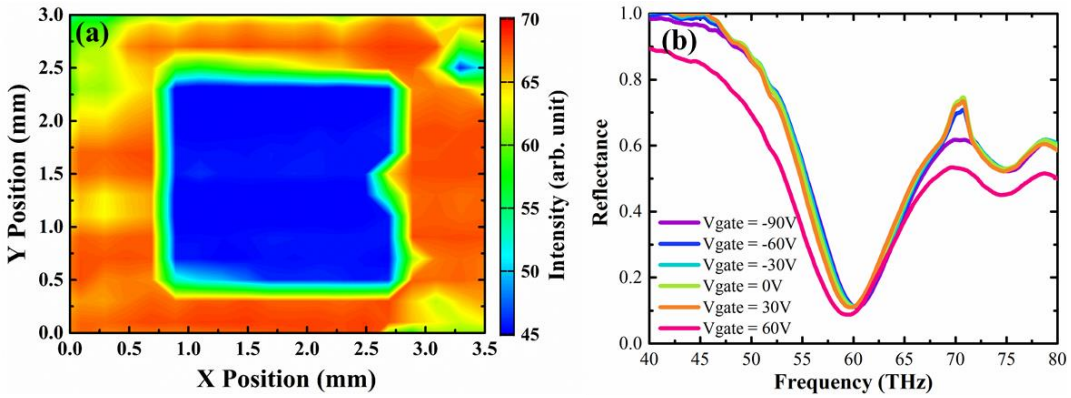

Figure 8.8 Spatially resolved reflectance map from the graphene metasurface modulator (b) Measured Reflection Spectra of graphene metasurface modulator with gate voltage ranging from -90 V to 60 V (V_{CNP}).

In order to compare the simulation results to the experimental results directly, the relationship between the Fermi level (E_F) of the graphene in the model and the gate voltage applied on the device can be determined by Equation (2.15). In our case, the charge neutral point is V_{CNP} = 60 V and the gate voltage varies from -90 V to 90 V, so that the gate voltage range applied in the experiment corresponds to the Fermi energy level of graphene ranging from 0 eV to 0.288 eV in the simulation. The frequencies at the reflection minima in both simulation and experiment spectra are extracted and plotted as a function of gate voltage for comparison. As shown in Figure 8.9, there is good agreement between the simulation and experimental results regarding the frequency at which the

reflection minimum is observed. The slight differences between the simulation and experimental results are mainly due to the fact that in the experiment the incident light is not exactly a plane wave because of the use of a reflecting objective lens [249]. In addition, the extra contact pads and bonding wires on the device may also retransmit electromagnetic signal and therefore affects the resonance performance of the modulator.

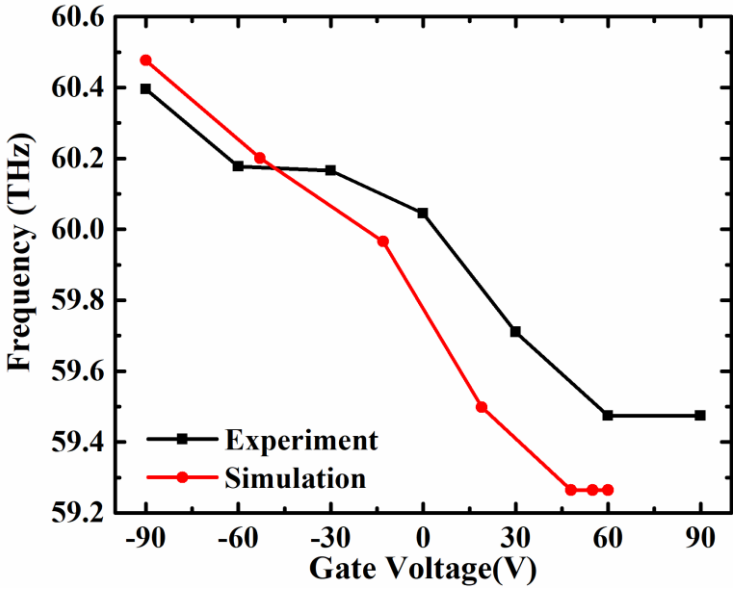

Figure 8.9 Extracted resonance frequency as a function of gate voltage, the same extracted simulation data is also presented here for comparison. For the simulation curve, the gate voltage is converted from the Fermi level by Equation (2.15). (Lines are guided for the eye and not fitted curves)

8.4 Application

The wide amplitude and phase modulation achieved by our modulator design make it an ideal building block for reconfigurable metasurfaces, which have a wide range of promising applications such as countermeasures to radar detection [235], compact lenses [250,251], beam steering devices [130,252], dynamic holograms [236,253,254], just name a few. Here we construct a reconfigurable metasurface by using the same metasurface design with different geometric parameters. Proof-of-principle simulation results of such graphene-integrated beam steering metasurface show the capability of reflecting the reflective beam to an anomalous angle under a normal incident plane wave at 60 THz when the graphene is electrostatically gated.

As mentioned in § 2.3.2 if a phase discontinuity is introduced at the interface between two media, the beam will be reflected to an anomalous angle, which can be calculated from Equation (2.13). Due to the graphene metasurface modulator is capable of achieving a wide range of phase modulation, we can dynamically control the phase gradient $d\Phi/dx$ along the interface and thus manipulate the direction of the reflection. The geometric parameters of the modulator design were swept to find four designs that can cover a linear spatial phase profile from 0 to 2π at 60 THz when the Fermi level of graphene is 0.4eV

and have nearly identical reflection phases when the Fermi level of graphene returns to the Dirac point. This enables the interface to reflect the incident wave specularly when no gate voltage is applied on the lens, and to deflect the wave anomaly when a gate voltage is driven.

The geometric parameters of four specifically designed modulators are shown in Table 8.1. If a lens is constructed by periodically aligning four modulators into a 4×1 super cell as illustrated in Figure 8.10(a), the phase profile in Figure 8.10(b) shows that there is a neglectable phase discontinuity in the phase profile along the interface when the graphene is non-doped ($|E_F|$ = 0 eV) ,and when the graphene is doped, a $d\Phi$ = π/2 phase increment between two adjacent modulators along x-axis direction will be established as soon as the Fermi level of graphene increase to 0.4eV. In this case, by changing the voltage added on the metasurface lens directly, we can alter the reflection angle from 0° to 29.6° at 60THz, according to equation (2.13). Figure 8.11(a) and (b) demonstrate the simulated farfield scattering pattern of the device in polar coordinates, which clearly show the beam is steered by 30°, in great agreement with the theoretical reflection angle. The steering efficiency, the intensity of wave at deflection angle normalized to that of the incident wave, can reach up to 45%, can be attained. This efficiency can be even higher if

more modulators are added into the super cell to overcome the discreteness of the phase discontinuity along the interface.

Modulator	r1 (nm)	w (nm)	θ (deg)	p (nm)	Graphene integrated?
1	900	120	20	2600	No
2	900	220	32	2600	Yes
3	900	120	20	2600	Yes
4	1120	70	66	2600	Yes

Table 8.1 Geometric parameters of modulators used in beam steering lens

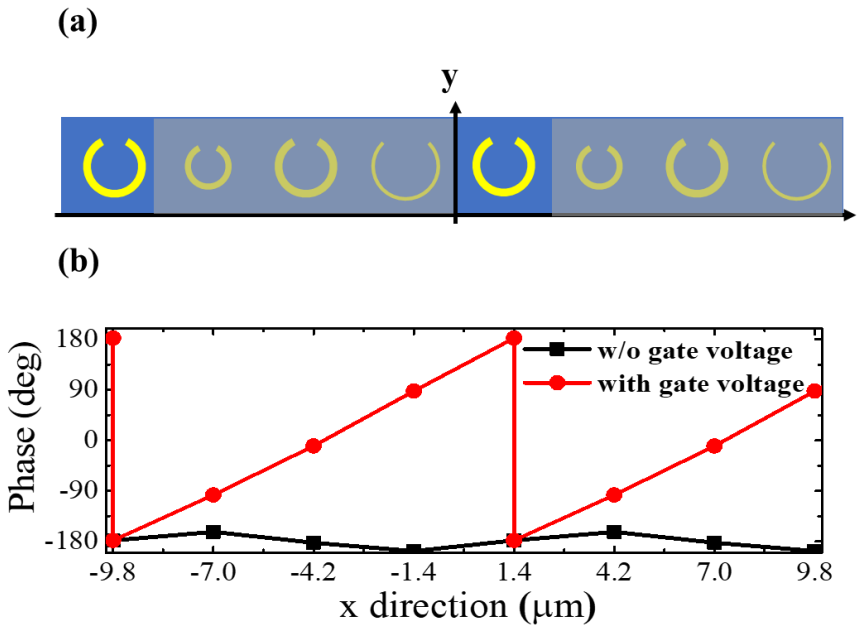

Figure 8.10 (a) Schematic of two adjacent super cells of beam steering lens constructed by four modulators with different geometric parameters to achieve the necessary reflection phases. (b) The phase profile along x-axis at f = 60 THz for non-doped and doped graphene devices shown in (a).

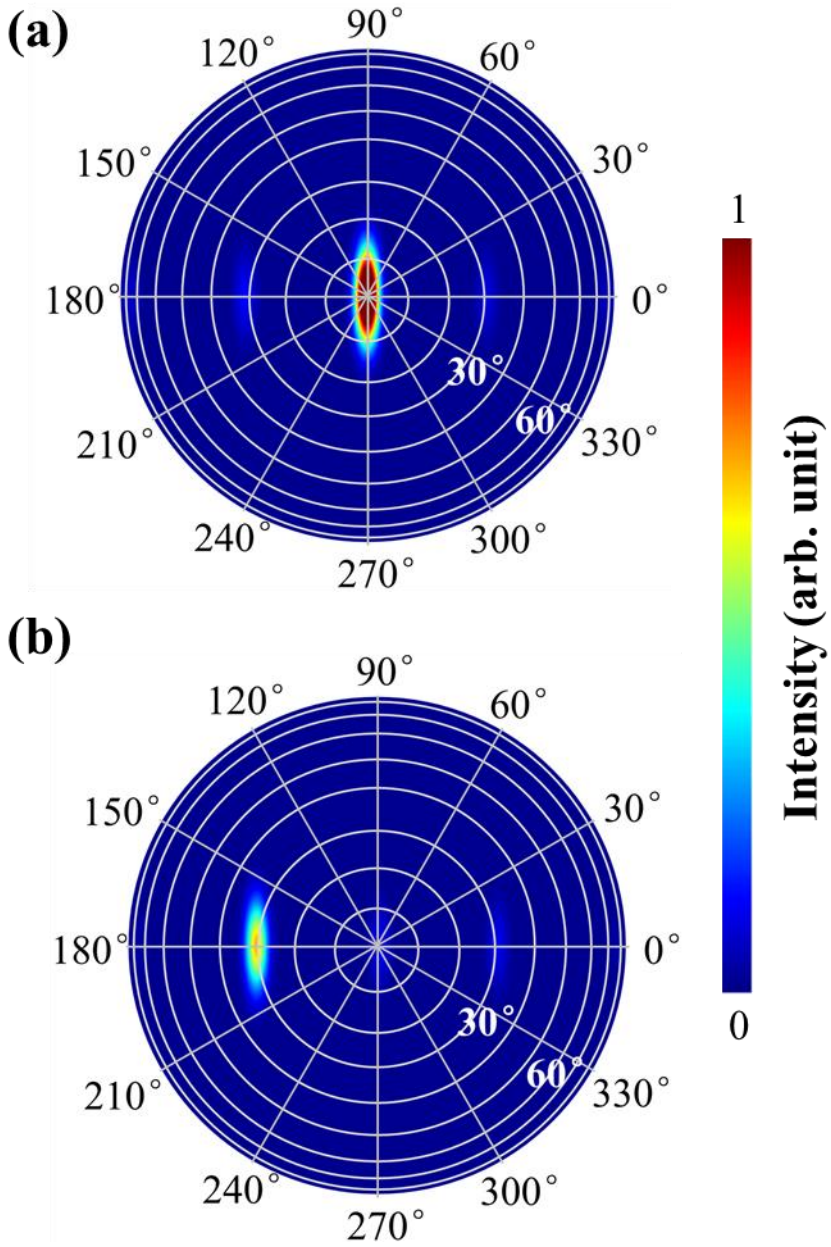

Figure 8.11 Numerical simulations of scattering farfield pattern of non-doped graphene (a) and doped graphene device (b), showing specular and anomalous reflection at f = 60 THz respectively.

8.5 Summary

In this chapter, it is shown that the electromagnetic response of the metasurface design can be manipulated via applying voltage on it by integrating monolayer graphene into it. The variation in the conductivity of graphene caused by tuning the gate voltage applied to it will change the effective impedance of the graphene integrated metasurface design and thus shift its reflection spectrum. The design proposed in this chapter, a graphene-integrated SRR Salisbury screen, is able to achieve a good tunability by enhancing the nonlinear response of graphene via localizing the electric field on it. Numerical simulations show that due to the strong confinement at the split gap of SRR, the design is able to achieve a 50% modulation width in reflectance and 150° in reflection phase when the Fermi level of graphene is altered from 0eV to 0.4eV accordingly. The fabricated modulator was then tested in an FTIR reflection setup, although only a 0.288eV Fermi level can be achieved, it is still observed that the resonant frequency at which the minimum in reflection occurs can be directly controlled by an applied bias, with the size of the shift being in good agreement with the simulations. We also demonstrate the feasibility of creating a beam steering lens by constructing four such modulators but with different geometric parameters as a new super cell. Simulations show that, as

a 0 to 2π phase variation over the super cell will be established as soon as the Fermi level of graphene is increased to 0.4 eV, the metasurface lens will reflect the beam with an extra 30° compared to when the graphene is undoped.

9 Conclusions and Outlook

The work presented in this thesis focuses on the development of a series of new generation mid-infrared devices which are compact in size and powerful in performance. Three different devices, narrowband mid-infrared thermal emitter, wave trapping sensor, and phase modulators were designed exploiting the unique properties of the two ultrathin building blocks: metasurface and graphene. Preliminary prototypes were fabricated in a cleanroom using modern semiconductor fabrication technology like RIE etching, e-beam lithography, and thermal evaporation. Results measured under different setups based on FTIR spectroscopy showed good agreement with simulation results.

However, it should be noted that there is still room to improve the performance of the devices described in Chapter 6,7,8. Some of the latest work on metasurface design and graphene synthesis, which could benefit our devices are highlighted in Section 9.2.

9.1 Conclusions

9.1.1 Metasurface-based Narrowband Graphene Thermal Emitter

A metasurface, composed of two groups of metallic annular rings in diagonal and off-diagonal directions, was designed as a frequency selective surface and integrated into the graphene thermal emitter for reducing the emission bandwidth. Simulation, as well as experiment results, show that the broadband emission from the Joule heating of the graphene filament is tailored into two narrow windows, which directly related to the resonance frequencies of both groups of annular ring resonators. The resonance of annual rings will constructively interferes with the thermal radiation from the graphene filament, leading to maxima in the emission spectra at wavelengths determined by their geometry. Simulations also show that the addition of a conducting layer below the emitting layer greatly increases the Q-factor of the maximum in the emission spectrum.

The possibility of tailoring the emission characteristics of these devices, which can reduce manufacturing costs and allow for modulation

at relatively high frequencies, demonstrates their potential for use in applications such as infrared gas sensing.

9.1.2 Metasurface-enhanced ATR Spectroscopy

In this work, a metasurface was designed to localize and enhance the field distribution in a small area for increasing the sensitivity of detecting chemical or other biological samples in an aqueous environment. Resonant features were observed corresponding to the resonance of the metasurface on the silicon substrate device, and the hybrid resonance of phonon modes and metasurface resonance on the SiO_2/Si substrate. Field distribution profiles obtained from the simulation results suggests the strong localized field enhancement in the nano gap at the centre of the complimentary ring resonators, where the light-matter interactions are strengthened. Preliminary experiments were undertaken in an FTIR-ATR system using mixtures of butyl acetate diluted with oleic acid. Without the use of a metasurface, the minimum concentration of butyl acetate that could be detected was 10%, whereas the use of the metasurface on the SiO_2/Si substrate allowed the detection of 1%, due to the coupling of the vibrational resonances of the butyl acetate with the hybridised metamaterial phonon mode.

These results demonstrate the potential of the use of metamaterials to improve the sensitivity of FTIR-ATR measurements, and offers a new route for improved trace chemical detection.

9.1.3 Graphene based metasurface phase modulator

Graphene is used in conjunction with metasurface to achieve a dynamic control on the response of the mid-infrared wave. A mid-infrared reflective modulator was achieved by split-ring resonator and CVD graphene. When a gate voltage is applied, the Fermi level of graphene is shifted leading to a change of its conductivity, which will consequently change the effective impedance at the interface. Simulations show that the device can achieve a phase modulation up to 150° when the Fermi level increases from 0eV to 0.4eV. Based on the design of modulator, we also demonstrate the feasibility of creating a beam steering lens by constructing four such modulators but with different geometric parameters as a new super lattice. Simulations show that, as 0 to 2π phase variation over the unit cell will be established as soon as a gate voltage is applied, the gated lens will reflect the beam with an extra 30° compared to when the lens is unbiased.

The compact and ultrafast modulators we proposed could promote a wide range of mid-infrared application in free-space communications, imaging, LIDAR, and homeland security, etc

9.2 Outlook

9.2.1 Metasurface

Due to the limited choices of fabrication equipment, the metasurface proposed in this work is all made of gold, which suffers from drawbacks such as low Q-factor as a result of high Ohmic losses. However, it has been proved in previous research that strong and high Q-factor resonance is achievable by using metasurface made of dielectrics with high permittivity, which can generate magnetic dipoles, electric dipoles and higher order dipoles due to Mie resonances [255]. This could potentially improve the performance of our metasurface-based graphene thermal emitter.

9.2.2 Graphene

The area of graphene has become a cutting-edge and promising researching direction in recent years, but there is still a very long way to

go for the mass production of graphene devices. Although CVD graphene can now be probed in a very large area, surface impurities introduced during the synthesis process will introduce detrimental impacts upon the intrinsic properties of graphene and thus device performances. The exfoliation method, on the other hand, can provide better quality graphene with higher purity and superior electrical and thermal performance, but is not ideal for large-scale monolayer graphene synthesis. Progress has been made on the research on the synthesis method of large-area, high quality monolayer graphene sheet. Zhang et al from Berkley, have recently reported their experiments of dewetting the catalytic metal during the CVD process [256]. In this case, the graphene will be directly attached to the dielectric layer which may eliminate impurities produced from CVD and transfer.

Bibliography

1 Krier, A. *Mid-infrared semiconductor optoelectronics*. Springer (2007).

2 Smith, B. C. *Fundamentals of Fourier transform infrared spectroscopy*. CRC Press (2011).

3 Elder, T., & Strong, J. The infrared transmission of atmospheric windows. *Journal of The Franklin Institute* **255**, 189-208 (1953).

4 Karoui, R., Downey, G. & Blecker, C. Mid-infrared spectroscopy coupled with chemometrics: A tool for the analysis of intact food systems and the exploration of their molecular structure-quality relationships-A review. *Chemical Reviews* **110**, 6144–6168 (2010).

5 Schliesser, A., Picqué, N. & Hänsch, T. W. Mid-infrared frequency combs. *Nature Photonics* **6**, 440–449 (2012).

6 Aroca, R. F., Ross, D. J. & Domingo, C. Surface-enhanced infrared spectroscopy. *Applied Spectroscopy* **58**, (2004).

7 Stuart, B. H. *Infrared Spectroscopy: Fundamentals and Applications*. John Wiley & Sons (2004).

8 Özcan, L. Ç., Tréanton, V., Kashyap, R. & Martinu, L. High-quality flat-top micromachining of silica by a CW CO2 laser. *IEEE Photonics Technology Letters* **19**, 459–461 (2007).

9 Lin, P. T. *et al*. Mid-infrared spectrometer using opto-nanofluidic slot-waveguide for label-free on-chip chemical sensing. *Nano Letters* **14**, 231–238 (2014).

10 Wysocki, G. & Weidmann, D. Molecular dispersion spectroscopy for chemical sensing using chirped mid-infrared quantum cascade laser. *Optics Express* **18**, 26123–26140 (2010).

11 Soref, R. Mid-infrared photonics in silicon and germanium. *Nat. Photonics*, **4**, 495 (2010).

12 Law, S., Podolskiy, V., & Wasserman, D. Towards nano-scale photonics with micro-scale photons: the opportunities and challenges of mid-infrared plasmonics. *Nanophotonics* **2**, 103-130 (2013).

13 Santos, P. M., Pereira-Filho, E. R., & Rodriguez-Saona, L. E. Application of hand-held and portable infrared spectrometers in bovine milk analysis. *Journal of Agricultural and Food Chemistry* **61**, 1205-1211 (2013).

14 Lin, C. A., Ayvaz, H., & Rodriguez-Saona, L. E. Application of portable and handheld infrared spectrometers for determination of sucrose levels in infant cereals. *Food Analytical Methods* **7**, 1407-1414 (2014).

15 Birkel, E., & Rodriguez-Saona, L. Application of a portable handheld infrared spectrometer for quantitation of trans fat in edible oils. *Journal of the American Oil Chemists' Society* **88**, 1477-1483 (2011).

16 Wright, A. F., & Dupuy, J. *Glass... current issues*. Springer Science & Business Media (2012).

17 Soref, R. Mid-infrared photonics in silicon and germanium. *Nature Photonics*, **4**, 495 (2010).

18 Harris, D. C. *Materials for infrared windows and domes: properties and performance*. SPIE Press (1999).

19 Mahlmeister, N. H., Lawton, L. M., Luxmoore, I. J., & Nash, G. R. Modulation characteristics of graphene-based thermal emitters. *Applied Physics Express* **9**, 012105 (2015).

20 Shi, C., Mahlmeister, N.H., Luxmoore, I.J. and Nash, G.R., Metamaterial-based graphene thermal emitter. *Nano Research* **11**, 3567-3573 (2018).

21 Shi, C., Penrose, C., Pitts, J. E., Gowda, P., Luxmoore, I. J., & Nash, G. R. Metamaterial-enhanced infrared attenuated total reflection spectroscopy. *Nanoscale Advances*, **1**, 476-480 (2019).

22 Shi, C., Luxmoore, I. J., & Nash, G. R. Graphene-based Metamaterial Tunable Phase Modulator for Mid-Infrared Wave Steering. In *CLEO2019* JTh2A-26 (2019).

23 Shi, C., Luxmoore, I. J., & Nash, G. R. Gate tunable graphene-integrated metasurface modulator for mid-infrared beam steering. *Optics Express* **27**, 14577-14584 (2019).

24 Qu, S., Ma, C., Wang, S., Liu, H., & Dong, L. Modulation speed limits of a graphene-based modulator. *Optical and Quantum Electronics* **50**, 105 (2018).

25 Atkins, P., & De Paula, J. *Physical Chemistry.* Macmillan Higher Education (2009).

26 Silverstein, R. M., Webster, F. X., Kiemle, D. J., & Bryce, D. L. *Spectrometric identification of organic compounds*. John Wiley & Sons (2014).

27 Theophanides, T. *Introduction to Infrared Spectroscopy. Infrared Spectroscopy - Materials Science, Engineering and Technology.* Intechopen (2012).

28 Allen, M. G. Diode laser absorption sensors for gas-dynamic and combustion flows. *Measurement Science and Technology* **9**, 545–562 (1998).

29 Muda, R., Lewis, E., O'Keeffe, S., Dooly, G. & Clifford, J. A compact optical fibre based mid- infrared sensor system for detection of high level carbon dioxide emissions in exhaust automotive applications. *Procedia Chemistry* **1**, 593–596 (2009).

30 Pejcic, B., Myers, M. & Ross, A. Mid-infrared sensing of organic pollutants in aqueous environments. *Sensors* **9**, 6232–6253 (2009).

31 Zhang, Y. *et al.* Design of a novel gas sensor structure based on mid-infrared absorption spectrum. *Sensors and Actuators B: Chemical* **147**, 5–9 (2010).

32 Töpfer, T. *et al.* Room-temperature mid-infrared laser sensor for trace gas detection. *Applied Optics* **36**, 8042–8049 (1997).

33 Werle, P. *et al*. Near- and mid-infrared laser-optical sensors for gas analysis. *Optics and Lasers in Engineering* **37**, 101–114 (2002).

34 Iseki, T., Tai, H. & Kimura, K. A portable remote methane sensor using a tunable diode laser. *Measurement Science and Technology* **11**, 594–602 (2000).

35 Yasuda, T., Yonemura, S. & Tani, A. Comparison of the characteristics of small commercial NDIR CO_2 sensor models and development of a portable CO_2 measurement device. *Sensors* **12**, 3641–3655 (2012).

36 Wilson, R. H. & Tapp, H. S. Mid-infrared spectroscopy for food analysis: Recent new applications and relevant developments in sample presentation methods. *TrAC Trends in Analytical Chemistry* **18**, 85–93 (1999).

37 Barth, A. Infrared spectroscopy of proteins. *Biochimica et Biophysica Acta-Bioenergetics.* **1767**, 1073–1101 (2007).

38 Seddon, A. B. A Prospective for new mid-Infrared medical endoscopy using chalcogenide glasses. *International Journal of Applied Glass Science* **2**, 177–191 (2011).

39 Lloyd, J. M. *Thermal imaging systems*. Springer Science & Business Media (2013).

40 Vollmer, M., & Möllmann, K. P. *Infrared thermal imaging: fundamentals, research and applications.* John Wiley & Sons. (2017).

41 Walther, M., 256× 256 focal plane array mid-wavelength infrared camera based on InAs/GaSb short-period superlattices. *Journal of Electronic Materials* **34**, 722-725 (2005).

42 http://lasp.colorado.edu/~bagenal/3720/CLASS5/5Spectroscopy.html

43 Clayden, J. J., Greeves, N., Warren, S. & Wothers, P. *Organic Chemistry*. Oxford University Press (2001).

44 Hester, R. E. & Girling, R. B. *Spectroscopy of Biological Molecules.* Royal Society of Chemistry (1991).

45 Socrates, G. *Infrared and Raman characteristic group frequencies: tables and charts*. John Wiley & Sons (2004).

46 Silverstein, R. M., Bassler, G. C., & Morrill, T. C. *Spectrometric Identification of Organic Compounds. 4th Edn.*, John Wiley and Sons (1981).

47 Stiff-Roberts, A. D., Chakrabarti, S., Pradhan, S., Kochman, B., & Bhattacharya, P. Raster-scan imaging with normal-incidence, midinfrared InAs/GaAs quantum dot infrared photodetectors. *Applied Physics Letters* **80**, 3265-3267 (2002).

48 Tsuji, T., Hattori, H., Watanabe, M., & Nagaoka, N. Development of night-vision system. *IEEE Transactions on Intelligent Transportation Systems* **3**, 203-209 (2002).

49 Starr, J. W., & Lattimer, B. Y. Evaluation of navigation sensors in fire smoke environments. *Fire Technology* **50**, 1459-1481 (2014).

50 Wong, W. K., Tan, P. N., Loo, C. K., & Lim, W. S. An effective surveillance system using thermal camera. *International Conference on Signal Acquisition and Processing In 2009,* 13-17 (2009).

51 Allison, R., Johnston, J., Craig, G., & Jennings, S. Airborne optical and thermal remote sensing for wildfire detection and monitoring. *Sensors* **16**, 1310 (2016).

52 Francisco, G. L. Amorphous silicon bolometer for fire/rescue. In Thermosense XXIII. *International Society for Optics and Photonics* **4360**, 138-148 (2001).

53 Yu, B., Qi, L., Ye, J. Z., & Sun, H. Preparation and radar wave absorbing characterization of bicomponent fibers with infrared camouflage. *Journal of Applied Polymer Science* **104**, 2180-2186 (2007).

54 Liu, X. F., Lai, Y. K., Huang, J. Y., Al-Deyab, S. S., & Zhang, K. Q. Hierarchical SiO2@ Bi2O3 core/shell electrospun fibers for infrared stealth camouflage. *Journal of Materials Chemistry C* **3**, 345-351 (2015).

55 Salihoglu, O. *et al.* Graphene-based adaptive thermal camouflage. *Nano Letters* **18**, 4541-4548 (2018).

56 Phan, L., Walkup IV, W. G., Ordinario, D. D., Karshalev, E., Jocson, J. M., Burke, A. M., & Gorodetsky, A. A. Reconfigurable infrared camouflage coatings from a cephalopod protein. *Advanced Materials* **25**, 5621-5625 (2013).

57 Schurig, D., Mock, J. J., Justice, B. J., Cummer, S. A., Pendry, J. B., Starr, A. F., & Smith, D. R. Metamaterial electromagnetic cloak at microwave frequencies. *Science* **314**, 977-980 (2006).

58 Landy, N., & Smith, D. R. A full-parameter unidirectional metamaterial cloak for microwaves. *Nature Materials* **12**, 25 (2013).

59 Ma, H. F., & Cui, T. J. Three-dimensional broadband ground-plane cloak made of metamaterials. *Nature Communications* **1**, 21 (2010).

60 Zang, X., Shi, C., Li, Z., Chen, L., Cai, B., Zhu, Y., & Zhu, H. Illusion induced overlapped optics. *Optics Express* **22**, 582-592 (2014).

61 Jiang, W. X., Qiu, C. W., Han, T., Zhang, S., & Cui, T. J. Creation of ghost illusions using wave dynamics in metamaterials. *Advanced Functional Materials* **23**, 4028-4034 (2013).

62 Smith, D. R., Vier, D. C., Koschny, T., & Soukoulis, C. M. Electromagnetic parameter retrieval from inhomogeneous metamaterials. *Physical Review E* **71**, 036617 (2005).

63 Smith, D. R., Schultz, S., Markoš, P., & Soukoulis, C. M. Determination of effective permittivity and permeability of metamaterials from reflection and transmission coefficients. *Physical Review B* **65**, 195104 (2002).

64 Liu, R., Cui, T. J., Huang, D., Zhao, B., & Smith, D. R. Description and explanation of electromagnetic behaviors in artificial metamaterials based on effective medium theory. *Physical Review E* **76**, 026606 (2007).

65 Simovski, C. R., & Tretyakov, S. A. Local constitutive parameters of metamaterials from an effective-medium perspective. *Physical Review B* **75**, 195111 (2007).

66 Schurig, D., Mock, J. J., & Smith, D. R. Electric-field-coupled resonators for negative permittivity metamaterials. *Applied Physics Letters* **88**, 041109 (2006).

67 Zhao, Q. *et al.* Electrically tunable negative permeability metamaterials based on nematic liquid crystals. *Applied Physics Letters* **90**, 011112 (2007).

68 Shalaev, V. M. Optical negative-index metamaterials. *Nature Photonics* **1**, 41 (2007).

69 Smith, D. R., Pendry, J. B., & Wiltshire, M. C. Metamaterials and negative refractive index. *Science* **305**, 788-792 (2004).

70 Landy, N. I., Sajuyigbe, S., Mock, J. J., Smith, D. R., & Padilla, W. J. Perfect metamaterial absorber. *Physical Review Letters* **100**, 207402 (2008).

71 Tao, H., Landy, N. I., Bingham, C. M., Zhang, X., Averitt, R. D., & Padilla, W. J. A metamaterial absorber for the terahertz regime: design, fabrication and characterization. *Optics Express* **16**, 7181-7188. (2008).

72 Hokmabadi, M. P., Wilbert, D. S., Kung, P., & Kim, S. M. Terahertz metamaterial absorbers. *Terahertz Science and Technology* **6**, 40-58. (2013).

73 Wang, B. X., Wang, L. L., Wang, G. Z., Huang, W. Q., Li, X. F., & Zhai, X. A simple design of ultra-broadband and polarization insensitive terahertz metamaterial absorber. *Applied Physics A* **115**, 1187-1192 (2014).

74 Ye, Y. Q., Jin, Y., & He, S. Omnidirectional, polarization-insensitive and broadband thin absorber in the terahertz regime. *JOSA B* **27**, 498-504 (2010).

75 Cui, Y., Fung, K. H., Xu, J., Ma, H., Jin, Y., He, S., & Fang, N. X. Ultrabroadband light absorption by a sawtooth anisotropic metamaterial slab. *Nano Letters* **12**, 1443-1447 (2012).

76 Grant, J., Ma, Y., Saha, S., Khalid, A., & Cumming, D. R. Polarization insensitive, broadband terahertz metamaterial absorber. *Optics Letters* **36**, 3476-3478 (2011).

77 Shi, C., Zang, X., Wang, Y., Chen, L., Cai, B., & Zhu, Y. A polarization-independent broadband terahertz absorber. *Applied Physics Letters* **105**, 031104 (2014).

78 Pu, M., Wang, M., Hu, C., Huang, C., Zhao, Z., Wang, Y., & Luo, X. Engineering heavily doped silicon for broadband absorber in the terahertz regime. *Optics Express* **20**, 25513-25519 (2012).

79 Zang, X., Shi, C., Chen, L., Cai, B., Zhu, Y., & Zhuang, S. Ultra-broadband terahertz absorption by exciting the orthogonal diffraction in dumbbell-shaped gratings. *Scientific Reports* **5**, 8901 (2015).

80 Shi, C., Zang, X. F., Chen, L., Peng, Y., Cai, B., Nash, G. R., & Zhu, Y. M. Compact broadband terahertz perfect absorber based on multi-interference and diffraction effects. *IEEE Transactions on Terahertz Science and Technology* **6**, 40-44. (2015).

81 Shen, X., Yang, Y., Zang, Y., Gu, J., Han, J., Zhang, W., & Jun Cui, T. (2012). Triple-band terahertz metamaterial absorber: Design, experiment, and physical interpretation. Applied Physics Letters, 101(15), 154102.

82 Ma, Y., Chen, Q., Grant, J., Saha, S. C., Khalid, A., & Cumming, D. R. A terahertz polarization insensitive dual band metamaterial absorber. *Optics Letters* **36**, 945-947 (2011).

83 Lu, D., & Liu, Z. Hyperlenses and metalenses for far-field super-resolution imaging. *Nature Communications* **3**, 1205 (2012).

84 Aydin, K., Bulu, I., & Ozbay, E. Subwavelength resolution with a negative-index metamaterial superlens. *Applied Physics Letters* **90**, 254102 (2007).

85 Zhang, X., & Liu, Z. Superlenses to overcome the diffraction limit. *Nature Materials* **7**, 435 (2008).

86 Liu, Zhaowei. *et al*. Far-field optical superlens. *Nano Letters* **7** 403-408 (2007).

87 Casse, B. D. F., Lu, W. T., Huang, Y. J., Gultepe, E., Menon, L., & Sridhar, S. Super-resolution imaging using a three-dimensional metamaterials nanolens. *Applied Physics Letters* **96**, 023114 (2010).

88 Ma, C., & Liu, Z. A super resolution metalens with phase compensation mechanism. *Applied Physics Letters* **96**, 183103 (2010).

89 Ma, C., & Liu, Z. Focusing light into deep subwavelength using metamaterial immersion lenses. *Optics Express* **18**, 4838-4844 (2010).

90 Chen, H., Chan, C. T., & Sheng, P. Transformation optics and metamaterials. *Nature Materials* **9**, 387 (2010).

91 Ergin, T., Stenger, N., Brenner, P., Pendry, J. B., & Wegener, M. Three-dimensional invisibility cloak at optical wavelengths. *Science* **328**, 337-339 (2010).

92 Lheurette, E. *Metamaterials and Wave Control*. Wiley-ISTE (2013).

93 Chen, H. T., Taylor, A. J., & Yu, N. A review of metasurfaces: physics and applications. *Reports on Progress in Physics* **79**, 076401 (2016).

94 Yu, N., & Capasso, F. Flat optics with designer metasurfaces. *Nature Materials* **13**, 139 (2014).

95 Zhang, L., Mei, S., Huang, K., & Qiu, C. W. Advances in full control of electromagnetic waves with metasurfaces. *Advanced Optical Materials* **4**, 818-833 (2016).

96 Holloway, C. L., Kuester, E. F., Gordon, J. A., O'Hara, J., Booth, J., & Smith, D. R. An overview of the theory and applications of metasurfaces: The two-dimensional equivalents of metamaterials. *IEEE Antennas and Propagation Magazine* **54**, 10-35 (2012).

97 Yu, N., Genevet, P., Kats, M. A., Aieta, F., Tetienne, J. P., Capasso, F., & Gaburro, Z. Light propagation with phase discontinuities: generalized laws of reflection and refraction. *Science* **334**, 333-337 (2011).

98 Huang, L. *et al*. Dispersionless phase discontinuities for controlling light propagation. *Nano Letters* **12**, 5750-5755 (2012).

99 Ding, X. *et al*. Ultrathin Pancharatnam–Berry metasurface with maximal cross-polarization efficiency. *Advanced Materials* **27**, 1195-1200 (2015).

100 Ni, X., Emani, N. K., Kildishev, A. V., Boltasseva, A., & Shalaev, V. M. Broadband light bending with plasmonic nanoantennas. *Science* **335**, 427-427 (2012).

101 Sun, S. *et al*. High-efficiency broadband anomalous reflection by gradient meta-surfaces. *Nano Letters* **12**, 6223-6229 (2012).

102 Aieta, F., Genevet, P., Kats, M. A., Yu, N., Blanchard, R., Gaburro, Z., & Capasso, F. Aberration-free ultrathin flat lenses and axicons at telecom wavelengths based on plasmonic metasurfaces. *Nano Letters* **12**, 4932-4936 (2012).

103 Pors, A., Nielsen, M. G., Eriksen, R. L., & Bozhevolnyi, S. I. Broadband focusing flat mirrors based on plasmonic gradient metasurfaces. *Nano Letters* **13**, 829-834 (2013).

104 Ni, X., Kildishev, A. V., & Shalaev, V. M. Metasurface holograms for visible light. *Nature Communications* **4**, 2807 (2013).

105 Huang, L., Chen, X., Mühlenbernd, H., Zhang, H., Chen, S., Bai, B., ... & Li, J. Three-dimensional optical holography using a plasmonic metasurface. *Nature Communications* **4**, 2808 (2013).

106 Zheng, G., Mühlenbernd, H., Kenney, M., Li, G., Zentgraf, T., & Zhang, S. Metasurface holograms reaching 80% efficiency. *Nature Nanotechnology* **10**, 308 (2015).

107 Li, A., Forati, E., & Sievenpiper, D. Study of the electric field enhancement in resonant metasurfaces. *Journal of Optics* **19**, 125104 (2017).

108 Singh, R., Cao, W., Al-Naib, I., Cong, L., Withayachumnankul, W., & Zhang, W. Ultrasensitive terahertz sensing with high-Q Fano resonances in metasurfaces. *Applied Physics Letters* **105**, 171101 (2014).

109 Novotny, L., Sánchez, E. J., & Xie, X. S. Near-field optical imaging using metal tips illuminated by higher-order Hermite–Gaussian beams. *Ultramicroscopy* **71**, 21-29 (1998).

110 Liu, N., Mesch, M., Weiss, T., Hentschel, M., & Giessen, H. Infrared perfect absorber and its application as plasmonic sensor. *Nano Letters* **10**, 2342-2348 (2010).

111 Atwater, H. A., & Polman, A. Plasmonics for improved photovoltaic devices. *Nature Materials* **9**, 205-213 (2010).

112 Sun, Q., Ueno, K., Yu, H., Kubo, A., Matsuo, Y., & Misawa, H. Direct imaging of the near field and dynamics of surface plasmon resonance on gold nanostructures using photoemission electron microscopy. *Light: Science & Applications* **2**, 118. (2013).

113 Dombi, P., Hörl, A., Rácz, P., Márton, I., Trügler, A., Krenn, J. R., & Hohenester, U. Ultrafast strong-field photoemission from plasmonic nanoparticles. *Nano Letters* **13**, 674-678 (2013).

114 Markoš, P., & Soukoulis, C. M. Numerical studies of left-handed materials and arrays of split ring resonators. *Physical Review E* **65**, 036622 (2002).

115 Wang, H., Sivan, V. P., Mitchell, A., Rosengarten, G., Phelan, P., & Wang, L. Highly efficient selective metamaterial absorber for high-temperature solar thermal energy harvesting. *Solar Energy Materials and Solar Cells* **137**, 235-242 (2015).

116 Mulla, B., & Sabah, C. Multiband metamaterial absorber design based on plasmonic resonances for solar energy harvesting. *Plasmonics* **11**, 1313-1321 (2016).

117 Zhang, Y. *et al*. Broadband diffuse terahertz wave scattering by flexible metasurface with randomized phase distribution. *Scientific Reports* **6**, 26875 (2016).

118 Liu, N., Mesch, M., Weiss, T., Hentschel, M., & Giessen, H. Infrared perfect absorber and its application as plasmonic sensor. *Nano Letters* **10**, 2342-2348 (2010).

119 Hecht, E. *Optics 2nd edition*. MA: Addison-Wesley Publishing Company (1987).

120 Zhu, W., Xiao, F., Kang, M., & Premaratne, M. Coherent perfect absorption in an all-dielectric metasurface. *Applied Physics Letters* **108**, 121901 (2016).

121 Feng, S., & Halterman, K. Coherent perfect absorption in epsilon-near-zero metamaterials. *Physical Review B* **86**, 165103 (2012).

122 Shrekenhamer, D., Chen, W. C., & Padilla, W. J. Liquid crystal tunable metamaterial absorber. *Physical Review Letters* **110**, 177403 (2013).

123 Zhao, J., Cheng, Q., Chen, J., Qi, M. Q., Jiang, W. X., & Cui, T. J. A tunable metamaterial absorber using varactor diodes. *New Journal of Physics* **15**, 043049 (2013).

124 Zhang, Y., Feng, Y., Zhu, B., Zhao, J., & Jiang, T. Graphene based tunable metamaterial absorber and polarization modulation in terahertz frequency. *Optics Express* **22**, 22743-22752 (2014).

125 Yu, N., Aieta, F., Genevet, P., Kats, M. A., Gaburro, Z., & Capasso, F. A broadband, background-free quarter-wave plate based on plasmonic metasurfaces. *Nano Letters* **12**, 6328-6333 (2012).

126 Decker, M*. et al*. High-efficiency dielectric Huygens' surfaces. *Advanced Optical Materials* **3**, 813-820 (2015).

127 Kim, M., Wong, A. M., & Eleftheriades, G. V. Optical Huygens' metasurfaces with independent control of the magnitude and phase of the local reflection coefficients. *Physical Review X* **4**, 041042 (2014).

128 Monticone, F., Estakhri, N. M., & Alù, A. Full control of nanoscale optical transmission with a composite metascreen. *Physical Review Letters* **110**, 203903 (2013).

129 Qin, F. *et al.* Hybrid bilayer plasmonic metasurface efficiently manipulates visible light. *Science Advances* **2,** e1501168 (2016).

130 de Galarreta, C. R. *et al*. Nonvolatile Reconfigurable Phase-Change Metadevices for Beam Steering in the Near Infrared. *Advanced Functional Materials* **28**, 1704993 (2018).

131 Gholipour, B., Zhang, J., MacDonald, K. F., Hewak, D. W., & Zheludev, N. I. An all-optical, non-volatile, bidirectional, phase-change meta-switch. *Advanced Materials* **25**, 3050-3054 (2013).

132 Chen, H. T., Padilla, W. J., Zide, J. M., Gossard, A. C., Taylor, A. J., & Averitt, R. D. Active terahertz metamaterial devices. *Nature* **444**, 597 (2006).

133 Liu, M. *et al*. A graphene-based broadband optical modulator. *Nature* **474**, 64 (2011).

134 Manjappa, M., Pitchappa, P., Singh, N., Wang, N., Zheludev, N. I., Lee, C., & Singh, R. Reconfigurable MEMS Fano metasurfaces with multiple-input–output states for logic operations at terahertz frequencies. *Nature Communications* **9**, 4056 (2018).

135 Goldflam, M. D. *et al*. Reconfigurable gradient index using VO_2 memory metamaterials. *Applied Physics Letters* **99**, 044103 (2011).

136 Balandin, A. A., Ghosh, S., Bao, W., Calizo, I., Teweldebrhan, D., Miao, F., & Lau, C. N. Superior thermal conductivity of single-layer graphene *Nano Letters* **8**, 902-907 (2008).

137 Pop, E., Varshney, V., & Roy, A. K. Thermal properties of graphene: Fundamentals and applications. *MRS Bulletin* **37**, 1273-1281 (2012).

138 Shahil, K. M., & Balandin, A. A. Thermal properties of graphene and multilayer graphene: Applications in thermal interface materials. *Solid State Communications* **152**, 1331-1340 (2012).

139 Lee, C., Wei, X., Kysar, J. W., & Hone, J. Measurement of the elastic properties and intrinsic strength of monolayer graphene. *Science* **321**, 385-388 (2008).

140 Frank, I. W., Tanenbaum, D. M., van der Zande, A. M., & McEuen, P. L. Mechanical properties of suspended graphene sheets. *Journal of Vacuum Science & Technology B: Microelectronics and Nanometer Structures Processing, Measurement, and Phenomena* **25**, 2558-2561 (2007).

141 Novoselov, K. S. *et al.* Electric field effect in atomically thin carbon films. *Science* **306**, 666-669 (2004).

142 Novoselov, K. S. *et al.* Two-dimensional gas of massless Dirac fermions in graphene. *Nature* **438**, 197 (2005).

143 Neto, A. C., Guinea, F., Peres, N. M., Novoselov, K. S., & Geim, A. K. The electronic properties of graphene. *Reviews of Modern Physics* **81**, 109 (2009).

144 Semenoff, G. W. Condensed-matter simulation of a three-dimensional anomaly. *Physical Review Letters* **53**, 2449 (1984).

145 Dirac, P.A.M. *Principles of Quantum Mechanics. International Series of Monographs on Physics (4th ed.)*. Oxford University Press (1982)

146 Zhang, Y., Tan, Y. W., Stormer, H. L., & Kim, P. Experimental observation of the quantum Hall effect and Berry's phase in graphene. *Nature* **438**, 201 (2005).

147 Novoselov, K. S. *et al*. Room-temperature quantum Hall effect in graphene. *Science* **315**, 1379-1379 (2007).

148 Young, A. F., & Kim, P. Quantum interference and Klein tunnelling in graphene heterojunctions. *Nature Physics* **5**, 222 (2009).

149 Katsnelson, M. I., Novoselov, K. S., & Geim, A. K. Chiral tunnelling and the Klein paradox in graphene. *Nature Physics* **2**, 620 (2006).

150 Cheianov, V. V., Fal'ko, V., & Altshuler, B. L. The focusing of electron flow and a Veselago lens in graphene pn junctions. *Science* **315**, 1252-1255 (2007).

151 Liu, H., Liu, Y., & Zhu, D. Chemical doping of graphene. *Journal of Materials Chemistry* **21**, 3335-3345 (2011).

152 Fang, T., Konar, A., Xing, H., & Jena, D. Carrier statistics and quantum capacitance of graphene sheets and ribbons. *Applied Physics Letters* **91**, 092109 (2007).

153 Das, A. *et al.* Monitoring dopants by Raman scattering in an electrochemically top-gated graphene transistor. *Nature Nanotechnology* **3**, 210 (2008).

154 Ju, L. *et al*. Graphene plasmonics for tunable terahertz metamaterials. *Nature Nanotechnology* **6**, 630 (2011).

155 Chen, J. *et al*. Optical nano-imaging of gate-tunable graphene plasmons. *Nature* **487**, 77 (2012).

156 Fang, Z. *et al*. Gated tunability and hybridization of localized plasmons in nanostructured graphene. *ACS Nano* **7**, 2388-2395 (2013).

157 Liu, P. Q., Luxmoore, I. J., Mikhailov, S. A., Savostianova, N. A., Valmorra, F., Faist, J., & Nash, G. R. Highly tunable hybrid metamaterials employing split-ring resonators strongly coupled to graphene surface plasmons. *Nature Communications* **6**, 8969 (2015).

158 Luxmoore, I. J., Liu, P. Q., Li, P., Faist, J., & Nash, G. R. Graphene–metamaterial photodetectors for integrated infrared sensing. *ACS Photonics* **3**, 936-941 (2016).

159 Vakil, A. *Transformation optics using graphene: one-atom-thick optical devices based on graphene.* PhD dissertation (2012).

160 Luxmoore, I. J., Gan, C. H., Liu, P. Q., Valmorra, F., Li, P., Faist, J., & Nash, G. R. Strong coupling in the far-infrared between graphene plasmons and the surface optical phonons of silicon dioxide. *ACS Photonics* **1**, 1151-1155 (2014).

161 Geim, A. K., & Novoselov, K. S. The rise of graphene. *Nature Materials* **6,** 183-191 (2007).

162 Hanson, G. W. Dyadic Green's functions and guided surface waves for a surface conductivity model of graphene. *Journal of Applied Physics* **103**, 064302 (2008).

163 Liu, C., Bai, Y., Zhou, J., Zhao, Q., & Qiao, L. A review of graphene plasmons and its combination with metasurface. *Journal of the Korean Ceramic Society* **54**, 349-365 (2017).

164 Dayal, G., Chin, X. Y., Soci, C., & Singh, R. High-Q Plasmonic Fano Resonance for Multiband Surface-Enhanced Infrared Absorption of Molecular Vibrational Sensing. *Advanced Optical Materials* **5**, 1600559 (2017).

165 Koppens, F. H., Chang, D. E., & Garcia de Abajo, F. J. Graphene plasmonics: a platform for strong light–matter interactions. *Nano Letters* **11**, 3370-3377 (2011).

166 Rodrigo, D., Limaj, O., Janner, D., Etezadi, D., De Abajo, F. J. G., Pruneri, V., & Altug, H. Mid-infrared plasmonic biosensing with graphene. *Science* **349**, 165-168 (2015).

167 Brar, V. W., Jang, M. S., Sherrott, M., Lopez, J. J., & Atwater, H. A. Highly confined tunable mid-infrared plasmonics in graphene nanoresonators. *Nano Letters* **13**, 2541-2547 (2013).

168 Freitag, M., Low, T., Martin-Moreno, L., Zhu, W., Guinea, F., & Avouris, P. Substrate-sensitive mid-infrared photoresponse in graphene. *ACS Nano* **8**, 8350-8356 (2014).

169 Brar, V. W. *et al.* Hybrid surface-phonon-plasmon polariton modes in graphene/monolayer h-BN heterostructures. *Nano letters* **14**, 3876-3880 (2014).

170 Shi, S. F. *et al.* Optimizing broadband terahertz modulation with hybrid graphene/metasurface structures. *Nano Letters* **15**, 372-377 (2014).

171 Steinhögl, W., Schindler, G., Steinlesberger, G., Traving, M., & Engelhardt, M. Comprehensive study of the resistivity of copper wires with lateral dimensions of 100 nm and smaller. *Journal of Applied Physics* **97**, 023706 (2005).

172 Balandin, A. A., Ghosh, S., Nika, D. L., & Pokatilov, E. P. Thermal conduction in suspended graphene layers. *Fullerenes, Nanotubes, and Carbon Nanostructures* **18**, 474-486 (2010).

173 Lindsay, L., Broido, D. A., & Mingo, N. Flexural phonons and thermal transport in graphene. *Physical Review B* **82**, 115427 (2010).

174 Li, Q. Y., Xia, K., Zhang, J., Zhang, Y., Li, Q., Takahashi, K., & Zhang, X. Measurement of specific heat and thermal conductivity of supported and suspended graphene by a comprehensive Raman optothermal method. *Nanoscale* **9**, 10784-10793 (2017).

175 Barnard, H. R., Zossimova, E., Mahlmeister, N. H., Lawton, L. M., Luxmoore, I. J., & Nash, G. R. Boron nitride encapsulated graphene infrared emitters. *Applied Physics Letters* **108**, 131110 (2016).

176 Kim, Y. D. *et al*. Bright visible light emission from graphene. *Nature Nanotechnology* **10**, 676 (2015).

177 Freitag, M., Chiu, H. Y., Steiner, M., Perebeinos, V., & Avouris, P. Thermal infrared emission from biased graphene. *Nature Nanotechnology* **5**, 497 (2010).

178 Bae M-H, Islam S, Dorgan V E and Pop E. Scaling of High-Field Transport and Localized Heating in Graphene Transistors. *ACS Nano* **5**,7936–44 (2011)

179 Monk, P. *Finite element methods for Maxwell's equations.* Oxford University Press (2003).

180 Ŝolín, P. *Partial differential equations and the finite element method*. John Wiley & Sons (2005).

181 Causon, D. M., & Mingham, C. G. *Introductory finite difference methods for PDEs.* Bookboon (2010).

182 Harrington, R. F. *Field Computation by Moment Methods*. Wiley-IEEE Press (1993).

183 Weiland, T. A discretization model for the solution of Maxwell's equations for six-component fields. *Archiv Elektronik und Uebertragungstechnik* **31**, 116-120 (1977).

184 Christ, A., & Hartnagel, H. L. (1987). Three-dimensional finite-difference method for the analysis of microwave-device embedding. *IEEE Transactions on Microwave Theory and Techniques* **35**, 688-696 (1987).

185 https://en.wikipedia.org/wiki/Computational_electromagnetics

186 Courant, R. Variational methods for the solution of problems of equilibrium and vibrations. *Bulletin of the American Mathematical Society* **49**, 1-23 (1943).

187 Yee, K. Numerical solution of initial boundary value problems involving Maxwell's equations in isotropic media. *IEEE Transactions on Antennas and Propagation* **14**, 302-307 (1966).

188 https://en.wikipedia.org/wiki/Finite-difference_time-domain_method

189 https://www.agilent.com/cs/library/applications/application-refractive-index-cary-5000-uv-vis-5994-0052en-us-agilent.pdf

190 https://kb.lumerical.com/ref_sim_obj_mesh_refinement.html

191 Obraztsov, A. N. Chemical vapour deposition: making graphene on a large scale. *Nature Nanotechnology* **4**, 212 (2009).

192 Mattevi, C., Kim, H., & Chhowalla, M. A review of chemical vapour deposition of graphene on copper. *Journal of Materials Chemistry* **21**, 3324-3334 (2011).

193 Muñoz, R., & Gómez-Aleixandre, C. Review of CVD synthesis of graphene. *Chemical Vapor Deposition* **19**, 297-322 (2013).

194 Suk, J. W., *et al*. Transfer of CVD-grown monolayer graphene onto arbitrary substrates. *ACS Nano* **5**, 6916-6924 (2011).

195 Inkson, B. J. *Scanning electron microscopy (SEM) and transmission electron microscopy (TEM) for materials characterization.* In *Materials characterization using nondestructive evaluation (NDE) methods*. Woodhead Publishing (2016).

196 Eaton, P., & West, P. *Atomic force microscopy*. Oxford University Press (2010).

197 Software downloaded from http://gwyddion.net/

198 Bruker Vertex Series Brochure

199 https://www.bruker.com/products/infrared-near-infrared-and-raman-spectroscopy/ft-ir/ft-ir-accessories/platinum-atr/overview.html

200 Hildenbrand, J. *et al.* Micromachined mid-infrared emitter for fast transient temperature operation for optical gas sensing systems. *IEEE Sensors Journal* **10,** 353–362 (2010).

201 Pusch, A. *et al.* A highly efficient CMOS nanoplasmonic crystal enhanced slow-wave thermal emitter improves infrared gas-sensing devices. *Scientific. Reports* **5,** 17451 (2015).

202 Bauer, D., Heeger, M., Gebhard, M. & Benecke, W. Design and fabrication of a thermal infrared emitter. *Sensors and Actuators A: Physical* **55,** 57–63 (1996).

203 MacIsaac, D., Kanner, G. & Anderson, G. Basic physics of the incandescent lamp (lightbulb). *The Physics Teacher* **37,** 520–525 (1999).

204 Yao, Y., Hoffman, A. J. & Gmachl, C. F. Mid-infrared quantum cascade lasers. *Nature Photonics* **6,** 432–439 (2012).

205 Haigh, M. K. *et al.* Mid-infrared $Al_xIn_{1-x}Sb$ light-emitting diodes. *Applied Physics. Letters* **90,** 231116 (2007).

206 Nash, G. R. *et al.* Mid-Infrared $Al_xIn_{1-x}Sb$ Light-Emitting Diodes and Photodiodes for Hydrocarbon Sensing. *IEEE Sensors Journal.* **9,** 1240–1243 (2009).

207 Hildenbrand, J. *et al.* Fast transient temperature operating micromachined emitter for mid-infrared optical gas sensing systems: design, fabrication, characterization and optimization. *Microsystem Technologies* **16,** 745–754 (2010).

208 Ban, D. *et al*. Optimized GaAs⁄ AlGaAs light-emitting diodes and high efficiency wafer-fused optical up-conversion devices. *Journal of Applied Physics* **96**, 5243-5248 (2004).

209 Dror, B., Zheng, Y., Agrawal, M., Radhakrishnan, K., Orenstein, M., & Bahir, G. Mid-Infrared GaN/AlGaN Quantum Cascade Detector Grown on Silicon. *IEEE Electron Device Letters* **40**, 263-266 (2019).

210 Geim, A. K. Graphene: status and prospects. *Science* **324**, 1530–1534 (2009).

211 Bonaccorso, F., Sun, Z., Hasan, T. & Ferrari, A. C. Graphene Photonics and Optoelectronics. *Nature Photonics* **4**, 611–622 (2010).

212 Campos-Delgado, J. *et al.* Thermal stability studies of CVD-grown graphene nanoribbons: Defect annealing and loop formation. *Chemical Physics Letters* **469**, 177–182 (2009).

213 Dorin, B. A., & Winnie, N. Y. Two-mode division multiplexing in a silicon-on-insulator ring resonator. *Optics Express* **22**, 4547-4558 (2014).

214 Papasimakis, N., Fu, Y. H., Fedotov, V. A., Prosvirnin, S. L., Tsai, D. P., & Zheludev, N. I. Metamaterial with polarization and direction insensitive resonant transmission response mimicking electromagnetically induced transparency. *Applied Physics Letters* **94**, 211902 (2009)

215 Hsieh, L. H., & Chang, K. Equivalent lumped elements G, L, C,and unloaded Q's of closed- and open-loop ring resonators. *IEEE Transactions on Microwave Theory and Techniques* **50**, 453–460 (2002).

216 Madelung, O., Rössler, U., & Schulz, M. *Group IV Elements, IV-IV and III-V Compounds. Part a - Lattice Properties.* Springer (Berlin Heidelberg, 2001).

217 Palik, E. D. *Handbook of optical constants of solids.* Academic press (1998).

218 Robitaille, P. M. Kirchhoff's law of thermal emission: 150 years. *Progress in Physics* **4**, 3-13 (2009).

219 Yang, X., *et al*. Far-Field Spectroscopy and Near-Field Optical Imaging of Coupled Plasmon–Phonon Polaritons in 2D van der Waals Heterostructures. *Advanced Materials* **28**, 2931-2938 (2016).

220 Meier, R. *Handbook of Vibrational Spectroscopy. Chalmers, J., Griffiths, P. R., Eds.*, John Wiley & Sons Ltd. (2003).

221 Ataka, K., Kottke, T., Heberle, & J. Thinner, smaller, faster: IR techniques to probe the functionality of biological and biomimetric systems. *Angewandte Chemie International Edition* **49**, 5416–5424 (2010).

222 Haris, P. I., & Severcan, F. FTIR spectroscopic characterization of protein structure in aqueous and non-aqueous media. *Journal of Molecular Catalysis B: Enzymatic* **7**, 207-221 (1999).

223 Fahrenfort, J. Attenuated total reflection: A new principle for the production of useful infra-red reflection spectra of organic compounds. *Spectrochim Acta* **17**, 698-709 (1961).

224 Dunuwila, D. D., Carroll II, L. B., & Berglund, K.A. An investigation of the applicability of attenuated total reflection infrared spectroscopy for measurement of solubility and supersaturation of aqueous citric acid solutions. *Journal of Crystal Growth* **137**, 561-568. (1994)

225 Iwaki, M., Cotton, N. P., Quirk, P. G., Rich, P. R., & Jackson, J. B. Molecular recognition between protein and nicotinamide dinucleotide in intact, proton-translocating transhydrogenase studied by ATR-FTIR spectroscopy. *Journal of the American Chemical Society* **128**, 2621–2629 (2006).

226 Brown, L. V., *et al*. Fan-shaped gold nanoantennas above reflective substrates for surface-enhanced infrared absorption (SEIRA). *Nano Letters* **15**, 1272-1280 (2015).

227 Huck, C. *et al*. Plasmonic enhancement of infrared vibrational signals: nanoslits versus nanorods. *ACS Photonics* **2**,1489-1497 (2015.).

228 Rodrigo, D. *et al*. Mid-infrared plasmonic biosensing with graphene. *Science* **349**, 165–168 (2015).

229 Cerjan, B., Yang, X., Nordlander, P., & Halas, N. J., Asymmetric aluminum antennas for self-calibrating surface-enhanced infrared absorption spectroscopy. *ACS Photonics* **3**, 354-360 (2016).

230 Verger, F. *et al*. Surface enhanced infrared absorption by nanoantenna on chalcogenide glass substrates. *Applied Physics Letters* **106**(7), 073103 (2015).

231 Umari, P., Pasquarello, A., Dal Corso, A. Raman scattering intensities in α-quartz: a first-principles investigation*. Physics Review B* **63**, 094305 (2001).

232 Fratini, S., Guinea, F. Substrate-limited electron dynamics in Graphene. *Physics Review B* **77**, 195414 (2008).

233 https://webbook.nist.gov/cgi/cbook.cgi?ID=C123864&Type=IR-SPEC

234 https://webbook.nist.gov/cgi/cbook.cgi?ID=C112801&Type=IR-SPEC&Index=1

235 Cui, T. J., Qi, M. Q., Wan, X., Zhao, J., & Cheng, Q. Coding metamaterials, digital metamaterials and programmable metamaterials. *Light: Science & Applications* **3**, e218 (2014).

236 Li, L. *et al.* Electromagnetic reprogrammable coding-metasurface holograms. *Nature Communications* **8**, 197 (2017).

237 Wang, L., Li, L., Li, Y., Zhang, H. C., & Cui, T. J. Single-shot and single-sensor high/super-resolution microwave imaging based on metasurface. *Scientific. Reports* **6**, 26959 (2016).

238 Lyakh, A., Maulini, R., Tsekoun, A., Go, R., & Patel, C. K. N. Intersubband absorption of quantum cascade laser structures and its application to laser modulation. *Applied Physics Letters* **92**, 211108 (2008).

239 Roy, T., *et al* Dynamic metasurface lens based on MEMS technology. *APL Photonics* **3**, 021302 (2018).

240 Bolotin, K., *et al* Ultrahigh electron mobility in suspended graphene. *Solid Solid State Communications* **146**, 351–355 (2008).

241 Novoselov K. S., *et al*. A roadmap for graphene. *Nature* **490**, 192–200 (2012).

242 Andryieuski, A., & Lavrinenko, A. V. Graphene metamaterials based tunable terahertz absorber: effective surface conductivity approach. *Optics Express* **21**, 9144-9155 (2013).

243 He, X., Liu, F., Lin, F., & Shi, W. Graphene patterns supported terahertz tunable plasmon induced transparency. *Optics Express* **26**, 9931-9944 (2018).

244 Zhang, Y. *et al*. Independently tunable dual-band perfect absorber based on graphene at mid-infrared frequencies. *Scientific Reports* **5**, 18463 (2015).

245 Huang, H. *et al*. Design of broadband graphene-metamaterial absorbers for permittivity sensing at mid-infrared regions. *Scientific Reports* **8**, 4183 (2018).

246 Cai, Y. *et al*. Enhanced spatial near-infrared modulation of graphene-loaded perfect absorbers using plasmonic nanoslits. *Optics Express* **23**(25), 32318-32328 (2015).

247 Sun, C., Dong, Z., Si, J., & Deng, X., Independently tunable dual-band plasmonically induced transparency based on hybrid metal-graphene metamaterials at mid-infrared frequencies. *Optics Express* **25**(2), 1242-1250 (2017).

248 Serway, R. A., & Jewett, J. W., *Principles of physics (2nd Ed.).* Fort Worth, TX: Saunders College Pub (1998).

249 Kim, S. *et al*. Electronically tunable extraordinary optical transmission in graphene plasmonic ribbons coupled to subwavelength metallic slit arrays. *Nature Communications* **7**, 12323 (2016).

250 Chen, K. *et al*. A reconfigurable active huygens' metalens. *Advanced Materials* **29**, 1606422 (2017).

251 Ee, H. S., & Agarwal, R. Tunable metasurface and flat optical zoom lens on a stretchable substrate. *Nano Letters* **16**, 2818-2823 (2016).

252 Iyer, P. P., Pendharkar, M., & Schuller, J. A. Electrically reconfigurable metasurfaces using heterojunction resonators. *Advanced Optical Materials* **4**, 1582-1588 (2016).

253 Wang, Q. *et al*. Optically reconfigurable metasurfaces and photonic devices based on phase change materials. *Nature Photonics* **10**(1), 60 (2016).

254 Zhu, Z., Evans, P. G., Haglund Jr, R. F., & Valentine, J. G. Dynamically reconfigurable metadevice employing nanostructured phase-change materials. *Nano Lett*ers **17**, 4881-4885 (2017).

255 Bohren, C. F., & Huffman, D. R. *Absorption and scattering of light by small particles*. John Wiley & Sons (2008).

256 Ismach, A. *et al.* Direct chemical vapor deposition of graphene on dielectric surfaces. *Nano Letters* **10**, 1542-1548 (2010).